UNIVERSITY OF SOUTHAMPTON

FACULTY OF PHYSICAL AND APPLIED SCIENCE

Electronics and Computer Science

Miniature Wind Energy Harvesters

by

Huihui Sun

Thesis for the degree of Doctor of Philosophy

May 2017

UNIVERSITY OF SOUTHAMPTON

ABSTRACT

FACULTY OF PHYSICAL AND APPLIED SCIENCES

Doctor of Philosophy

MINIATURE WIND ENERGY HARVESTERS

by Huihui Sun

Energy harvesting is a very attractive technique for a wide variety of self-powered microsystems such as wireless sensors. Airflow induced oscillations have been used as an attractive technique for energy harvesting because of its potential capacity for generating electrical power. The aero-elastic instability phenomenon such as flutter has been suggested especially for small scale energy harvesters.

This paper describes the design, simulation, fabrication, measurement and performance of a miniature wind energy harvester based on a flapping cantilevered beam. The wind generator is based on oscillations of a cantilever that faces the direction of the airflow. The oscillation is amplified by interactions between an aerofoil attached on the cantilever and a bluff body placed in front of the aerofoil. To achieve the optimum design of the harvester, both computational simulations and experiments have been carried out to investigate the structure. Simulation is achieved with ANSYS to optimise the structure and predict the power generation for practical design.

Both piezoelectric materials and electromagnetic transducers are used for the generator and tested. Three prototypes with the same volume of 37.5 cm^3 are fabricated and tested through two aspects of the performance namely the threshold wind speed for operation and the output power. Wind tunnel test results are presented to determine the optimum structure and to characterize the performance of the harvesters. The piezoelectric generator is fabricated by thick-film screen printing technique. The optimized device finally achieved a working wind speed range from 2 m/s to 8 m/s. The power output was ranging from 0.35 to 3.6 μW and the open-circuit output voltage was from 0.6V to 1.9V. The first electromagnetic harvester had a working wind speed range from 1.35 m/s to 6 m/s with a maximum power output of 29.8 μW and a voltage of 293 mV. While for the second generator, the wind speed for operation is form 1.5 m/s to 6.5 m/s. The output power is ranging from 8.9 μW to 41 μW and the output voltage is up to 171 mV. Results verified the harvester can effectively convert wind energy into large amplitude mechanical vibration without strict frequency matching constraints.

Declaration of Authorship

I, Huihui Sun, declare that the thesis entitled Miniature Wind energy Harvesters and the work presented in the thesisit are both my own, and have been generated by me as the results of my own original research. I confirm that:

- this work was done wholly or mainly while in candidature for a research degree at the University;
- where any part of this thesis has previously been submitted for a degree or any other qualification at this University or any other institution, this has been clearly stated;
- where I have consulted the published work of others, this is always clearly attributed;
- where I have quoted from the work of others, the source is always given. With the exception of such quotations, this thesis is entirely my own work;
- I have acknowledged all main sources of help;
- where the thesis is based on work done by myself jointly with others, I have made clear exactly what was done by others and what I have contributed myself;
- parts of this work have been published as:

H. Sun, D. Zhu, N. M. White, and S. P. Beeby (2016) **A miniature electromagnetic generator for wind energy harvesting**, (In preparation).

H. Sun, D. Zhu, N.M. White, S.P. Beeby (2015) **A miniature piezoelectric energy harvester for air flows**, *IEEE Symp. Des. Test, Integr. Packag. MEMS/MOEMS*, 1–3, doi:10.1109/DTIP.2015.7161035.

H. Sun, D. Zhu, N. M. White, and S. P. Beeby (2013) **A miniature airflow energy harvester from piezoelectric materials**, *J. Phys. Conf. Ser.*, 476, 012057, doi: 10.1088/1742-6596/476/1/012057.

H. Sun, D. Zhu, N. M. White, and S. P. Beeby (2015) **A miniature piezoelectric energy harvester for air flows**, *The 17th Symposium on Design, Test, Integration and Packaging of MEMS/MOEMS*, Montpellier, France

H. Sun, D. Zhu, N. M. White, and S. P. Beeby (2013) **A miniature airflow energy harvester from piezoelectric materials**, *The 13th International Conference on Micro and Nanotechnology for Power Generation and Energy Conversion Applications*, London, United Kingdom,

Signed:……

Date:……

Acknowledgements

This PhD thesis marks the end of my four-year challenging journey in Southampton, and it is now time for me to express my gratitude for all who made this journey smooth and enjoyable.

I am particularly grateful to my supervisor, Prof. Steeve Beeby, for giving me this opportunity to be his student and for his guidance and enthusiasm throughout my PhD and beyond. His scientific vision and rigorous academic attitude along with the trust and freedom he has offered makes an ideal environment for a simple student to develop into a research scientist. Thanks also go to my co-supervisor, Prof. Neil White for his helpful comments in my work. A special gratitude to Dr Dibin Zhu, my third supervisor, for his extensive advice and ceaseless supply of suggestions. The working experience with him in has made me completely forgotten any "hierarchy" in this academic world.

My sincere gratitude also goes to Dr Yang Wei and Dr Russel Torah for showing me the thick-film processing techniques. I also would like to take this opportunity to thank my fellow colleagues without whom this stimulating scientific environment would never exist and many of whom have become good friends of mine.

Furthermore, I would like to thank my friends in Southampton who I have shared great time with me. Big thanks to all the members of our "Poker Gang", and Dr 4U group.

I would thank my big family for their tireless love and support over the years. To my parents, thank you for always believing in me and raising me to be the person that I am today. I hope I have made you proud.

A special thanks to my beloved husband, Dr Ruomeng Huang, thank you for your constant unwavering support through the darkest of times, for your understanding, kindness and patience with me, and for constantly reminding me that life is wonderful. Finally, thanks to my son for giving me so much love and courage. Daddy and Mummy love you.

CONTENT

List of Figures

List of Tables

To My Dear Husband,

Ruomeng Huang

And My Son

Qianmu Huang

Chapter 1 Introduction

1.1 Background

Wireless sensor networks are one of the key enabling technologies as a concept formally put forward in 1991 by Mark Weiser [1]. It is a concept of deploying small, self-contained sensor nodes into an environment to collect and transmit information, and provide localised actuation. Potential uses for wireless sensor networks include: medical applications [2], structural monitoring of buildings [3]; status monitoring of machinery; environmental monitoring [4]; military tracking [5]; security; human guidance systems [6]; and wearable computing. Current wireless devices are often powered by electrochemical batteries. Considering their limited lifespan, it is obvious that periodic replacement of batteries is necessitated. These battery replacements can be troublesome due to the high cost and the large number of wireless devices in use at present [7]. In the case of wireless sensors that are located remotely, the sensor must be easily accessible to make the device function over extended periods of time [8]. Consequently, one of the major obstacles to extend the life of such devices is the limited lifespan of power sources, which must be replaced periodically. The continual evolution of solid-state electronics, from the invention of the bipolar transistor in 1949 [9] to the current state of the art integrated circuit manufacturing techniques [10], has led to large reductions in both the power and size of circuits required to perform given functions. This continual reduction in power consumption opens the possibility of other methods to power the sensors in a wireless sensor network [11]. Rather than powering the devices from a finite local store of energy, such as a battery, the device could be powered by harvesting energy from its local environment. Hence, as long as energy is present in that environment in a particular form, and the device has a suitable mechanism for converting that energy into an electrical form, the device can run indefinitely, subject to device reliability [12]. Towards this mission, researchers have begun investigating methods of energy scavenging for wireless devices over the past decades [13].

1.2 Energy Harvesting Overview

Energy harvesting, also known as energy scavenging, describes the process of capturing the ambient energy surrounding the electronics then converting it into electrical energy. The general concept behind energy harvesting is to convert unusable form energy into

a more useful form. Often the most useful form of energy in modern applications is electrical energy that can be stored in batteries or used to power electronic systems. The initial form of energy can originate from any number of energy domains, then being converted into a usable form of electrical energy by some form of transducer. Depending on the situation, we can classify energy harvesting sources in two ways. The first classification scheme places an emphasis on what kind of energy is converted; thus identifying four types of energy: photovoltaic energy, kinetic energy, thermal energy and electromagnetic energy.

The other classification scheme may consider the source where the conversion energy comes from. For example human energy source means the energy is provided by the activity of human beings or animals. Another example is environment energy source, in which the energy comes from the environment [14].

There are a number of ambient energy sources available as listed below [15]:

- Electromagnetic (RF) energy: Base stations, wireless internet, satellite communication, radio, TV, digital multimedia broadcasting, etc.
- Solar and light. The conversion mechanism can be Photovoltaic cell.
- Motion, vibration or mechanical energy: floors, stairs, object's movement, transfer energy from the engine to the battery during braking, etc. The electromechanical transducer can be electromagnetic, electrostatic, or piezoelectric.
- Fluid flow (liquids or air).
- Pressure gradients (from air or sea water)
- Thermal energy: Geothermal from temperature, combustion, waste heat from vehicle exhausts, etc.
- Biological energy: biofuels, biomass.

Each of these sources can be utilized separately or combined together to power microelectronic systems. However, it is difficult to generalize which energy source is the most suitable; as each application should be evaluated individually with regards to choosing the best energy harvesting method.

Among the common renewable energy sources, wind (airflow) energy harvesting has been widely researched for high power applications where large wind turbine generators are used for supplying power to remote loads and grid-connected applications. With the recent increase in public interest in renewable energy sources, wind energy is gaining popularity as perhaps the most technologically developed and practical alternative today. The wind turbine technology has already been well documented and sophisticated. As generating energy from wind does not depend on a dominant-frequency, the natural frequency of the vibrating structural therefore does not need to match a certain frequency, which results in great flexibility in the configuration of the harvester. Another method for wind energy extraction is called flow-induced

vibration based on aerodynamic instability phenomena.

Despite those advantages previously mentioned on energy harvesting from wind, there are many challenges as well. The intermittency of wind hinders continuous energy production, and the inconsistent quality of wind reduces the efficiency of harvesters. Unpredictable directions of wind are another issue for flow-induced harvesters. All these challenges must be addressed in using wind as a reliable input energy source.

1.3 Motivation of Work

Energy consumption of buildings in developed countries comprises 40% approximately of total energy use and is above industry and transport as shown in Figure 1.1. The upward trend in energy demand will continue in the future because of growing population, increasing demand for building services, as well as the rise in time spent inside buildings. Among the building servicers, the growth in HVAC systems energy use, which presents 55% of the total primary energy consumption, is particularly significant [16].

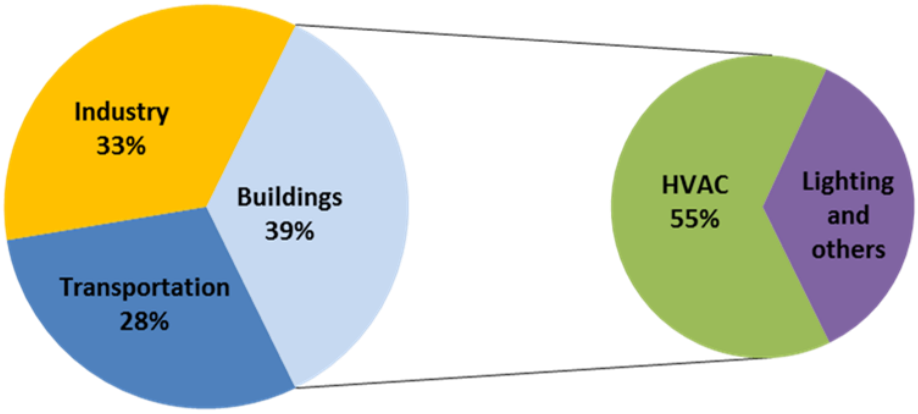

Figure 1.1: World final energy consumption and energy use in buildings.

HVAC (Heat, Ventilation and Air Condition) system is designed to provide a comfortable and desired environment for the occupants. To achieve this, temperature, humidity and gas sensors are deployed in air ducts to monitor air quality. Harvesting localized air flow power form HVAC systems is an opportune way to power a sensor. For this application, airflow energy is the most obvious source since it is already available in air ducts in the buildings. Although many devices have been published for airflow energy harvesting, few can operate in the entire range of flow speeds in HVAC ducts in the buildings, typically between 1.5 m/s – 4.5 m/s [17]. For small scale wind turbines, which are the most common used structures, the starting airflow speed of operation are normally 3 m/s to 4 m/s. The relatively high starting speed makes small

turbines unable to harvest from the entire air ducts flow range. Moreover, these rotating components suffer from fatigue and wear, hence are not desirable for long-term applications. Flow-induced vibration is a novel approach to airflow energy harvesting, and many studies have already been done on these structures. The potential advantages of this technique appear in compactness, robustness and simple construction. However, as these harvesters are not currently at "utility scale", there still exists a gap in investigating them theoretically and experimentally. In addition this application just begins to touch on the large potential of energy harvesting for powering many sensors that could be used in air ducts.

1.4 Objectives of Work

The focus of this work is to provide an airflow energy harvester which can effectively convert the energy of a uniform and steady flow into periodic motion of the solid structure. The main objective of this work includes the following specifications:

The harvester has a wider air speed range for operation. This goal implies minimising the threshold wind speed (the lowest wind speed at which the harvester can operate) of the harvester. As mentioned above, many published devices, particularly small wind turbines, are developed for wind speeds above 3 m/s, which make them unable to harvest from low flow speed in the ducts. However for practical applications, wind harvesters should operate below 2.5 m/s of wind speed to charge sensor nodes. In HVAC ducts, in order to operate throughout the entire range of flow speeds, a low threshold wind speed (1.5 m/s) is necessary for the harvesters. Moreover, the inconsistent quality of wind reduces the efficiency of the harvester. And this problem can be improved by designing the harvester with a wider flow speed range for operation as well.

The focus of the wind energy harvester is the conversion of energy of a uniform and steady flow into periodic motion of the mechanical structure with the aim of obtaining high efficiency, high power density and having a capability to self-start and sustain the periodic motions. To build up a self-excited energy harvester with the optimum structure, investigations should be carried out with both computational simulations and experimental work. In addition, the scaling effects of flow-induced harvesters are unknown. Hence such harvesters may have better performance than rotary harvesters at some scales. In order to compare the performances of wind harvesters with different scales, a previously published wind generator should be used as a reference system.

Converting the mechanical energy from wind into electrical energy is performed by a transducer. Among these transduction systems, piezoelectric and electromagnetic generators present the advantages of harvesting high power levels with simple implementations. They have been widely studied in both macroscopic realizations as well as MEMS structures [18]. Most researches have discussed some optimizations of

harvested power of the electromagnetic or piezoelectric energy harvesters while limited works have been conducted to compare the power harvesting performance. Generally electromagnetic transducers bear the advantage of high efficiency if there is no size constraints applied. While piezoelectric generators are favourable for miniature devices when size is the main concern. However, most researchers used piezoelectric transducers of flexible materials such as PVDF, piezoelectric ceramics especially thick-film printed PZT materials should be investigated for wind energy harvester applications. Moreover the performance of piezoelectric and electromagnetic generators should also be compared theoretically and experimentally.

1.5 Thesis Structure

This thesis will detail the development of a miniature energy harvester for airflow. In Chapter 2, an extensive literature review is conducted. The background of wind energy harvesting together with the current state in this field especially in micro size is briefly introduced. In Chapter 3, the wind energy generator with cantilevered beam structure is studied, together with theory relatively to both piezoelectric and electromagnetic transduction systems. Chapter 4 focuses on the derivation of design parameters and the simulation model of the mechanical structure. The harvester consists of four components, including a beam, a wing, a base part and a bluff body. In order to investigate the influence of the mechanical structure, both computational simulations and experimental work are carried out. An analytical model based on pure mechanical structures of the device is developed. And a prototype of the harvester is fabricated for experimental work. Both simulation and experimental results will be compared to obtain the optimum structure of the harvester. After investigating the mechanical structure, the transduction systems should also be considered. To compare the performance of piezoelectric and electromagnetic generators, both transducers are used for the harvester during the tests. In Chapter 5, a prototype of the piezoelectric wind harvester is fabricated and tested. The typical piezoceramic material, PZT, is chosen for the transducer using normal thick-film printing technique. Both simulations and experiments are carried out to estimate the performance of the harvester. A set of experiments both on shaker and in the air duct are carried out to investigate the performance of the harvester. The testing results are used to compare with the simulation results in Chapter 4 as well. In Chapter 6, the electromagnetic transducer is also investigated to compare with the piezoelectric one. Two commonly electromagnetic generator structure are designed, which are magnet-through-coil (MTC) structure and magnet-across-coil (MAC) structure. Final devices with optimum design and structures are used to compare with the piezoelectric one and other devices in review part. All these works are summarized and concluded in the final chapter.

Chapter 2 Literature Review

2.1 Energy Harvesting History

The first harvesting energy in the form of current generation from heat was observed by Thomas Johann Seebeck in 1821. He found that a closed circuit made of two dissimilar metals with junctions at different temperatures, would induce an electrical current. This phenomenon was then given the name thermoelectric effect [19]. Electromagnetic induction was discovered by Joseph Henry and Michael Faraday in 1831 [20], and in the same year, the first direct-current generator, consisting of a copper plate rotating between magnetic poles, was invented by Faraday. In 1839, Edmund Becquerel discovered the photovoltaic effect when he did experiments with an electrolytic cell composed of two metal electrodes [21]. However, it was not until 1894 that Charles Fritts built the first large area solar cell using a layer of selenium with a thin layer of gold coated to form the junctions [22]. The first harvesting energy in the form of charge generation was recognised in 1880 by Pierre and Jacques Curie. They successfully proved that certain crystals would exhibit a surface charge when subject to mechanical stress, known as piezoelectricity.

2.2 Kinetic Energy Harvesting

Although it is difficult to generalize the power levels available from different types of energy to determine which energy source is the best for harvesting, kinetic energy in the form of motion or vibration is generally considered as the most versatile ambient energy source available. Solar energy harvesters can achieve relatively high power densities in good light conditions, but they are unsuitable for implantable devices, low light or dirty situations. Thermal devices require a temperature gradient to generate electrical energy, which is difficult to achieve in miniature generators. Kinetic energy is a readily harvestable energy source, both for human and for environment energy harvesting devices. The power transferred to a load is limited by the availability of the raw energy, the efficiency of the transducer, the conversion circuit and the harvester size constrains.

2.2.1. Types of Kinetic Energy Transduction Mechanisms

The principle behind kinetic energy harvesting is the displacement of a moving part or the mechanical deformation of some structure inside the energy harvesting device. With respect to mechanical structures, there are two types of possible generators. One is called inertial generators, which the kinetic energy is obtained from vibrations or displacements of a proof mass. These devices are mostly based on mass-spring-damper systems that resonate at a particular frequency. Being resonant, when the mechanical stimulus vibrates at a frequency that matches the resonance, these generators work most efficiently. The other mechanical structure is the non-inertial generator, where energy is obtained from the deformation caused by applied pressure on piezoelectric materials. In this case, the obtained energy usually depends on the rate and amount of deformation instead of on the proof mass in inertial generators.

One of the crucial requirements for energy harvester is to convert energy collected into an electrical form, that is, some form of transduction mechanism. In this report for example, it is the kinetic energy collected by the mechanical part of device that should be transferred into electrical energy. Different methods have been utilized to realize this requirement. The electricity can either be generated from mechanical strain or the relative displacement present in the system. These methods lead to three major transduction mechanisms which have been widely used nowadays: piezoelectric generators, electromagnetic transduction and electrostatic generators. The characteristics such as damping effects ease of use, scalability and effectiveness are different for each mechanism, and hence the suitability for these mechanisms are subjected to practical constraints. The following subsection will describe these three mechanisms in detail separately.

2.2.2. Piezoelectric Generators

2.2.2.1 Piezoelectric Effect

If a piezoelectric material is loaded with a pressure, it is compressed as any other elastic material, and it is extended transversely to the direction of the load. In addition, electrical charges are generated on the electrodes on the surface of the piezoelectric material and it is possible to measure a voltage between the electrodes. The generation of charges is called the piezoelectric effect. There is also an inverse piezoelectric effect whereby an applied electric field can produce a mechanical strain. Piezoelectric materials are therefore used to convert mechanical energy into electrical energy.

2.2.2.2 Piezoelectric Materials

There are two kinds of piezoelectric materials: monocrystalline materials, such as quartz, zinc oxide, and ferroelectric materials, such as ceramics PZT (lead zirconate titanate), and the polymer PVDF (poly vinylidene fluoride). The efficiency of electric transduction differs for each material with different piezoelectric properties. In general the piezoelectric effect of monocrystalline materials is comparatively small. Therefore, the piezoelectric effect of ferroelectric materials is employed in most cases [23]. However, ferroelectric materials are not immediately piezoelectric after they are fabricated and they need a certain procedure to activate the electromechanical interaction property. Similar to ferromagnetic materials which need to be magnetized in a magnetic field before they become permanent magnets, ferroelectric materials need to be polarized by a large electrical field before use.

For piezoelectric ceramics, most of them are manufactured in bulk form commercially. However, due to the relatively large thickness (greater than 100 μm), their application is limited in Micro-Electro-Mechanical Systems. Film piezoceramics, on the other hand, are more favourable to fabricate devices with thickness less than 100 μm for electrical power generation because of its relatively high piezoelectric activity compared to piezoelectric polymer materials [24]. Film piezoceramics can be fabricated with thin- and thick-film technologies. Thin-film technology is basically used to fabricate films with thickness less than 5 μm. The process involves physical vapour deposition, chemical vapour deposition, and solution deposition. For thicker films between 10 μm – 100 μm, thick-film technology is more favourable, which involves screen printing technique.

2.2.2.3 Piezoelectric Constants

Since piezoelectric materials are anisotropic, their physical constants relate to both the direction of the applied stress or electric force and to the directions perpendicular to the applied force. Therefore each constant generally has two subscripts to indicate the directions of the two related quantities. As illustrated in Figure 2.1, the direction X, Y and Z are represented by the subscript 1, 2 and 3 respectively, and the shear about these axes are represented by 4, 5 and 6 respectively. The various constants can be written with these subscripts.

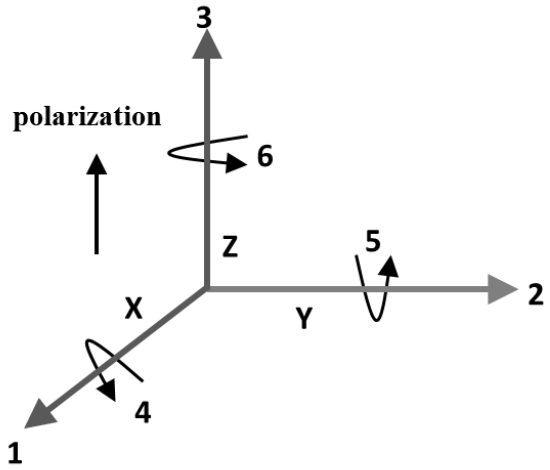

Figure 2.1: Direction of forces affecting a piezoelectric element.

The most frequently used piezoelectric constants are: the piezoelectric charge constant *d*, the piezoelectric voltage constant *g*, and the permittivity *e*. The main constant describing the piezoelectric effect is the piezoelectric charge constant *d*, which relates to the strain caused by the electric field in the absence of mechanical stress and to the electrical charge per unit area by the applied stress under zero electric field. The first subscript to d_{ij} indicates the direction of polarization generated in the material, and the second subscript is the direction of the applied stress or the induced strain, respectively. For instance, as shown in figure 2.2, d_{31} means that the induced polarization is in direction 3 and the stress is applied along axis 1. d_{33} on the other hand, means both the induced polarization and the stress are in direction 3.

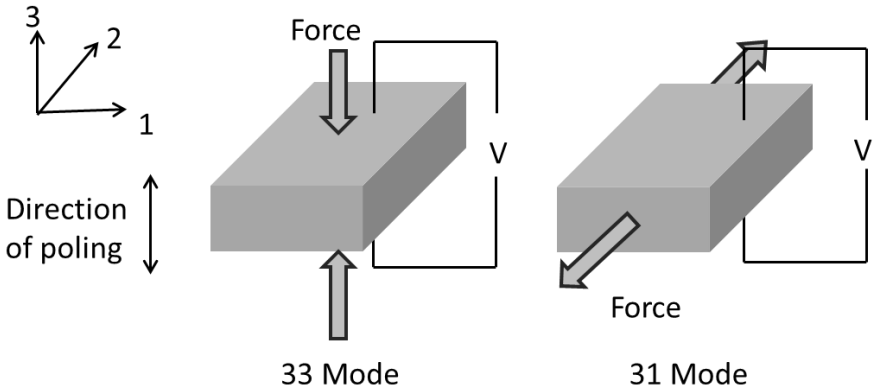

Figure 2.2: Piezoelectric constants in typical energy harvesting modes. Reprinted from [25].

The most advantageous way to employ piezoelectric materials is cantilevered structures operating in a bending mode with piezoelectric layers attached to surfaces on one or two sides (unimorph or bimorph). It is commonly used for enabling relatively high stress levels on the piezoelectric material while minimizing the dimensions of the devices. The structure can be

designed to operate in either d_{31} or d_{33} modes depending on the arrangement of the electrodes. In many cases, d_{31} mode has been used where a piezoelectric layer is sandwiched between two metal electrodes. The piezoelectric layer is poled and driven through its thickness thereby straining the piezoelectric material and generating a charge. In contrast, the d_{33} mode is poled parallel to the passive layer using an interdigitated transducer (IDT) where stress can be applied to the poling direction. In many ferroelectric materials, the d_{33} coefficient is two to three times larger than the d_{31} [26].

2.2.2.4 Poling

The piezoelectric properties of ferroelectric materials can be enhanced by applying a sufficiently high electric field at an elevated temperature, therefore generating an internal remnant polarization in the material, which continues long after the removal of the electric and thermal fields. This process is known as poling [27].

Several poling techniques that have been developed are: contact poling, corona poling, photo thermal poling and electron beam poling. Each technique has some advantages and drawbacks. In this paper, contact poling is used as a simple static field poling technique.

In the contact poling process a large poling field is created through electrodes with the piezoelectric film in between (Figure 2.3). The film is heated up to an elevated temperature and the poling voltage, depending on the thickness of the material, is applied through electrodes. The main drawback of this technique is the limited voltage that can be applied due to the dielectric breakdown in surrounding air or in the poled film itself [28].

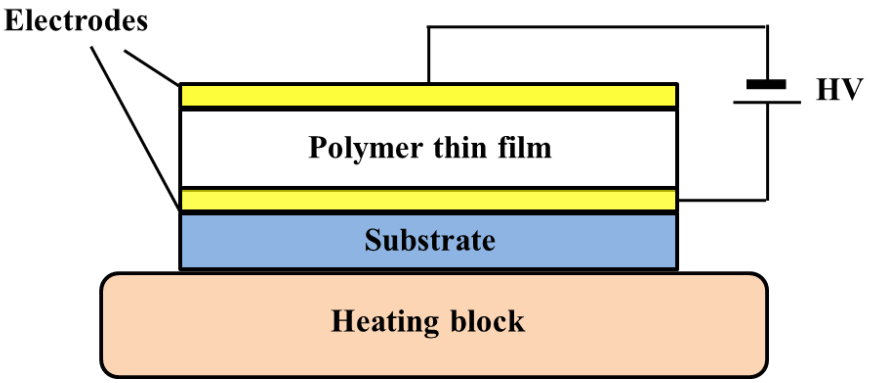

Figure 2.3: Schematic of the contact poling technique.

In all techniques, heating is the essential process to permit dipoles inside the material to become mobile and orient in the direction of the applied **external** field. The orientation is then frozen

by cooling the poled film to room temperature whilst under the applied external field.

The effect of poling conditions including temperature, time and electric field has been investigated by Torah *et al.* [29]. Results showed the value of d_{33} increased with poling temperature and duration, as well as the poling voltages. However, the maximum achievable poling field is limited by the electrical breakdown of the films. An optimum result was obtained at a temperature of 200°C with poling times of 30 minutes and electric filed strength up to 4 MV/m. However, little improvement was achieved in the piezoelectric activity when the applied electric field was above 2.5 MV/m.

2.2.2.5 Thick-film Screen Printing

Screen printing is one of the oldest forms of graphic art reproduction. The basic concept is to deposit ink or paste onto a base material or substrate by the use of a finely woven screen with the desired pattern [30]. This technique is traditionally used for the production of graphics onto items such as T-shirts and mugs. Then it has been applied to manufacture electronic components as well as microelectronic thick-films with typical thickness ranging from 0.1 μm to 100 μm [31].

The standard process starts with a typical screen, which is made of a finely woven mesh of stainless steel, adhesively attached to a cast aluminium frame and coated with a UV-sensitive emulsion. The mask is generated on the mesh through which the paste can be squeegeed to produce a pattern on the substrate. The mask is patterned by a standard photolithography process [32]. The paste is poured onto the upper surface of the screen, and then a rubber blade called a squeegee sweeps across the screen under pressure, forcing the paste through the apertures of the screen onto the substrate as shown in Figure 2.4. However, before starting screen printing, some parameters need to be considered in the printing profile such as the printing gap, velocity and pressure of the squeegee.

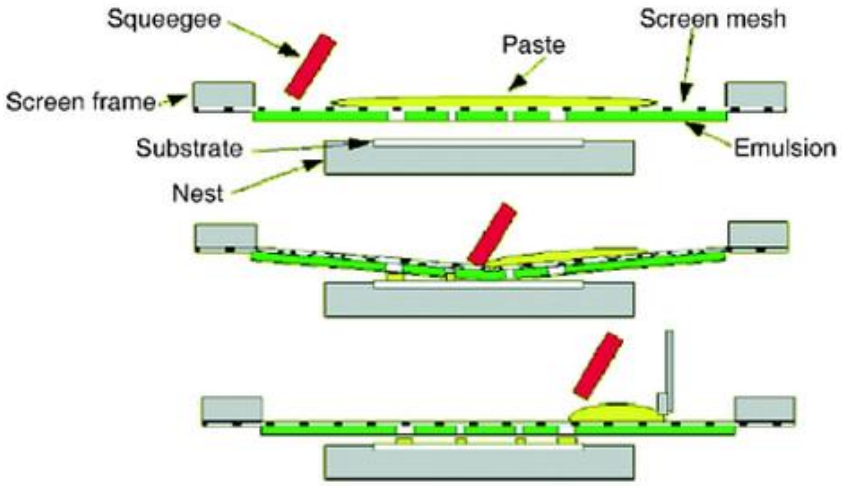

Figure 2.4: Process of screen printing. Reprinted from [32].

After screen-printing, the deposit films are dried to remove the organic carriers in the paste and form a rigid film for over-printed upper layers. This stage is usually undertaken in an infrared belt drier at a temperature of approximately 150˚C The next step is firing the films to produce a solid film one on the substrate and bind the active particles together. This process is achieved in a belt furnace in air atmosphere at temperatures up to 900˚C [32]. After firing, the film is firmly attached to the substrate. Then the printing, drying and firing process can be repeated if further screen printed layers are needed.

2.2.2.6 Applications

The piezoelectric generator is widely employed because of the large output voltage or force which can be generated in a small volume. A large percentage of recent studies have focused on improving the efficiency of piezoelectric energy harvesting systems by means of changing the configuration of the device to maximize the energy captured from the ambient environment.

The type of piezoelectric material selected can have a major influence on functionality and performance of the harvester. To date, the most commonly used piezoelectric material is lead zirconate titanate, a piezoelectric ceramic, known as PZT, which has very high electromechanical coupling ability. However, PZT is extremely brittle, limiting the strain that it can safely absorb without being damaged [33]. In order to eliminate the disadvantages of piezoceramic materials and improve their efficiency, researchers have developed a wide variety of piezoelectric materials that exhibit more flexibility and can be employed in energy harvesting applications [34, 35]. Other methods of modifying the configuration of piezoelectric energy harvesters have been investigated by different researchers including changing the

electrode pattern, altering the poling and stress direction, layering the material to maximize the active volume, and tuning the resonant frequency of the device [36–39].

2.2.3. Electromagnetic Transduction

2.2.3.1 Electromagnetic induction

Electromagnetic induction was first discovered by Faraday in 1831, which states the generation of electric current in a conductor when it is located within a varying magnetic field. This applies whether the field itself changes in strength or the conductor moves through it. For a typical electromagnetic generator, the conductor takes the form of a coil and permanent magnets are used to produce the magnetic field. Therefore the electricity is generated either by the relative motion of the magnet and coil, or the changes of the magnetic field. In this case, the induced voltage across the coil depends upon the strength of the magnetic field, the velocity of the relative movement and the number of turns of the coil.

2.2.3.2 Application

Electromagnetic transduction has been widely used in the form of rotating generators for many years. It generates power from a few watts (brushless DC domestic wind turbine systems), to several hundred megawatts (synchronous machines used for power generation by the utility companies). For kinetic energy harvesting, both rotating generators and linear generators can be exploited to harvest power from rotation and vibration. One of the most effective methods for linear generators is to use an inertial frame configuration, in which the relative movement between the magnets and the coils are induced by the vibration of a resonating cantilever beam. Either the magnets or the coil can be chosen to be mounted on the beam while the other remains fixed. However, it is generally preferable to attach the magnets onto the beam as the inertial mass [40]. Figure 2.5 shows two commonly used arrangements of electromagnetic generators.

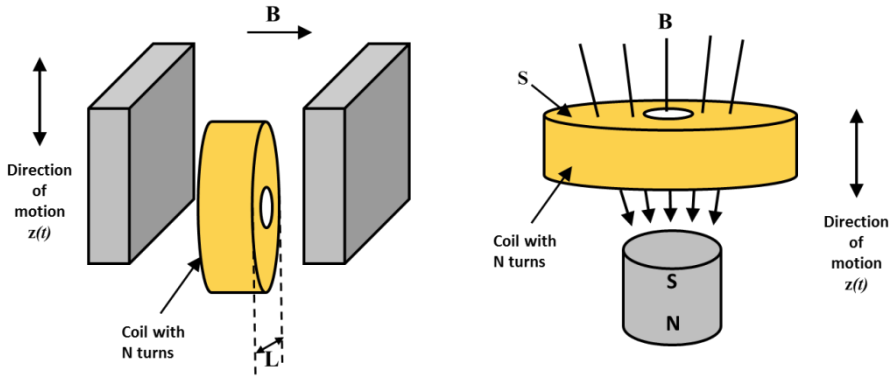

Figure 2.5: Schematics of two electromagnetic generators arrangements.

Electromagnetic transduction has the advantage of high efficiency compared with other mechanisms when there are no size constraints applied. This advantage is largely contributed to the feasibility of designing the coil in such a way (e.g., increasing the number of turns, decreasing the coil resistance by using larger diameter wire, using a larger area coil) to achieve high coupling factors. Several examples demonstrating this principle can be found in the literature [41–46].

2.2.4. Electrostatic Generators

Electrostatic forces have also found use in converting kinetic energy into electrical energy. These types of generators consist of a variable capacitor whose two plates are electrically isolated by air, a vacuum, or an insulator. External vibration (on both horizontal and vertical directions) will lead to a movement of the two plates and hence induce a capacitance change. There are two modes of operation for electrostatic generators. The first is called constant charge operation as shown in Figure 2.6(a). For the parallel plate structure, in which the two plates have a constant overlap with a variable separation, the field strength is proportional to the charge and thus the energy density of the electric field is independent of plate separation. As the electrode separation increases, additional electrical potential energy is stored as an increase in the electric field. If the plates, on the other hand, are moved relative to each other with a sliding motion at a constant separation, mechanical work is done against the fringing field and there is an increase in stored electrical energy because the electric field strength increases with the reduction in plate overlap [47].

The other mode of operation is referred as constant voltage operation, in which a constant voltage is applied on the two plates as illustrated in Figure 2.6(b). If the plate separation is increased with a fixed overlap, the electric field strength between the plates falls causing charge to be pushed off the plates into an external circuit as a current flow *i(t)*. If the plates are moved with constant separation and changing overlap, the field strength stays constant while the current is again forced to flow into the source because the volume of the field decreases. In both cases, the mechanical work done is converted into additional electrical potential energy as an increased space charge in the voltage source.

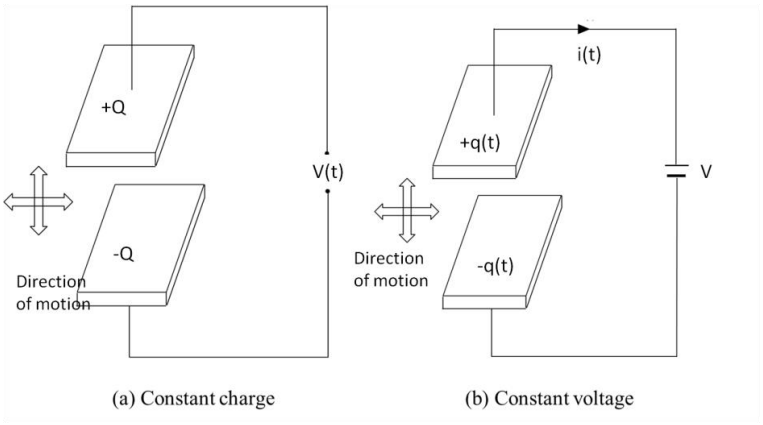

Figure 2.6: Principle of operation of the electrostatic generator.

The efficiency of electrostatic transducer is limited by technical challenges including charging the electrodes, the separation distances, and the amplitudes of displacement [48].

2.3 Wind Energy Harvesting

A number of sources can provide kinetic energy including human movements, mechanical vibrations from environment, and fluid flow (liquid flow and airflow). Of several possible alternatives, wind energy has been utilized for thousands of years and became one of the most important sustainable energy resources. Since the beginning of the twentieth century, this technology has developed rapidly towards new dimensions in both large and micro scales. Nowadays, existing methods of wind energy harvesting include using turbines, harvesting energy from flow-induced vibration and using Helmholtz resonators.

2.3.1. Wind Turbines

2.3.1.1 Description of technique

A wind turbine, also known as windmill, is essentially a rotating machine which converts the kinetic energy from the incoming wind into the electric energy. The design is based on the drag or lift effect relying on different air resistance on the front and back of the rotor section to cause rotation. The first wind turbines for electricity generation emerged at the beginning of the 20th century and the technology improved incrementally since early 1970s. There are two categories of wind turbines according to different direction of the rotational axis: horizontal-axis wind turbines (HAWT) and vertical-axis wind turbines (VAWT). The former one captures kinetic wind energy with propeller rotors and the rotating axis is parallel to the direction of wind. While the other one uses straight or curved bladed rotors perpendicular to the wind. The advantage of all vertical-axis windmills is that they can accept wind coming from all directions,

thus, they do not have to face up or downwind for rotation like the horizontal-axis machines. However, since the end of the 1980s, the development of vertical-axis wind turbines has almost stopped due to their lower efficiencies [49]. The horizontal-axis approach currently is used world widely.

Modern wind turbines generate electricity using slender aerodynamic blades and tall towers. The general components are:

- A rotor to convert wind energy into mechanical power.
- A tower to support rotor.
- A gearbox to adjust the rotational speed.
- A control system to monitor operation of wind turbine automatically.
- A foundation to protect the turbines in high speed winds.
- A generator to convert mechanical energy into electrical power.

The main operation of wind turbines to generate electricity is: When the wind blows, the blades lift, rotate and turn the rotor, which creates mechanical energy. The generator uses magnetic fields to convert the kinetic rotating energy into electrical energy. The power output can be transformed to the right voltage or stored in batteries for typical systems. The control system is connected to an anemometer to measure wind speed continuously. It allows the turbine to rotate, producing power in a certain level when wind speed is high enough. If the wind speed exceeds its limits of the electrical or mechanical parts of turbines, the system will cut out to prevent more power increase.

Some elements can influence the performance and the design of wind turbines. The most important factors are wind speed and wind turbine availability. The maximum mechanical power that can be extracted by a wind turbine is given by:

$$P_t = \frac{1}{2}\rho A v^3 c_p(\lambda, \beta) \qquad \text{(Equation 2.1)}$$

Here P_t is the power (W), ρ the density of air, A the rotor area, v the wind speed and c_p is the coefficient of power that is a function of tip speed to wind speed ratio, λ , and blade pitch angle, β . The power is proportional to the area of turbine blades and the cube of the wind speed, which means that the maximum available power can reduce significantly with scaling down the size of wind turbine or decreasing wind speeds. The average wind speed is unstable due to its variation with time, altitude, gusts, and fast changes in direction or air density [50]. An average speed of 4.5 m/s to 5 m/s is typically needed to make the electricity economically

feasible; however, some windmill designs begin producing electricity at a wind speed as low as 3.5 m/s [51]. The power efficiency is described by c_p, a dimensionless term with a theoretical maximum value of 0.59. This is known as the Betz limit. However, in practice, due to the stall and viscous drags of the rotor, bearing or gear losses of the transmission and the low efficiency of the generator, the total efficiency of the wind turbine is much lower.

2.3.1.2 Recent development in wind turbine generators

In order to maximize the energy captured by wind turbines, much research had been done in this field particularly from the point of view of velocity direction control of the wing and in turbine blade design. With respect to recent development in wind turbine generators at large scale, some researchers have put an emphasis on magnetic bearings. A mechanical bearing is typically used to promote smooth rotation of the rotor in the wind turbine. However, there is always friction between the bearing and the rotor as a result of mechanical contact, increasing the driving force of transmission drive system and reducing efficiency of energy conversion. No matter how frequently the bearing is maintained to be lubricated, it will gradually wear out and eventually fail. To solve this problem, magnetic bearing has been investigated and applied to wind turbine as a replacement of the traditional mechanical bearing [52]. The magnetic bearing supports the rotor using magnetic levitation, thus there is no physical contact between the rotor and the bearing. Because of the full magnetic levitation, the rotation has a very low friction and no mechanical wear, the life time of the turbine can be increased and the maintenance cost will be reduced. Liu *et al* [53] reported a magnetically suspended VAWT, which also proved that the starting wind speed of the magnetically suspended turbine is reduced to 1.5–2.5 m/s, which is much lower than that of the traditional turbine with the same size (3–4 m/s).

On the other hand, as large-scale wind turbine technology is well documented and matures, more and more attention has been paid to the development of small scale wind turbine generators. However, to the author's best knowledge, very few research works can be found in the literature that discuss the issue of wind energy harvesting using micro wind turbines which are miniaturized in size. A miniature wind turbine can be generally defined as rotor-tip diameter of several centimetres in scale. It is used to capture efficient power from where modest ambient airflows are present, for example, in heating, ventilating, and air-conditioning ducts, or in outdoor environments [54]. Several challenges are associated with this type of miniature wind energy harvesting system in contrast to the large-scale systems. They are: (i) wind speeds of interest at low height and concealed ground are relatively low compared to large-scale systems; (ii) relatively high viscous drag on the blades at low Reynolds number; (iii) aerodynamic force generated by miniaturized vanes with very small surface area is extremely small in comparison

to huge wind turbine; (iv) bearing and thermal losses increase significantly as size decreases. Consequently, for miniature windmills, which operate at a much higher speed and low Reynolds number, it is important to understand how the size of the generator will affect its performance. Shrestha *et al.* [55] investigated scaling laws for wind turbine generators. It concluded that the output power of the generator decreases with reduction of the mass and length of the blades at different ratio.

A number of miniature energy scavengers based on turbines have been demonstrated successfully with different techniques in recent years. Some of them showed good performance with a maximum efficiency close to 40%. Hirahara *et al.* demonstrated a small wind turbine system with a 50 cm rotor diameter [56]. Research group from Uludag University also reported a miniature wind turbine rotor using different shapes of aerofoils. The rotor models had a 31 cm diameter were made from Balsa wood [57]. However, those devices are relatively large in size, which may not be appropriate for wireless sensor applications.

Some miniature wind turbines whose rotor-tip diameters smaller than 10 cm have already been published. A micro electromagnetic power generator with 4.2 cm diameter turbine was reported by Rancourt in 2007 [58]. After test, an output power of 2.4 mW was achieved with 5.5 m/s wind speed and 130 mW at 11.8 m/s. The maximum overall efficiency was 9.5% at 11.83 m/s but at 5.5 m/s efficiency was as low as 1.85%. Holmes and his colleagues from Imperial College have reported a micro-power conversion device combined an axial-flux electromagnetic generator, of which the rotor area was down to approximately 1.5 cm^2 [59]. However, in this design, due to its configuration, the power generation capability is limited. To improve performance further, in 2009 and 2011, they developed similar turbine geometry, a shrouded wind turbine with an integrated axial flux permanent magnet generator [60, 61]. Figure 2.7 shows a prototype of the device. It is fabricated by rapid prototyping and traditional machining techniques, as well as flexible printed circuit board. In the rotor area, there is a central hub, an annular rim, and a number of blades, which are all made by rapid prototyping. A thin layer of nickel coating is electroplated on the blades for strengthening. The rotor is fixed on a stainless steel casing, held by a pivot and bearings. The static friction of bearings is a critical issue because it determines the lowest airflow speed for operation of wind turbines. In this design, they used jewel bearings, which can offer very low starting friction. In the experiment, a prototype with 12 blades was tested and showed the threshold wind speed for operation is 4.5 m/s, and the output power is approximately 4.3 mW at average flow speed of 10 m/s.

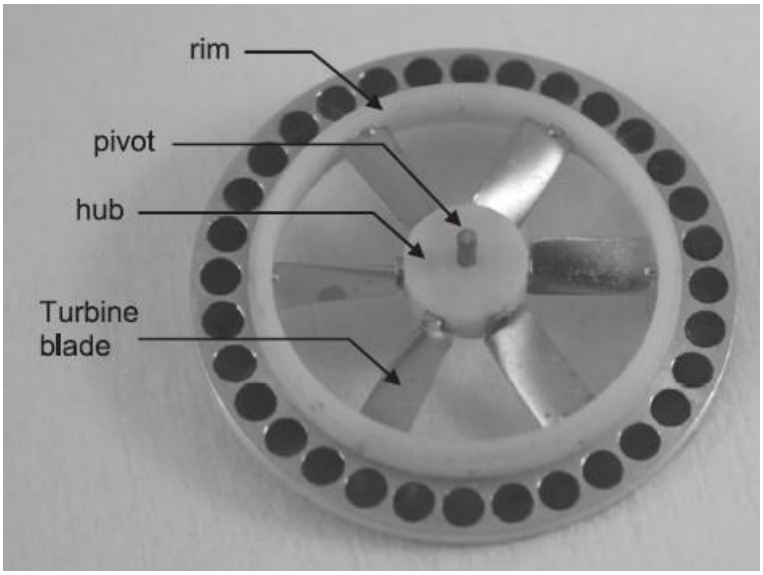

Figure 2.7: Schematic view of wind turbine. Reprinted from [61].

Most miniature wind turbines are mainly focused on the design and fabrication techniques, while some researchers concentrated on harvesting circuit control and the general theory of system modelling to assist the design and estimate the performance. Carli *et al.* [62] provided a detailed model and characterization of the micro wind turbine with an effective power-saving architecture to control the harvesting circuit. The optimized design of the wind flow harvester had a turbine diameter of just 6.3 cm. A highly efficient buck-boost converter, aimed towards the minimization of its power losses, is the core of the optimal power point tracking circuit. The experimental results showed that the wind generator was able to supply up to 10 mW with an airflow speed of about 7 m/s, and can work at its maximum efficiency over a wide range of operating conditions. Xu *et al.* [63] successfully designed an equivalent circuit model used as a guild line for predicting and optimizing the performance of the wind turbine system. The maximum output power reached 13.5 mW and 18 mW at the wind speed of 4 m/s and 4.5 m/s respectively.

Although a majority of existing turbine generators are based on electromagnetic transducers as mentioned above, there are some researches on piezoelectric wind turbine generators. Chen and Lin [64] investigated the feasibility of using resonant piezoelectric structures to generate energy from wind flow. Simulation results showed that the efficiency of such piezoelectric wind turbine generator is only 0.003% which is much lower than the Betz limit. A novel small scale piezoelectric windmill for energy harvesting from the wind flow was demonstrated by Priya *et al.* in year 2004 [65]. The device has 11 bimorph piezoelectric cantilevers arranged along the circumference of the centre shaft which is connected to the rotor of the wind turbine. The centre rotates with the rotation of the wind turbine. The stoppers bend the piezoelectric cantilevers to produce electricity. As the piezoelectric material has great impact on the

performance of the transducers, with this structure, the mechanical energy transferred to the bimorph was high. This study was further extended in year 2005 and a theoretical model to estimate the generated electric power output was presented [66]. The piezoelectric wind mill was found to be capable of producing electrical power up to 7.5 mW at the wind speed of 4.5 m/s. Two years later, researchers from the same department of the University of Texas designed another piezoelectric windmill with an optimized structure [67]. Figure 2.8 shows the inner structure of the windmill and crank assembly which consisted of a vertical shaft connected to a lever arm that converted the rotational motion into translation motion. All three fans were connected into the single vertical shaft through an adjustable gear ratio. The wind mill was composed by two rows of piezoelectric bimorphs, as front and back rows, where each row had nine bimorphs. Therefore, this windmill can reduce the force required for deflection and expand the surface area for energy capturing. In addition, the frequency can be adjusted by varying the gear ratio. After testing, the windmill can operate at a low flow speed down to 3 m/s; and with a flow speed of 4.5 m/s, it generated a 5 mW continuous power. In year 2010, Bressers *et al.* attempted to develop a contact-less wind turbine which utilizes vertical axis Sarvonius wind turbine rotor and piezoelectric bimorphs [68]. This device has a series of piezoelectric bimorphs with magnets at the tip placed horizontally around the wind turbine rotor shaft. The magnets were used to induce harmonic vibration in the piezoelectric elements. The design of contactless wind turbine having a size of 80 mm × 80 mm × 175 mm was found to provide peak power output of 1.2 mW at 4 m/s of wind speed.

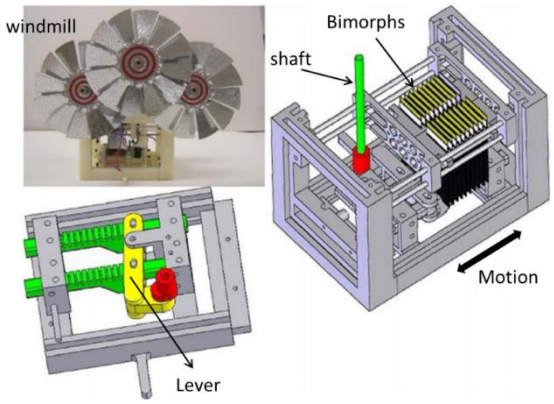

Figure 2.8*:* Piezoelectric windmill with isometric view and internal structure. Reprinted from [68].

Many miniature wind turbines have been demonstrated successfully for wind energy harvesting, however due to the increased friction losses of the bearings and the reduced surface area of the blades, the efficiency of conventional turbines reduces with size. These devices reviewed above are summarised in Table 2.1. Power efficiencies in this table show the percentages of the wind kinetic energy that converted into electric output energy. In general, almost all reported

miniature wind energy harvester with rotor diameters smaller than 10 cm have practically low efficiency for specific range flow speed to date. For some miniature wind turbines, the rated wind speed is higher than the nominal ambient air speed. Therefore achieving lower threshold wind speed for operation is the main issue of such devices. Additionally, complicated mechanical structures and intricate fabrication processes also limit the minimization of rotary air-powered generators.

Table 2.1: A Summary of miniature wind turbines reviewed.

Authors	Type	Threshold wind speed (m/s)	Maximum Power Output (mW)	Efficiency
Rancourt *et al.*	Electromagnetic	5.5	130	9%
Holmes *et al.*	Electromagnetic	3	2.5	1.4%
Carli *et al.*	Electromagnetic	unknown	10	5.5%
Xu *et al.*	Electromagnetic	3	18	8%
Priya *et al.*	Piezoelectric	2.5	7.5	1%

2.3.2. Energy harvesters based on flow-induced vibration

When a structure is subjected to wind loads, the structure may experience unwanted, excessive vibrations due to aerodynamic instability phenomena. This kind of flow-induced vibration has been generally avoided in civil engineering to reduce possible damage. From a totally different perspective, such vibration has started to emerge recently as a novel approach based on wind power to generate electrical energy. Several distinct phenomena are known to excite flow induced vibrations of structures including vortex induced vibration, wake galloping and divergent oscillation (flutter). Figure 2.9 shows the typical velocity– amplitude curves of the aerodynamic instability phenomena [69].

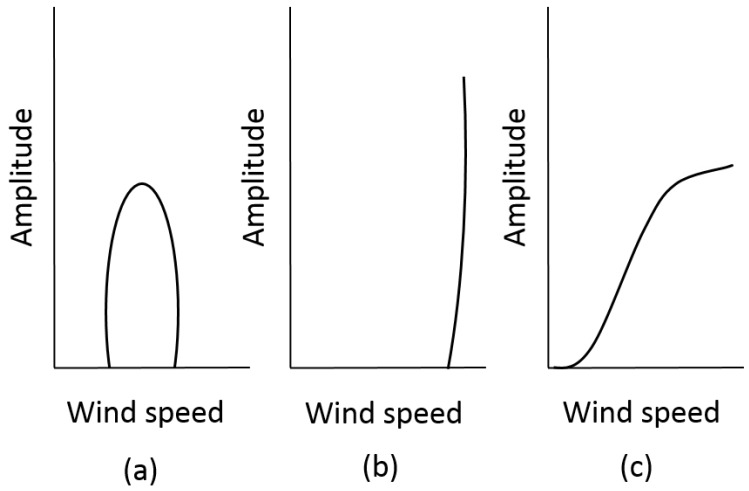

Figure 2.9: Typical velocity–amplitude curves of aerodynamic instability phenomena; (a) vortex-induced vibration, (b) divergent oscillations (i.e. flutter), (c) wake galloping. Reprinted from [69].

As shown in the figure, Vortex-induced vibration may occur at relatively low wind speed, but it occurs only within a very narrow range of wind speed along with relatively small amplitude. Therefore, an energy harvesting system based on vortex-induced vibration may be inefficient. The flutter-based energy harvesting system can dramatically improve the amplitude with increasing wind speed. However such devices only operate at very high wind speed and become unstable under unexpected flows. The wake galloping structures can operate at a wider range of flow speed, but suffer from drastic deterioration of efficiency at low speed levels.

2.3.2.1 Vortex induced vibration

Vortex induced vibration is one of the most classical-type aerodynamic instability phenomenon. It predominately occurs in bluff bodies such as bridge decks, smoke stacks, or heat exchanger tubing. When a fluid flows toward the leading edge of a bluff body, it will be slowed down while in contact with the surface of the bluff body as a result of viscosity, forming a boundary layer. This boundary layer can be separated from the body because of its excessive curvature. If the flow speed is higher than a critical value, pressure on both sides of the bluff body will change from stable free steam pressure to unstable stagnation pressure, and hence vortices are created. This phenomenon is called Vortex Street or Kármán Vortex Street as shown in Figure 2.10. In one limited range of flow speed, the exciting frequency may be close enough to one of the natural frequencies of the body, causing resonance and oscillations. Therefore certain transduction mechanisms can be applied to extract energy. Sanchez-Sanz and his colleagues [70] studied the feasibility of energy harvesting based on the Kármán vortex street and proposed several design rules of such micro-resonator. This method is suitable both air flow

and liquid flow. A preliminary study on harnessing energy from piezoelectric transducers by vortex-induced vibration phenomena was discussed by Sivadas *et al.* [71]. Different bluff-body shapes and dimensions are investigated, including cylindrical, triangular, and pentagonal. The simulation results obtained showed the cylindrical bluff body had a wider lock-in bandwidth, which means it can generate appreciable power over a wider range of flow speeds, and higher average power compared to the other two bluff body shapes investigated.

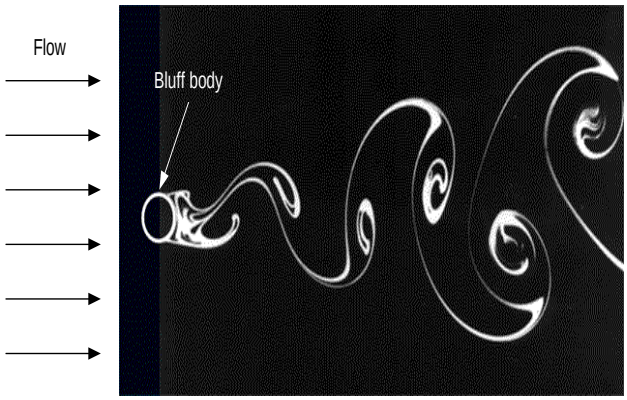

Figure 2.10: An example of Kármán Vortex Street.

Classical studies predict that the dominant exciter of this oscillation phenomenon should be when the vortex is shedding from the bluff body. Bernitsas *et al.* [72] proposed an energy harvesting device using vortex induced vibration and the idea has since then been further developed. Some researchers focused on this type of excitation [73], and the most famous energy harvester based on Vortex Street is the 'Energy Harvesting Eel' [74]. Figure 2.11 shows a schematic of the device. The 'eel' converts the flow energy to electrical power through a flow induced oscillating motion on the PVDF film behind bluff body. However, those devices are mostly used in liquid flow such as rivers or oceans [75–78].

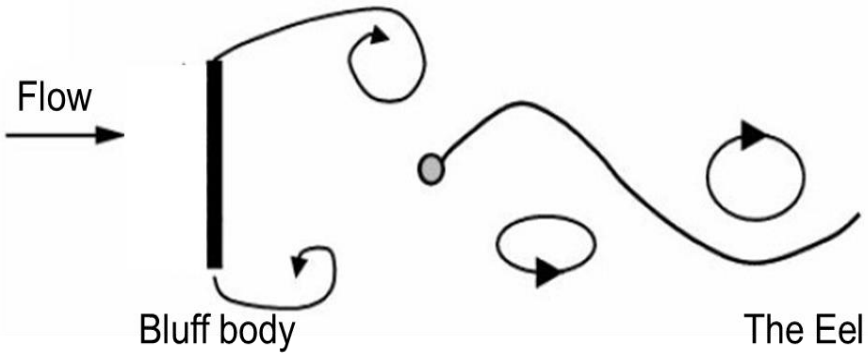

Figure 2.11: Schematic of the 'Energy Harvesting Eel' (top view).

A wind energy harvesting configuration, called flapping-leaf, has been reported by Li and Lipson as shown in Figure 1.22 [79]. The device consists of a PVDF cantilever with one end clamped on a bluff body and the other end connected to a triangular plastic leaf. When the airflow passes through, the vortex shedding, caused by the bluff body, generates harmonic force; meanwhile another unsteady force is induced by the trailing edge of leaf. Those two potential excitations generate unstably periodic motion of the flexible plate and thus the PVDF cantilever produces electrical energy. The energy harvester generated a maximum output power of 17 μW under the wind of 6.5 m/s. Dimensions of the PVDF cantilever is 73 mm × 16 mm × 40 μm. The same group explored another type of flapping-leaf with a dangling cross-flow stalk arrangement, which can amplify the vibration by an order of magnitude. They claimed that their architecture makes it appropriate for low-cost organic piezo-materials. Experimentally, the prototype produced a peak output power of approximately 600 μW in the wind of 8 m/s [80].

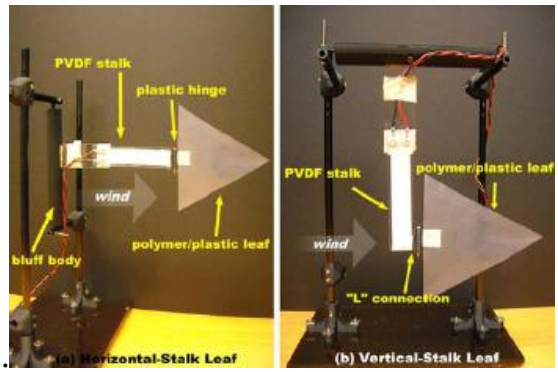

Figure 2.12: Different configurations of piezo-leaf. Reprinted from [79].

Kwon *et al.* also implemented a leaf-like design for a piezoelectric harvester with two different kinds of piezoelectric materials. The soft flexible one is used to make the leaf element, while the hard one is applied to the trunk portion of the tree requiring rather strong winds to generate any power. Results showed the power output was insufficient for powering a wireless network node [81].

Dunnmon *et al.* [82] reported a piezoelectric aeroelastic energy harvester. It consists of a flexible plate with piezoelectric laminates which is placed behind a bluff body. It is excited by a uniform axial flow field in a manner analogous to a flapping flag such that the system delivers power to an electrical impedance load. In this case, the bluff body is in the shape of an aerofoil rather than a cylinder. The beam is made of aluminium and an off-the-shelf piezoelectric patch is mounted close to the clamped end of the beam. Experimental results showed that an output power of 2.5 mW can be derived under a wind of 27 m/s. The plate has dimensions of 310 mm

× 101 mm × 0.39 mm and the bluff body has a length of 550 mm. Dimensions of the piezoelectric laminate are 25.4 mm × 20.3 mm × 0.25 mm.

Wen *et al.* [83] proposed a fluid kinetic energy harvester excited by vortex induced vibration. In order to optimize the harvester, they used a two-way Fluid Structure Interaction (FSI) simulation to investigate the performance. The harvester was assembled with a cuboid-shaped aluminium bluff body and a piezoelectric polymer (PVDF) cantilever in size of 60 mm × 12 mm × 52 μm. The test results showed that the energy harvester delivered 1 μW power output. Researchers from University of Brescia [84] have also reported a VIV energy harvesting system based on a piezoelectric converter to power autonomous sensors. The convertor was embedded as a part of a flexure beam (45 mm long and 20 mm wide) with a blade (70 mm long and 30 mm wide) and a bluff body placed upstream. The results of experimental characterization showed a harvested power up to 100 μW was obtained at a flow speed of 4m/s.

Weinstein *et al.* proposed a cantilevered piezoelectric beam for energy harvester used in HVAC flow. Excitation is amplified by the interactions between an aerodynamic fin attached at the end of the piezoelectric cantilever and the vortex shedding downstream from a cylinder shaped bluff body placed in ahead of the cantilever assembly (Figure 2.13). The positioning of small weights in the form of magnets were placed along the length of the fin to adjust the resonant frequency of the bender. The energy harvester was test to operate at flow velocities from 2 to 5/m s with power generation of 200 μW to 3 mW respectively with a dimension of 22.5 cm long and 11 cm wide [85].

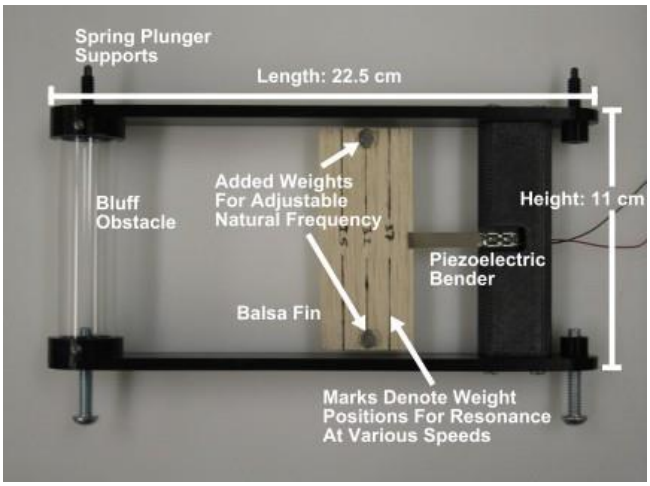

Figure 2.13: Schematic of the cantilevered piezoelectric beam. Reprinted from [85].

2.3.2.2 Wake galloping

Wake galloping is known to occur in parallel cylinders because of the wake interference

between two circular cylinders. Under certain conditions the leeward cylinder may be subjected to galloping oscillations induced by the turbulent wake of the windward cylinder. Figure 2.14 shows the schematic of this phenomenon. The vibration orbit depends upon the arrangement of parallel cylinders. However, there were some incidences that these devices were damaged by strong forces due to the wake galloping.

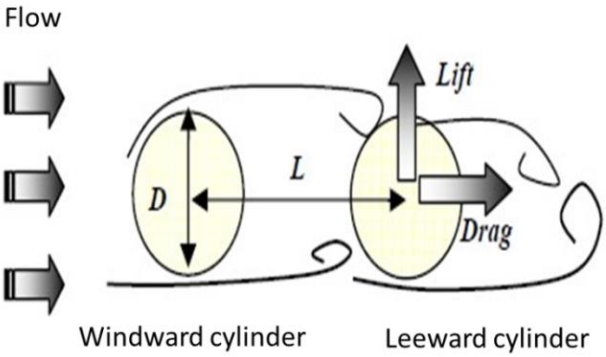

Figure 2.14: Schematic of wake galloping phenomenon.

Numerical investigations for two circular cylinders in different arrangement have been reported since 1973 [86] and researchers found that if the distance between two cylinders is approximately six times larger than the diameter, the vibration does not appear. Jung *et al.* [87] proposed an energy harvesting devices based on the wake galloping phenomenon for the first time. Tests results showed that with two cylinders with lengths of 85 cm and diameters of 5 cm, a maximum power of 1.13 W was measured under wind speed with 5.6 m/s. Later, a more detailed investigation followed their conceptual study was reported by Jung and Lee [88]. In order to validate the effectiveness of the wake galloping-based energy harvesting system clearly, a prototype device with electromagnetic induction was designed and manufactured as shown in figure 2.15. In the experiment, the prototype device produced an average output power of 370 mW under wind of 4.5 m/s.

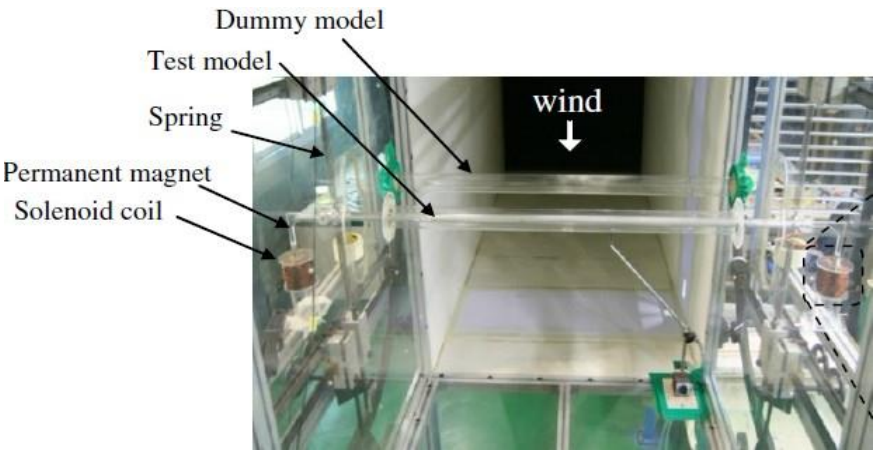

Figure 2.15: A prototype of the wake galloping-based energy harvesting system. Reprinted from [88].

2.3.2.3 Flutter

Flutter is a self-feeding and potentially destructive vibration where aerodynamic forces on an object couple with a structure's natural mode of vibration to produce rapid periodic motion. It happens when the natural mode of vibration for this object couples with the aerodynamic forces applied on it. When the natural damping of the system is smaller than the aerodynamic excitation, the vibration will keep increasing until the aerodynamic or mechanical damping of the object matches the energy input. This phenomenon leads to large amplitude of the oscillation for a stable nonlinear limit cycle to emerge or a rapid structure failure of the system in divergent behaviour due to an increased wind speed. Consequently, the study of this phenomenon was initiated in the field of aeronautics to aerodynamically stabilize aerofoils.

The possibility of the idea that utilising aerodynamic instability phenomena for energy harvesting was first addressed by Duncan in 1948 [89]. Since then, some researches has been carried out for developing energy harvesting systems based on this phenomena, more specifically divergent oscillation due to the flutter. In the early 1980s, McKinney and DeLaurier [90] proposed a prototype power generating device called windmill based on the flutter phenomenon. They carried out wind tunnel tests and demonstrated that their device had an efficiency of 10% approximately, which was comparable to a conventional windmill. In 1997, Jones *et al.* [91] described their numerical and experimental methods for an oscillating rectangular wing generator. Their study found that an oscillating wing would be suitable for some power generation application, if the pitch amplitude exceeded the induced angle of attack owing to the plunging motion. In 2003, Isogai *et al.* [92] proposed a different type of energy harvesting device using a flapping wing under the flutter phenomenon. They introduced an electric motor to mechanically drive the pitching oscillation of the wing. The result showed an increased efficiency of the system.

Erturk *et al.* [93] reported the use of a curved aerofoil section with piezoceramics for energy harvesting as shown in Figure 2.16. A mathematical model was established and a prototype device was built to validate the model. The generator has a 0.5 m long aerofoil vertically placed. Two PZT-5A piezoceramics were attached onto the two ends of the aerofoil. Under certain airflow, the aerofoil flaps and actuates the piezoceramics to produce electricity. An electrical power output of 10.7 mW was achieved at the linear flutter speed of 9.3 m/s.

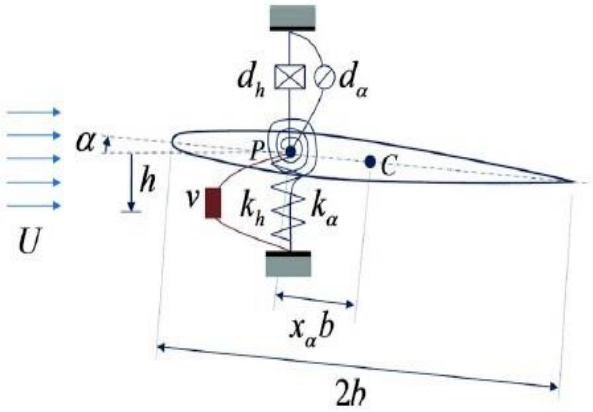

Figure 2.16: Schematic of a piezoaeroelastic section under uniform airflow. Reprinted from [93].

Zhu *et al.* [94] investigated the performance of a new type of flow energy harvester based on oscillating foils through numerical modelling by using 2D and 3D models. By examining the power extraction capacity and efficiency of the system at various geometrics including mechanical and kinematic parameters, the optimal performance of the system was achieved in the case when there is no spring, and the pitching axis is located at the centre of the chord. They also found that the presence of the ground increases the heaving response of the foil due to the blocking of trailing vortices, and greatly enhances both the power extraction and the efficiency.

Kwon published a T-shaped piezoelectric cantilever for generating electric power from fluid flow. The working principle of the device is based on aeroelastic flutter and utilizes a bimorph cantilever with T-shape which hastens occurrence of flutter at a low fluid speed. A prototype device (100 mm × 60 mm × 30 mm) was tested in a wind tunnel. The device was found to provide power from a wind speed of 4 m/s and a continuous peak electrical power output of 4 mW [95].

Bryant and Garcia [96] proposed a novel energy harvesting device powered by aeroelastic flutter vibrations to generate power on a helicopter rotor blade. The model of a simple wing connected to the tips of a pair or bimorph piezoelectric beams has been derived by fusing the governing mechanical, electromechanical, and aerodynamic terms of the system. One design for such a power harvester is detailed and the electromechanical behavior of the system has been predicted. The same group then designed another aeroelastic energy harvester consisting of an aerofoil section attached to a cantilevered piezoelectric bender by a flexural joint, as illustrated in Figure 2.17, both theoretically and experimentally [97-100]. The beam was made of Stainless steel with a size of 250 mm × 25 mm × 0.38 mm, attached with PZT piezoceramics. This configuration creates an aeroelastic flutter response above a critical cut-in wind speed, allowing the system to generate vibrations from the airflow and directly transduce the

vibrations to electrical energy. A model based on simple two degree aeroelastic system of this device has been developed to examine the effects on the cut-in wind speed of the system when several design parameters are tuned and the size and mass of the system is held fixed. Experimental results showed an output power of 2 mW at a wind speed of 7 m/s.

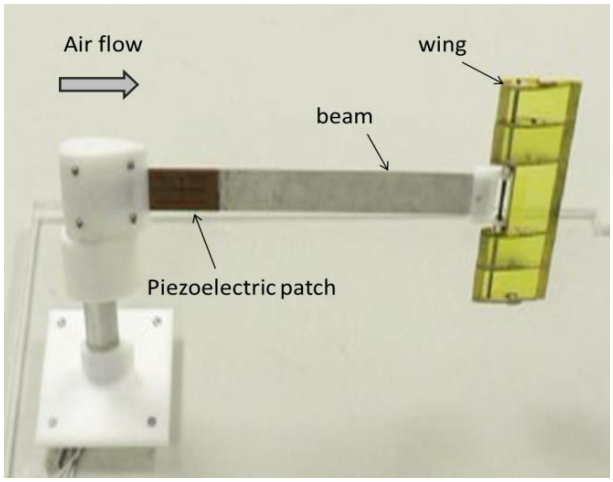

Figure 2.17: Photograph of the aeroelastic power harvester design. Reprinted from [99].

Researchers from Stanford University [101] investigated the efficiency of an aero-elastic-flutter based energy harvester with wind speed augmenting funnel incorporated (Figure 2.18). The wind-flow-contracting funnel device was designed to direct the wind flow to the flutter and magnify the wind speed. Tests showed that the wind speed was magnified up to approximately 20 % by the funnel within an incident angle of 30°, which leads to an increase in the voltage output of the device.

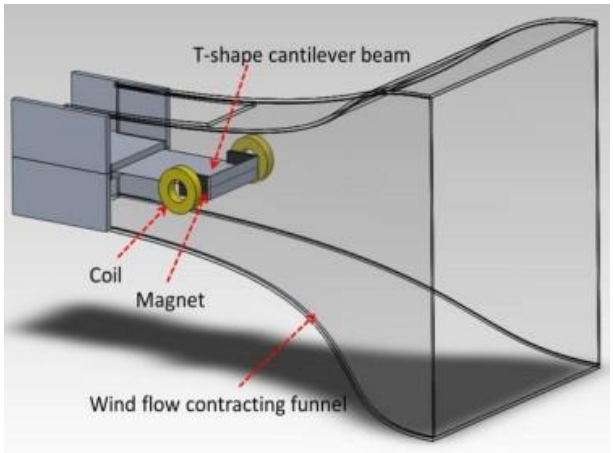

Figure 2.18: Photograph of the aeroelastic power harvester with wind funnel. Reprinted from [101].

All of the studies mentioned previously were focused on flapping-wing type power generators

based on the flutter phenomenon, which could be inspired from oscillating wings in an aircraft.

Humdingers windbelt is a flapping wind generator that has been proposed by Shawn Frayne and his team in 2004 as shown in Figure 2.19 [102]. It uses a tensioned membrane for the flutter oscillation to collect energy from the wind. Magnets are attached to the end of the membrane. They move with the membrane and are coupled with static coils to generate electricity. The smallest Windbelt, with a 12 cm × 0.7 cm membrane, can provide an output power less than 100 μW with minimum wind speed of 3 m/s.

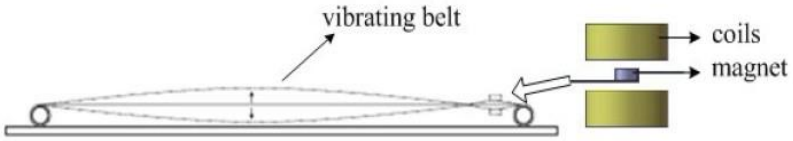

Figure 2.19: Schematic of a windbelt. Reprinted from [102].

Pimentel [103] and his group presented a characterization of the wind flutter generator with a 50 cm long windbelt. After several parameters taken into account, experimental results showed the peak output power was 5 mW with wind speed of 3.6 m/s. Fei *et al.* [104] also designed a wind energy converter using windbelt structure which has a better performance than previous one. By optimizing of the location of the generator coils and the magnet using FEM tools, they achieved a peak output power of 7 mW at 2.8 m/s wind speed.

Kim *et al.* from Georgia Institute of Technology has presented an electromagnetic generator using windbelt-based vibration [105]. As shown in Figure 2.20, it consists of a polymer resonator with embedded permanent magnets, polymer housing, and copper windings with a size of 12 mm × 12 mm × 6 mm. The resonator produces high frequency mechanical oscillation from air-flow with the motion of vibrating membrane in the middle, then converses it to electrical power with permanent magnet system. The epoxy housing located inlet and outlet airflow ports is used to maximize the energy conversion efficiency. In experiment, this generator produced a peak-to-peak output voltage of 81 mV from an input pressure of 50 kPa.

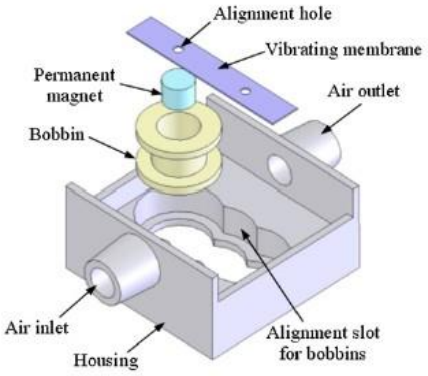

Figure 2.20: Three-dimensional schematics of the windbelt vibration energy harvester. Reprinted from [105].

Sun *et al.* reported a PVDF microbelt to convert the energy from low-speed air flow to electricity via their resonant oscillation. The micrometre thick PVDF thin films were fabricated by a top-down reactive ion etching process. With measures to improve surface smoothness, the thickness could be controlled down to a submicron level. MB structures made from the PVDF thin films were shown to oscillate under low speed air flow around 1 m/s. A continuous 12 minutes of simulated respiration produced a capacitor voltage output of 200 mV, corresponding to 20 mJ of electrical energy storage [106].

St. Clair *et al.* reported a micro generator using flow-induced self-excited oscillations of a piezoelectric beam embedded within a cavity [107]. The principle is similar to music-playing harmonicas as shown in Figure 2.21. When the flow rate of air past the beam exceeds a certain threshold, the energy pumped into the structure via nonlinear pressure forces offsets the system's intrinsic damping setting the beam into self-sustained limit-cycle oscillations. Output power between 0.1 mW and 0.8 mW was obtained at wind speeds of 7.5 m/s and 12.5m/s. They emphasized that their device can eliminate the bandwidth issues associated with resonant vibratory energy harvesters. Similar device has also been developed by Ji *et al.* which has impressive mill watt scale power outputs but suffers from a cut-in speed around 3 m/s [108].

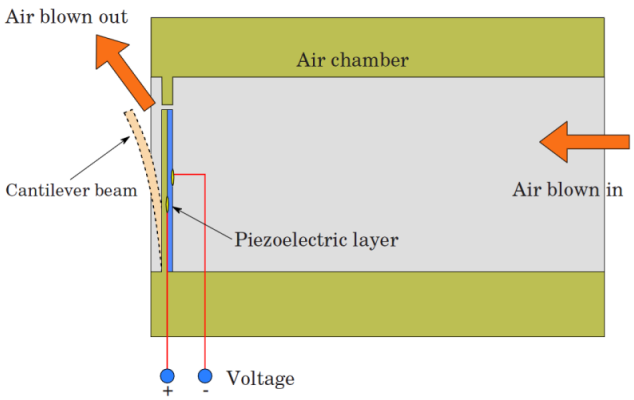

Figure 2.21: Energy harvesting using flow-induced self-excited oscillations. Reprinted from [107].

Researchers from Kangwon National University designed a piezoelectric MEMS energy harvester using flow-induced vibration as shown in Figure 2.12 [109]. They used parasitic flow as the input energy harvester, where reduction of the natural frequency of the harvesters is a vital factor. The micro harvester was composed of one silicon cantilever coated with piezoelectric thin film with a size of 610 μm × 300 μm × 3.5 μm. When the bent micro-cantilever was exposed to wind, the structure undergoes flow-induced vibration which resulted in electrical power based on piezoelectricity. In the experiments, this harvester generated voltage of 0.44 V, 0.62 V and 0.82 V at the flow speed of 6.1 m/s, 12.4 m/s, and 21.6 m/s, respectively. However, no specific power output was mentioned. The harvester was further investigated in a recent published paper by changing the geometrical properties of engineering structures [110]. In this work, four silicon cantilevered with PZT film were used, each of which has a length of 2,000 μm, a width of 200 μm, and a thickness of 3.5 μm. After testing, an output power of 1.77 μW and an output voltage of 1.88 V was achieved at flow velocity of 12.4 m/s.

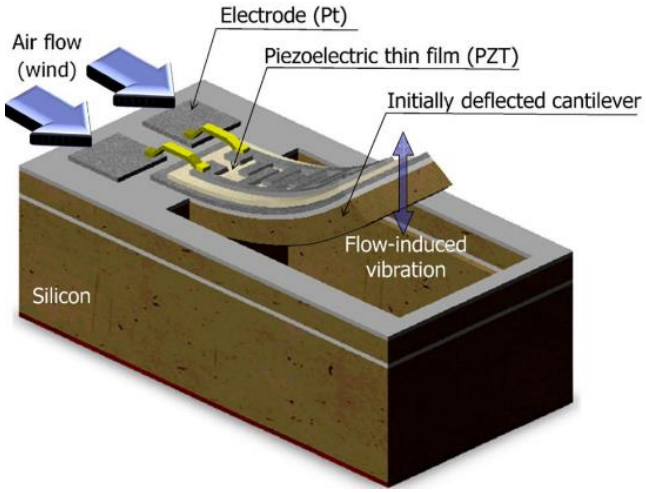

Figure 2.22: The structure of piezoelectric energy harvester using flow-induced vibration. Reprinted from [109].

Recently, Wang and his group proposed a flow-induced triboelectric nanogenerator (TEGs) for wind energy harvesting [111]. The mechanism is based on the contact/separation between two triboelectric materials to drive the electrons flow in the external circuit because of the coupling between triboelectrification and electrostatic induction. The generator consisted of two Al foils and a fluorinated ethylene propylene (FEP) film in a cuboid acrylic tube, as illustrated in Figure 2.13. The Al foil plays dual roles as a triboelectric surface and as an electrode. One side of the FEP film was fixed in the middle of the end surface of the tube, leaving the other side free-standing. The distance between the two Al foils and the FEP film can be changed periodically

due to the vibration of the FEP film, resulting in an output voltage/current across an external loading resistor. A prototype with dimensions of 2.5 cm × 2.5 cm × 22 cm was tested and an output power of 0.16 mW at a wind speed of 10 m/s was obtained. To optimise the output performance of harvester, the device sizes and the film material were further investigated. In another paper, an improved TEG was fabricated and tested [112]. The new device had a total size 22 mm ×10 mm × 67 mm, and a triboelectric polytetrafluoroethylene (PTFE) film was used between the Al foils. The best performance of the generator was 3.7 mW power output at wind speed of 7.6 m/s. The same group also reported a hybridized nanogenerator integrating TENGs and the electromagnetic generators (EMGs) to enhance the output performance of the device [113]. A prototype that consisted of two TENGs and two EMGs was fabricated with dimensions of 6.7 cm × 4.5 cm × 2 cm. This device can deliver an output power of 3.5 mW from one TENG and 1.8 mW from one EMG under an air-flow speed of 18 m/s.

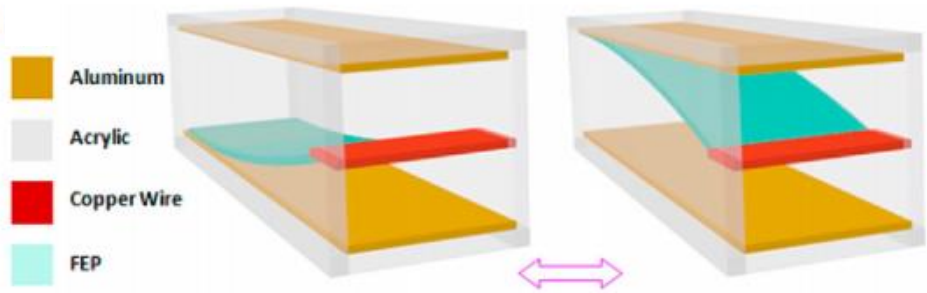

Figure 2.23: Schematic of a triboelectric nanogenerator for wind energy harvesting .Reprinted from [111].

Another flow-induced energy harvester based on aeroelastic flutter vibrations was reported by Zhu *et al.* [114] shown in the following Figure 2.24. The generator consists of a wing attached to a cantilever spring made of beryllium copper. The airflow over the wing causes the cantilever to bend upwards, the degree of bending being a function of the lift force from the wing and the spring constant. As the cantilever deflects downwards, the flow of air is reduced by the bluff body and the lift force reduced causing the cantilever to spring back upwards. This exposes it to the full airflow again and the cycle is repeated. When the frequency of this movement approaches the resonant frequency of the structure, the wing has the maximum displacement. A permanent magnet is fixed on the wing while a coil is attached to the base of the generator. The movement of the wing causes the magnetic flux cutting the coil to change which generates electrical power. The proposed device has dimensions of 12 cm × 8 cm × 6.5 cm. This generator can operate at wind speeds as low as 2.5 m/s with a corresponding electrical output power of 470 μW. This is sufficient for periodic sensing and wireless transmission. When the wind speed is 5 m/s, the output power is 1.6 mW.

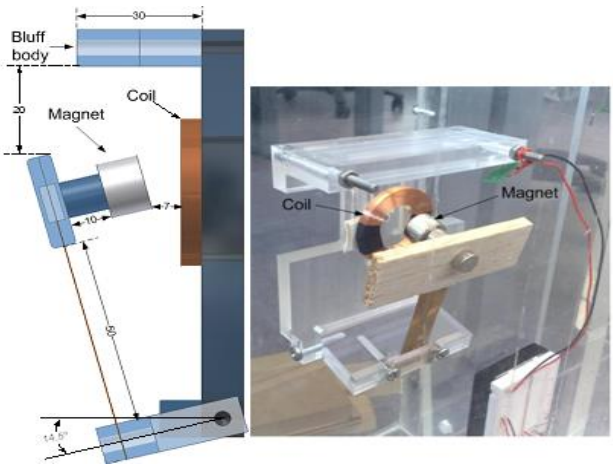

Figure 2.24: Schematic of the cantilever-based electromagnetic wind generator. Reprinted from [114].

A summary of all flow-driven devices reviewed in this section is listed in Table 2.2. To calculate the efficiency, the windward sweeping area was calculated by measuring the width of the flapping part and the vibration amplitude. In some papers, these values were not clearly listed, however the value could be estimated by the size and the movement of the device. This made the efficiency calculated not as accurate as the others, therefore the values were only used as a guide for comparison. Again the efficiencies at different speeds were calculated and the maximum one was chosen for comparison

Table 2.2: A summary of the flow-driven devices.

Authors	Type	Threshold wind speed (m/s)	Maximum Power Output (mW)	Efficiency
Jung *et al.*	Electromagnetic	2.5	370	unknown
Pimentel	Electromagnetic	3.6	5	unknown
Zhu *et al.*	Electromagnetic	2.5	1.6	1.2%
Fei *et al.*	Electromagnetic	2.8	7.5	unknown
Humdinger	Electromagnetic	3	0.1	unknown
Kim *et al.*	Piezoelectric	unknown	0.0017	4.2%
Demori *et al.*	Piezoelectric	4	0.1	unknown
Dunnmon *et al.*	Piezoelectric	unknown	2.5	0.002%
Wen *et al.*	Piezoelectric	unknown	0.001	0.58%
Clair *et al.*	Piezoelectric	unknown	0.8	unknown
Li *et al.*	Piezoelectric	4	0.6	0.04%
Weinstein *et al.*	Piezoelectric	2	3	0.93%

Erturk *et al.*	Piezoelectric	9.3	10.7	unknown
Kwon *et al.*	Piezoelectric	4	4	unknown
Bryant *et al.*	Piezoelectric	2	2.2	0.18%
Ji *et al.*	Piezoelectric	2.8	4.5	unknown
Wang *et al.*	Electrostatic	>6	0.16	0.04%

2.3.3. Energy harvesting from Helmholtz resonators

A Helmholtz resonator, which is a type of acoustic resonator, consists of a cavity full of gas connected to the environment through a narrow neck. When air flows past the opening, an oscillation wave occurs. A volume of air in and near the open neck vibrates because of the 'springiness' of the air inside. The pressure in the cavity is relatively uniform, and the air in the neck oscillates as a single mass. Generally, the cavity has several resonance frequencies, the lowest of which is the Helmholtz resonance. The Helmholtz resonant frequency is given by:

$$f = \frac{c}{2\pi}\sqrt{\frac{S}{VL}} \qquad \text{(Equation 2.2)}$$

Here c is the speed of sound in a gas; S is the cross sectional area of the neck; L is the length of the neck and V is the volume of the cavity.

Helmholtz resonators are mostly applied for acoustic energy harvesting, which capture energy from ambient acoustic field [115]. According to the current review, the published studies on wind energy harvesting based on Helmholtz resonator are limited. In most cases, the energy converters are placed at the bottom of the Helmholtz resonators.

A Helmholtz resonator based generator designed for weaker airflow was reported by Liu *et al.* [116]. It comprises a gas-filled chamber with an open neck, where the oscillation occurs. As the membrane oscillates due to the Helmholtz resonance, a static coil is coupled with the moving magnet to generate electricity. Two energy harvesters were fabricated and tested. The first one has a dimension of 19 mm × 5 mm and a resonant frequency of 1.4 kHz. It generated an open circuit voltage of 4 mV_{pp} under the airflow of 0.2 kPa (5 m/s). The second device has a dimension of 9 mm × 3 mm and a resonant frequency of 4.1 kHz. It generated an open circuit voltage of 15 mV_{pp} under the airflow of 1.6 kPa.

Matova *et al.* [117] reported a device that has a packaged MEMS piezoelectric energy harvester inside a Helmholtz resonator shown in Figure 2.25. It was found that packaged energy harvesters had better performance than unpackaged energy harvesters as the package removes

the unwanted viscous influence and provides only vibration excitation to the energy harvester. Experimental results show that the energy harvester generated a maximum output power of 2 μW at 309 Hz under the airflow of 13 m/s.

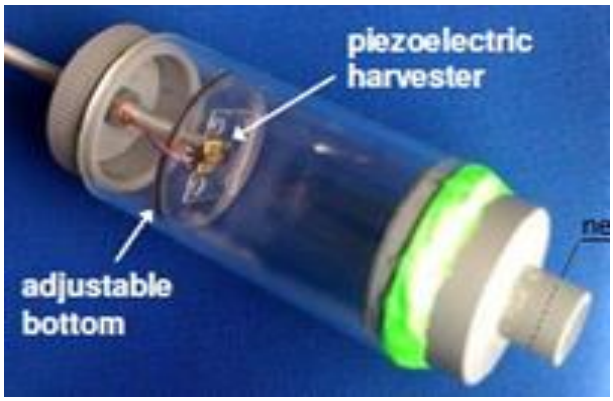

Figure 2.25: Helmholtz resonator with the piezoelectric cantilever harvester. Reprinted from [117].

Compared to other wind energy harvesting techniques, reclaiming wind energy using Helmholtz resonator has received less attention. A major drawback of this kind of device is the strong dependence of resonant frequency on the ambient temperature. This means that energy harvesters with Helmholtz resonators can only be used in the environments with stable temperature.

2.4 Conclusion

The recent development of wind energy harvesting are introduced and reviewed in this chapter. The main methods of capturing flow energy include wind turbines, flow-induced vibration and Helmholtz resonators. Based on the current literature review, low efficiency, high threshold wind speed for operation as well as complicated fabrication process is the main issues of miniature wind turbine systems. Alternative approaches for replacing these conventional blade type wind power systems have been investigated in recent years. Due to the temperature limitation of Helmholtz resonators, most researchers put their emphasis on flow-induced vibrations.

Most flow-induced structural harvesters take the form of beams cantilevered to a vibrating base object and tuned to resonate at the vibration frequency of the base object. These cantilevered based generators have relatively low threshold wind speed for operation than other structures in the review. In this project, a flow induced energy harvester with a flapping beam is proposed, which represents a novel opportunity that may achieve low threshold wind speed of operation

as well as large amplitude. The generator has a cantilever beam attached by an aerofoil for limit cycle oscillation behind a bluff obstacle in the airflow. As all reviewed devices are developed to operate at wind speeds above 2 m/s, a low threshold wind speed (1.5 m/s) is the first strategy in this work. In addition, this structure of harvester provides relatively high performance at low flow speeds and the efficiency can dramatically improve with increasing wind speed. However the scaling effect of such structure is unknown. Hence it may have better performance than rotary harvesters at some scales. In order to investigate that, the work by Zhu *et al.* will be used as a reference. Generally the smaller the size of the energy harvester the better it is for miniature systems application. However, considering that the output power reduces significantly with the size of the generator scaling down, an optimum design is required to balance both power generation and size of the device. Hence another goal pursued in the report is to achieve higher power densities than the previous device with smaller sizes.

Since most wind turbines use conventional electromagnetic transducers in the literature review, there is little progress made in piezoelectric windmills due to their low adaptability. On the other hand, most flow-induced wind harvesters, especially with miniature sizes, are piezoelectric generators. Among them, flexible materials like piezoelectric polymers give low surface energy density because of low piezoelectric coefficient; and high performance material like bulk piezoelectric ceramics have limitations in size due to large thicknesses. In this situation, film piezoceramics are more favourable to fabricate devices with small thicknesses. Further investigations on designing proper transduction systems will be discussed in the following chapters.

Chapter 3 Theory

This chapter explains some relating theory to the wind energy harvester that would be used for concept design.

3.1 Oscillation under Air Flow

Unlike the flow-induced harvesters reviewed in Chapter 2, the operation of the cantilever oscillation in this work is still not fully understood. However, some parts of the operation can be speculative based on the ANSYS model which will be discussed in details in the following chapter. As shown in Figure 3.1, an aerofoil is attached to one end of the cantilever spring while the other end is clamped. If there is no wind, the aerofoil will slightly bend downward due to its mass. When air is flowing towards the aerofoil, it will bend as shown in Figure 3.1(b). The degree of bending is related to the spring constant, mass and the lift/drag force form the aerofoil caused by the air flow. In this condition, however, the cantilever will remain stationary with a fixed deflection without oscillation. In order to oscillate the cantilever, a bluff body is required to be placed in front of the cantilever as shown in Figure 3.1(c). The bluff body will induce differences in velocity distributions above and under the surface of the aerofoil which causes the lift force to be asymmetric with deflection and varies the direction of deflection of the cantilever. The bluff body serves to reduce the flow of air which reduces the lift force when the cantilever is deflecting. In this case, the cantilever is operating mainly under inertial effects and will spring back. However when the cantilever springs back to the original position where the aerofoil can be fully exposed to the airflow again, the cycle is repeated. The amplitude of displacement increases until it reaches its steady state motion, which almost resembles harmonic forced vibration. Such a configuration can self-start and sustain the necessary oscillations under uniform and steady flow conditions. In addition to this advantage, such a harvester will potentially operate at a lower flow speed.

By attaching the aerofoil to the opening end, the deflection of the beam can be larger and its response can be better tuned for various flows. The position of the bluff body, both its distance to the cantilever and its height is of significance to the oscillation of the cantilever. The system can then resonate through both tuning the resonant frequency of the cantilever spring as well

as appropriate design and positioning of the bluff body. Specific theory of the generator with cantilevered structure, theoretical model of piezoelectricity, static aeroelasticity and aerodynamic characteristics of the aerofoil will be discussed in the following sections.

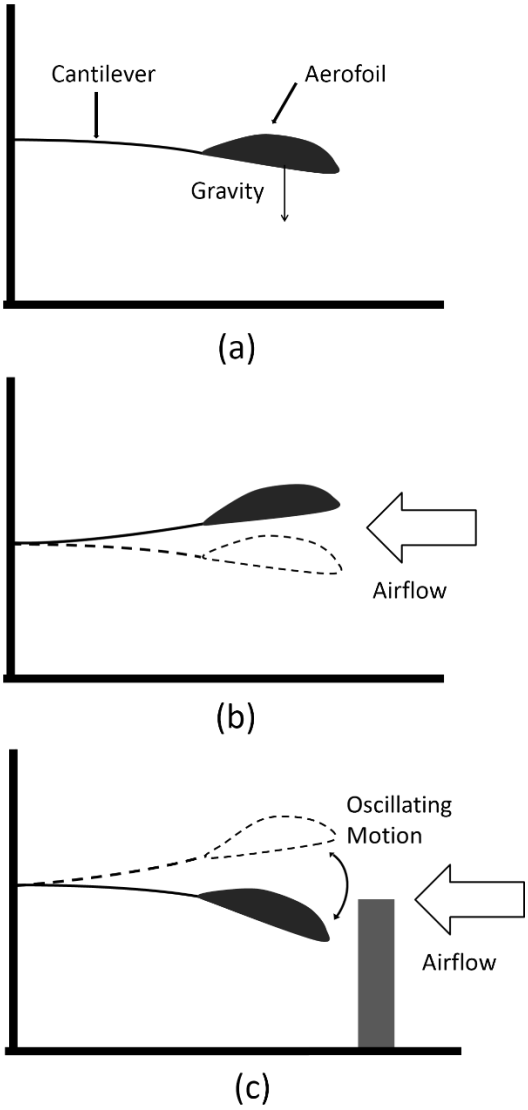

Figure 3.1: Schematic showing the operation of the cantilever oscillation.

The natural frequency of the cantilever oscillation f_n can then be calculated by:

$$f_n = \frac{1}{2\pi}\sqrt{\frac{k}{m}} \qquad \text{(Equation 3.1)}$$

Where *k* and *m* are the stiffness and the total mass of the beam, respectively. The stiffness k can be obtained by the following equation:

$$k = \frac{3EI}{L^3} \qquad \text{(Equation 3.2)}$$

The total mass is the sum of the effective mass of end mass and the mass of cantilever and can be given by:

$$m = m_{cantilever} + m_{eff} = 0.2235\rho L + m_{eff} \qquad \text{(Equation 3.3)}$$

and the natural frequency of the beam can be written as:

$$f_n = \frac{1}{2\pi}\sqrt{\frac{k}{m}} = \frac{1}{2\pi}\sqrt{\frac{3EI}{(0.2235\rho L + m_{eff})L^3}} \qquad \text{(Equation 3.4)}$$

where

E is the Young's modulus of the beam	k is the stiffness of the beam
I is the area moment of inertia	f_n is the natural frequency of the beam
L is the active length of the beam	$m_{cantilever}$is the mass of cantilever
ρ is the mass per unit length of the beam	m_{eff} is the end mass

According to this equation, for a set material, the natural frequency of beam is related to the effective end mass and the active length of the beam. The frequency therefore can be decreased by either increasing the active length or the effective end mass. In other words, known values of elastic modular E and the density of material, by varying the thickness, width, active length of the cantilever, its stiffness and natural frequency can be predicted theoretically. Then it was possible to design a cantilever suited to fit the desired stiffness and frequency.

3.2 Power of Wind

The power generated by a wind generator is originated from the wind power. The theoretical wind energy can be calculated from the standard formula for the kinetic energy approximation of a moving system:

$$E = \frac{1}{2}mv^2 \qquad \text{(Equation 3.5)}$$

Here m is the total mass of air at the windward area while v is the wind speed. The air mass can be given by

$$m = \rho A v \Delta t \qquad \text{(Equation 3.6)}$$

where ρ is the air density, A is the windward area for the device and Δt is the period of time over which the calculation is performed. Hence, the kinetic energy becomes

$$E = \frac{1}{2}\rho A v^3 \Delta t \qquad \text{(Equation 3.7)}$$

From this equation, we can obtain the wind power simply by dividing the kinetic energy by the time:

$$P = \frac{1}{2}\rho A v^3 \qquad \text{(Equation 3.8)}$$

In this case, the power of the wind becomes a function of air density, and area as well as wind speed. The air density and the windward area for a device are fixed while the wind velocity can be changed and is proportional to its power.

3.3 Power of Generator

A mechanical model of a second order spring mass system, i.e. an inertial device, was was first proposed by Williams and Yates which consists of the base excitation of an elastically mounted seismic [118]. While the elastic mount is typically modelled as a coil spring, in practice a cantilever beam would provide both the flexibility and necessary constraint of the seismic mass. The means of energy extraction may consist of a magnetic seismic mass moving past a coil, or the beam may be fabricated from piezoelectric material. As far as the mechanical vibration is concerned, the combination of mechanical and electrical damping is treated as equivalent to linear viscous damping, which is proportional to velocity. The basic system can be considered as a second order spring-mass-damper model as shown in Figure 3.2.

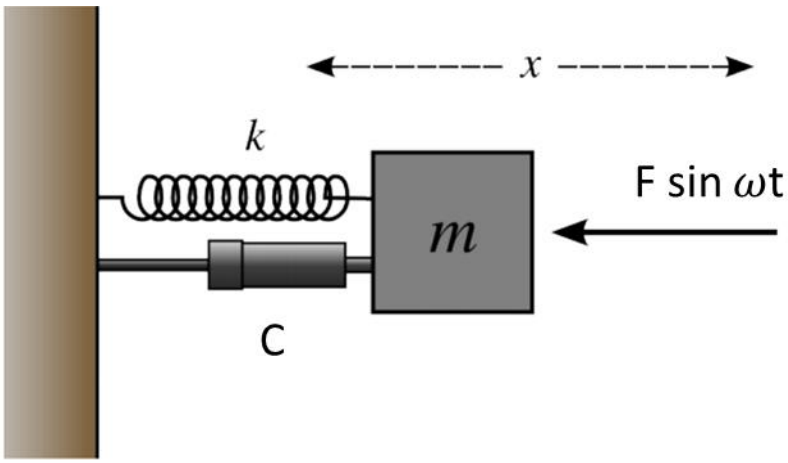

Figure 3.2: Schematic of a second order mass-spring-damper system.

In Figure 3.2, the model is subject to a sinusoidal force applied directly to the mass. Then the differential equation of motion is described as:

$$m\ddot{x} + c\dot{x} + kx = Fsin\omega t \qquad \text{(Equation 3.9)}$$

Where *k* is the stiffness of the cantilever; m is the proof mass added to the end of the cantilever; *c* is used to model the mechanical and electrical damping; and *x* is the displacement of the mass. The standard steady state response is

$$x = \frac{\omega^2}{\left[\frac{k}{m} - \omega^2\right]^2 + \left(\frac{c\omega}{m}\right)^2} Ysin(\omega t - \varphi) \qquad \text{(Equation 3.10)}$$

Where *Y* is the amplitude of vibration and the phase angle φ is given by:

$$\varphi = \tan^{-1}\left(\frac{c\omega}{k - m\omega^2}\right) \qquad \text{(Equation 3.11)}$$

The maximum power is extracted from the environment when the frequency of excitation is equal to the natural frequency, regardless of the damping ratio. Then the resonant frequency is given by:

$$\omega_r = \omega_n\sqrt{1 - 2\zeta^2} \qquad \text{(Equation 3.12)}$$

Here ζ is the damping ratio, while the natural frequency is

$$\omega_n = \sqrt{\frac{k}{m}} \qquad \text{(Equation 3.13)}$$

The power captured by the damper is described by the following equation by Williams and Yates [118]:

$$P = \frac{m\zeta Y^2\left(\frac{\omega}{\omega_n}\right)\omega^3}{\left[1 - \left(\frac{\omega}{\omega_n}\right)^2\right]^2 + \left[2\zeta\left(\frac{\omega}{\omega_n}\right)\right]^2} \qquad \text{(Equation 3.14)}$$

When $\omega = \omega_n$, the maximum power generated. Therefore Equation 3.10 can be reduced to

$$P_d = \frac{mY^2\omega_n{}^3}{4\zeta} \quad \text{(Equation 3.15)}$$

From equation above, it can be seen that a low damping factor is required for a higher power generation. However, the conclusion that the output power will be increase towards infinity as the damping ratio reduces towards zero cannot yet be made. Setting the damping ratio to zero implies that the system is no longer in a steady-state; therefore the equations are no longer valid. Besides it is clear from the above that the mass and the maximum displacement of the mass should be as large as possible within the size constraints to maximize the output power.

3.4 Theoretical Model of Piezoelectricity

The piezoelectric generator can be modelled by assuming a basic configuration (a bender mounted as cantilever with a mass on the end) based on beam theory and the piezoelectric constitutive equations:

$$\delta = {}^{\sigma}/_{E} + dQ \quad \text{(Equation 3.16)}$$

$$D = \varepsilon Q + d\sigma \quad \text{(Equation 3.17)}$$

where:

δ is mechanical strain
σ is mechanical stress
E is the modulus of elasticity (Young's Modulus)
d is the piezoelectric strain coefficient
Q is the electric field
D is the electrical displacement (charge density)
ε is the dielectric constant of the piezoelectric material

A model suggested by Roundy *et al.* [119] is presented here to better understand the electromechanical coupling behaviour of the piezoelectric generator. It is an analogous transformer model where the mechanical and the electrical domains of the piezoelectric system are modelled as circuit elements and the piezoelectric coupling is then modelled as a transformer as shown in Figure 3.3.

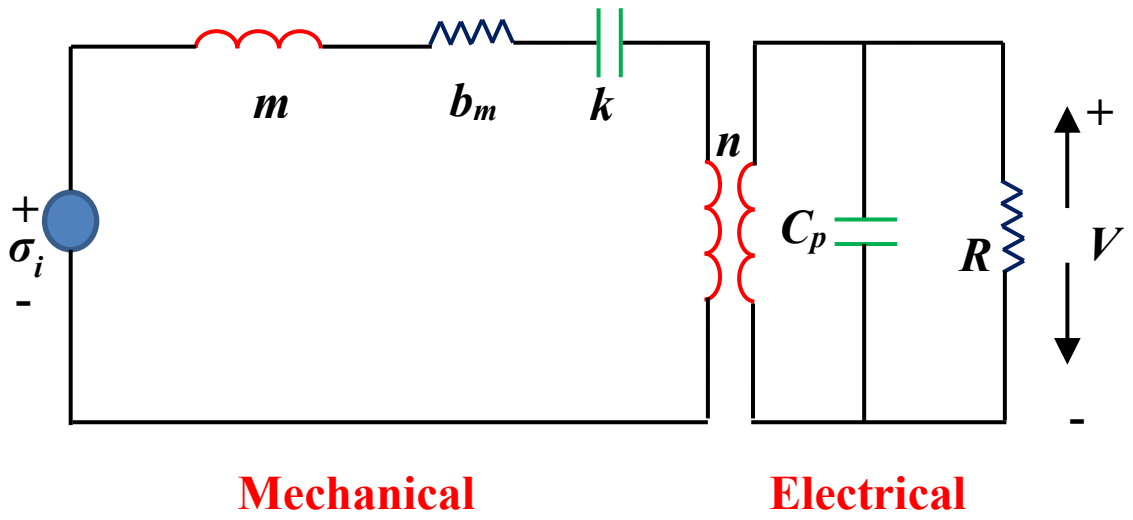

Figure 3.3: Circuit model of piezoelectric with resistive load.

The mechanical domain of the equivalent circuit at the left hand side consists of an inductor, a resistor and a capacitor which represent the generator mass, *m*, the mechanical damping, b_m, and mechanical stiffness *k*, respectively. For the electrical domain on the right, C_p is the capacitance of the piezoelectric and R is the external resistive load. *n* is the equivalent turn ratio of the transformer and is proportional to the piezoelectric charge constant. The vibration input is shown as a stress generator (σ_{in}) which originated from the input acceleration $A_{in.}$ The relation between input vibrations (A_{in}) and an equivalent stress can be written as:

$$\sigma_{in} = \frac{m}{b^{**}} A_{in} \qquad \text{(Equation 3.18)}$$

where b^{**} is the geometric constant relating average bending stress to force at the beam's end. The system equation can be developed by using Kirchoff's Voltage Law (KVL) and Kirchoff's Current Law (KCL) as:

$$\ddot{\delta} = \frac{-k_{sp}}{m}\delta - \frac{b_m b^{**}}{m}\dot{\delta} + \frac{k_{sp} d}{m t_c} V + b^{*} A_{in} \qquad \text{(Equation 3.19)}$$

$$\dot{V} = \frac{-k d t_c}{\varepsilon}\dot{\delta} - \frac{1}{R C_p} V \qquad \text{(Equation 3.20)}$$

where:

V is the voltage at the output

t_c is the thickness of a single layer of the piezoelectric material

k_{sp} is the equivalent spring constant of cantilever beam

b^* is the geometric constant relating average bending stain to force at the beam's end

The electrical coupling term in Equation (3.19), $\frac{k_{sp}d}{mt_c}V$, can then be used to find the equivalent linear damping ratio, ζ_e, which represents the electrically induced damping as presented in Equation (3.21):

$$\zeta_e = \frac{\omega K^2}{2\sqrt{\omega^2 + {}^1/_{(RC)^2}}} \qquad \text{(Equation 3.21)}$$

where K is the piezoelectric coupling coefficient and $K = \sqrt{\frac{E}{\varepsilon}d}$. It is an indication of the material's ability to convert mechanical energy to electrical energy [120]. The load resistance can then be adjusted to equalise the electrically induced damping ζ_e to the mechanically induced damping ζ_m to achieve an optimal output power. The optimal load resistance can then be given by:

$$R_{opt} = \frac{1}{\omega C}\frac{2\zeta_m}{\sqrt{4\zeta_m^2 + K^4}} \qquad \text{(Equation 3.22)}$$

and hence the optimal output power can be calculated as:

$$P = \frac{RC_p^2\left(\frac{kdt_c b^*}{\varepsilon}\right)}{(4\zeta_m^2 + K^4)(RC_p\omega)^2 + 4\zeta_m \mathrm{K}(RC_p\omega) + 2\zeta_m^2} A_{in}^2 \qquad \text{(Equation 3.23)}$$

The power output is proportional to the square of the acceleration magnitude of the driving vibrations and is inversely related to the frequency as can be seen directly from the equation. However, it should be noted that although a lower frequency will help increase the output power, the accompanied increase of the displacement of the proof mass may lead to an increased strain. As there is a limit on the maximum strain can be supported by the material, the power output is hence limited by the fracture strain of the piezoelectric material. In addition, although not immediately obvious from the expression in Equation 3.23, we can still conclude the output power is proportional to the proof mass as an increase of mass will lead to increases of other variables under a given frequency. For instance, with the increase of mass, either the thickness or the width of the beam must go up to maintain the same resonant frequency, this will consequently induce either an increase in both t_c and b^* or an increase of C_p, both of which will result in a higher predicted output power.

Although this model is used to calculate output power from vibration, it can also be adapted in

this work by relating A_{in} to the amplitude of the cantilever Y:

$$A_{in} = \omega^2 Y \qquad \text{(Equation 3.24)}$$

Equation (3.23) can then be further written as:

$$P = \frac{RC_p^2\left(\frac{kdt_c b^*}{\varepsilon}\right)}{\left(4\zeta_m^2+K^4\right)\left(RC_p\omega\right)^2+4\zeta_m K^2\left(RC_p\omega\right)+2\zeta_m^2}\omega^2 Y \qquad \text{(Equation 3.25)}$$

In this work, the oscillation amplitude of the cantilever is determined by the test wind speed. By establishing the relation between the amplitude and wind speed, this equation can then be applied to direct calculate the theoretical output power of the piezoelectric generator fabricated in this work at different wind speeds.

3.5 Theoretical Model of Electromagnetism

Most electromagnetic based energy harvesters use an inertial frame configuration, in which the relative movement between the magnets and the coils are induced by the vibration of the inertial frame. The voltage induced in the electromagnetic transducer is expressed by the Faraday's law as follows:

$$V = -N\frac{d\emptyset}{dz}\frac{dz}{dt} \qquad \text{(Equation 3.26)}$$

where N is the number of coil turns, z is the relative displacement between a magnet and the coil; $\emptyset$ is the magnetic flux. The induced voltage is proportional to the product of a magnetic gradient. Furthermore, the magnetic flux is proportional to the position of the inertial mass, which is determined by the geometries and the configuration of the coil and the magnet as well as the relative velocity between them. Consequently, the voltage across the idealized voltage source in the electrical domain can also be expressed as:

$$V(t) = \theta z'(t) \qquad \text{(Equation 3.27)}$$

where θ is the coupling coefficient. It can be written as $\theta = NlB$ and has units Vs/m. Here Nl and B are the effective length of the coil and the average flux density. From Equation 3.14, it can be seen that the maximum power generates when the exciting frequency coincides with the natural frequency of the system. Using the electromagnetic transduction, the amount of power generated is equivalent to the energy dissipated by the electromagnetic induction. Therefore

equation can also be expressed as

$$P_e = \frac{m\zeta_e Y^2 {\omega_n}^3}{4(\zeta_e+\zeta_m)^2} \quad \text{(Equation 3.28)}$$

Where $\zeta_m = c_m/2m\omega_n$ and $\zeta_e = c_e/2m\omega_n$, the electric damping coefficient c_e can be expressed as

$$c_e = \frac{(NlB)^2}{R_L+R_c+j\omega L_c} \quad \text{(Equation 3.29)}$$

where R_L, R_c and L_c are, respectively, the load resistance, the coil resistance and inductance. Based on above equation, to achieve high coupling factors, the coil should be designed with large effective length, which can be achieved by increasing the number of turns and using a larger area coil. Moreover, decreasing the coil resistance by using larger diameter wire is also an effective way.

The average power delivered to the load then can be expressed as

$$P_{load} = \frac{m\zeta_e Y^2 {\omega_n}^3}{4(\zeta_e+\zeta_m)^2}\left(\frac{R_L}{R_L+R_c}\right) \quad \text{(Equation 3.30)}$$

The maximum power can be transferred to the load by matching the load impedance to the source impedance. And the relationship is [121]

$$R_L = R_c + \frac{\theta^2 c_m {\omega_n}^2}{(k-m{\omega_n}^2)^2+(c_m\omega_n)^2} \quad \text{(Equation 3.31)}$$

where:

k is the spring stiffness

$c_m$is the mechanical damping coefficient

Considering the case at mechanical resonance by substituting in $\omega_n = \sqrt{k/m}$ in to equation 3.31 gives:

$$R_L = R_c + \frac{\theta^2}{C_m} \quad \text{(Equation 3.32)}$$

This equation has previously been derived by Stephen [122] as the resistive match at resonance,

taking coil resistance into account. It can be inferred that the optimum load is function of the coil resistance and the mechanical damping.

3.6 Aerofoil

In this work, an aerofoil was used as the wing of the power harvester. An aerofoil is a device designed to obtain useful reaction upon its surface from the air. When an aerofoil starts moving through the air, it is capable of producing lift. Wings, turbines and propellers are all examples of aerofoils. Operation of an aerofoil is based on Bernoulli's Principle, which states that the pressure of a fluid (liquid or gas) decreases at points where the speed of the fluid increases [123]. In other words, within the same fluid, such as air, high speed flow is associated with low pressure, and low speed flow with high pressure. This phenomenon is used to create lift. By making proper shape of the aerofoil, velocity of the wind above its surface is increased, therefore pressure above the aerofoil decreased. Simultaneously, the impact of the air on the lower surface of the aerofoil increases the pressure below. Then the higher pressure below is able to produce a perpendicular lift force on it.

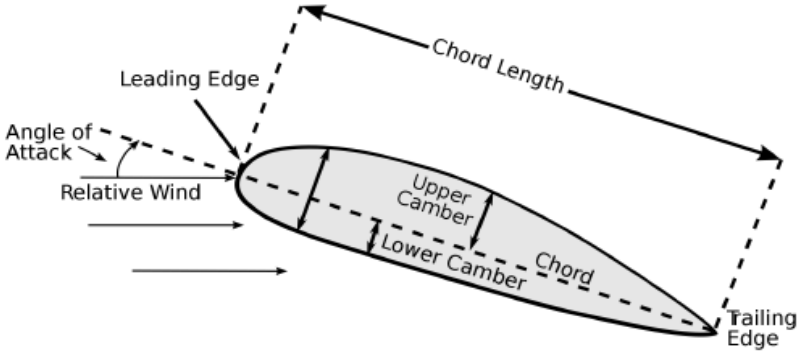

Figure 3.4: Schematic of an aerofoil module. Reprinted from [124].

Figure 3.4 illustrates the various modules that make up an aerofoil. The forward part of an aerofoil is rounded and is called the leading edge. It is the part of the aerofoil that meets the wind first. The aft part, which is called the trailing edge, is narrow and tapered. It is the last part before the wind leaves the aerofoil. A reference line often used in discussing aerofoils is the chord, an imaginary straight line joining the terminals of the leading and trailing edges, dividing the aerofoil into the upper chamber and the lower chamber. The angle between the chord and the oncoming wind towards the aerofoil is labelled as the angle of attack. Lift force on the aerofoil would vary when the angle of attack changes [124].

Aerofoil geometry can be characterized by the coordinates of the upper and lower surface. It is

often summarized by a few parameters including maximum thickness, maximum camber, position of max thickness, position of max camber, and nose radius. By given these parameters, a reasonable aerofoil section can be demonstrated accurately. The NACA aerofoils are aerofoil shapes for aircraft wings developed by the National Advisory Committee for Aeronautics (NACA) [125]. The shape of the NACA aerofoil is described using a series of digits following, illustrating three parameters, the camber (first digit), the position of the camber (second digit) and the thickness in percent (two digits). In this work, the most commonly used aerofoil shapes NACA 0024 and NACA 4424 are selected and will be tested in chapter 4. The former one is symmetric aerofoils (not cambered) while the latter one is an asymmetric aerofoil profile. According to the operation description, an asymmetric aerofoil should be preferable to maximise the lift force acting on it. For simplification, only two aerofoil shape are tested in this work. However, other aerofoil shapes might give better results.

3.7 Conclusion

In this chapter, the theory governing the mechanical behaviour of the harvester was expounded with different models. Some conclusions were drawn from those models for potential design feature. The minimum wind speed for operation of the system is a critical design parameter for tailoring the energy harvester to its target application and maximizing its useful operating range. Based on the working principle of the harvester, the mechanical structure can be optimised by designing the bluff body and aerofoil in a proper way. In any practical device, the amplitude of the mass is limited to some maximum value, together with the magnitude and frequency of the excitation. To get maximum power output, the maximum displacement of the mass should be as large as possible within the design constrains of dimension. Moreover, a lower fundamental frequency of vibration is also preferable for larger output power. The natural frequency of the cantilever can be decreased by either increasing the active length or the effective end mass. Besides the mechanical structure, transduction system is also critical to the generated power. For electromagnetic transducer, high coupling factors can be achieved by designing coils in such way of increasing effective length and decreasing the coil resistance. While in the piezoelectric transduction system, although a lower frequency and a larger amplitude will help increase the output, as piezeceramics are fragile, the maximum displacement must be controlled to produce strain within the limit of the material. Furthermore, static aeroelasticity of such device should be considerable for steady operation. All these design concerns will be discussed in detail and investigated computationally and experimentally in following chapters.

Chapter 4 Oscillation Wind Harvester Design

In this chapter, a wind harvester model is designed and discussed. The main objective is to design the structure based on theory and estimate the performance by simulation. The simulation of the model will be carried out through a finite element method using ANSYS software, and it will be used to compare with experimental results. To optimise the basic geometry of the harvester, both simulations and experiments in this chapter focus on the mechanical design of the harvester without the transducer part. The transducers will be studied afterwards.

4.1 Design Considerations

As mentioned in previous chapters, in order to operate throughout the entire range of flow speeds in air ducts, a low threshold wind speed (<1.5 m/s) is desirable for the harvester. This parameter is an important design point for any potential application and would be constrained by size, mass, and material limitations in practical applications. It can be achieved by improving the mechanical and transducer configurations. The mechanical configuration involves several parameters such as the position of the bluff body, the attack angle of the cantilever wing, and the dimensions of the cantilever (seen in Figure 4.1). These need to be optimized simultaneously according to the operating conditions at different wind speed. The optimum configuration thus should be designed by investigating these factors for a better performance.

To achieve the maximum output power from the device, the input excitation from the air flow should ideally match the natural frequency of the cantilever. For low wind speed operations, the oscillation frequency of the harvester is normally lower than 20 Hz. In order to operate at resonance, the natural frequency of the structure should reduce to that value as well. This target can be achieved through changing dimensions of the beam and employing large proof-mass or low material stiffness.

After considering the mechanical design factors of the harvester, the transducer features will

then be taken into account to enable electrical energy output. For most flow-induced energy harvesters, piezoelectric generators and electromagnetic transduction are used as major transduction mechanisms. These design details will be discussed in the following chapters.

4.2 Structure Design

4.2.1. Overall Size

The micro wind harvester presented in this report is based on a previous larger scale device reviewed in the literature search. The volume of the previous harvester was 624 cm^3 in total. In order to scale down the size and investigate the performance, a miniaturized form with a volume of 62 cm^3 approximately, which is one tenth of the large device volume, was proposed. The total volumes and the beam sizes of two harvesters are listed below individually. A T-shape extension of the beam was used to support the length of the blade. This kind of shape is preferable rather than a traditional simple rectangular shim sheet as the differing air flows along the length of the blade might lead to a periodic and random twist during oscillation.

Table 4.1: Main components of two harvesters.

Main Components	Reference device	Miniature prototype
Total volume	120mm ×80mm×65mm	50mm ×35mm×35mm
Beam	50mm ×18mm×0.2mm	35mm ×5mm×0.1mm

4.2.2. Material Chosen

For most flow-induced energy harvesters with a cantilevered structure, two materials, beryllium copper and stainless steel, are widely used as great spring materials. Properties of those two alloy materials are slightly different. In this section, beryllium copper was selected to fabricate the beam because of its lower stiffness which means a lower nature frequency. Balsa wood was used to make the wing part to minimize weight since the density of this material is much lower than plastic or other kind of wood. Other components were fabricated using 3D rapid prototyping. All material properties are listed in the following table.

Table 4.2: Material Properties.

Components	material	Density (g/cm^3)	Poisson ratio	Young's modulus (G Pa)
Beam	Beryllium copper	8.9	0.32	120

Wing	Balsa wood	0.35	0.4	11

4.2.3. Design Configuration

The harvester is constituted with four components, including a beam, a wing, a base part and a wind shield (bluff body). Figure 4.1 shows the sketch of the harvester mechanical structure. Some factors that may have a significant influence on the performance of the harvester are the position of the bluff body, shape and the attack angle of the wing. The position of the bluff body can be represented as the distances between the bluff body and the wing both in horizontal and vertical directions. The horizontal position of the bluff body is the distance from the wing, while the vertical position is the height from the wing. A set of simulations and experiments will be carried out to investigate the influence of these factors.

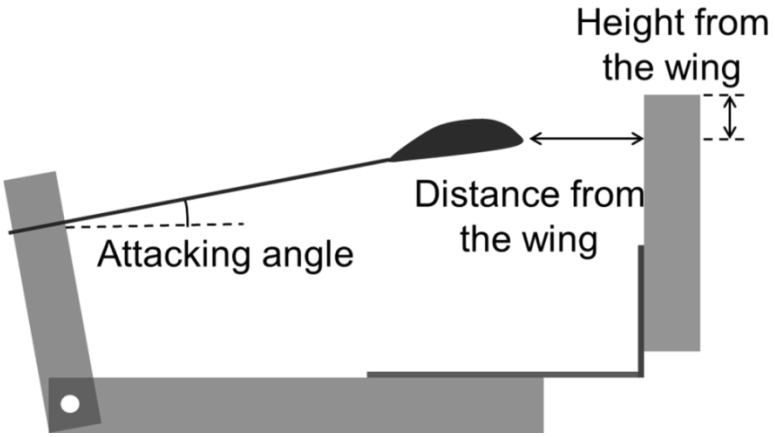

Figure 4.1: Schematic of the harvester mechanical structure.

4.3 Simulation Analysis

It is necessary to investigate the influence of the mechanical structure both computationally and experimentally. Ideally fluid-structure interaction simulations should be conducted to simulate the behaviour of the device. However fluid–structure interaction problems and multi physics problems are often too complex to solve analytically and numerically. In this work, for simplification, a static model was used for analysis instead of computational dynamic model. All simulations were conducted using ANSYS CFX to estimate the effect of bluff body and the attack angle of the wing. Results from different arrangements were compared and plotted using ANSYS commercial package of Design Optimization.

Figure 4.2 shows the symmetry scheme of the static model where a laminar airflow passed through the wind tunnel along –x direction with the bluff body placed at the bottom. The inlet

speed was set from 1 m/s to 8 m/s, which is the wind speed range in the experiments. The colours in the figure represent the velocity distribution and the arrows represent the wind speed vector. During the simulation, when the airflow passes the aerofoil, a lift force is generated due to the asymmetric wind speeds above and below it. In static model, the aerofoil and cantilever will not move with the airflow, therefore the threshold wind speed is unpredictable. However, as explained in Chapter 3, the oscillating vibration of the device starts from the asymmetric force above and below the aerofoil, which is enhanced by placing a bluff body in front of the aerofoil. Since the consequence that large lift force acting on aerofoil will provide a relatively low threshold wind speed, configurations generating larger lift force should correspond with those having lower threshold wind speed. Accordingly, a set of parameters were used to estimate the lift force applied on the aerofoil, which was used as a guide to determine the threshold wind speed of the device. The variable simulation parameters included the height of the bluff body, the horizontal distance from the aerofoil and the attack angle of the aerofoil.

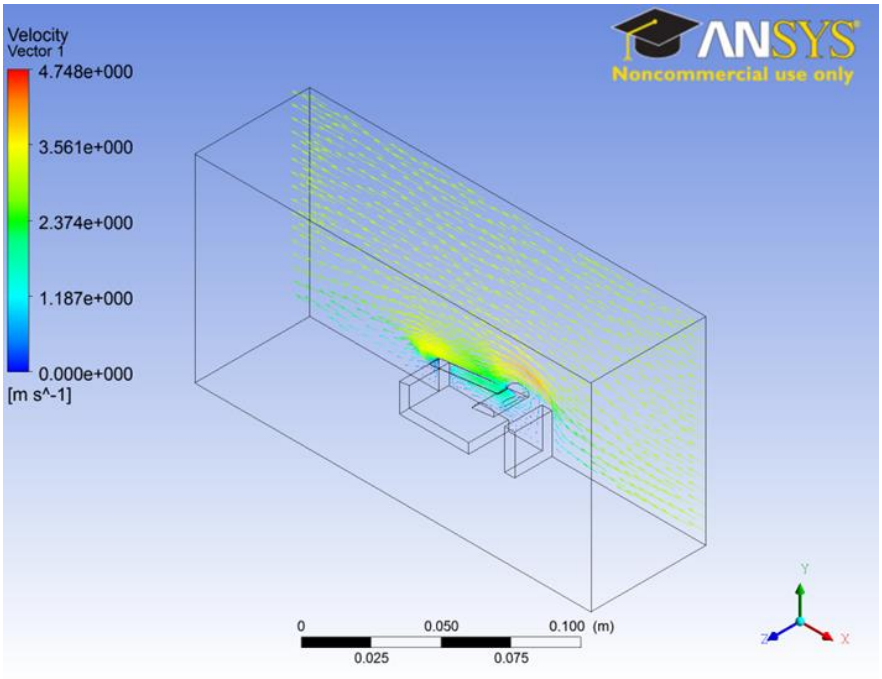

Figure 4.2: Static modal in ANSYS CFX (Inlet wind speed = 2 m/s).

Firstly, the characteristic of flow over the bluff body without the device was investigated. As shown in Figure 4.3. It is clear to see the airflow over the bluff body has changed both in magnitude and direction. In area A, the flow speed has magnitude nearly half as much again as the inlet speed while flow speed at area B reduces significantly. This situation causes an asymmetry in pressure distribution, resulting in a different pressure field behind it.

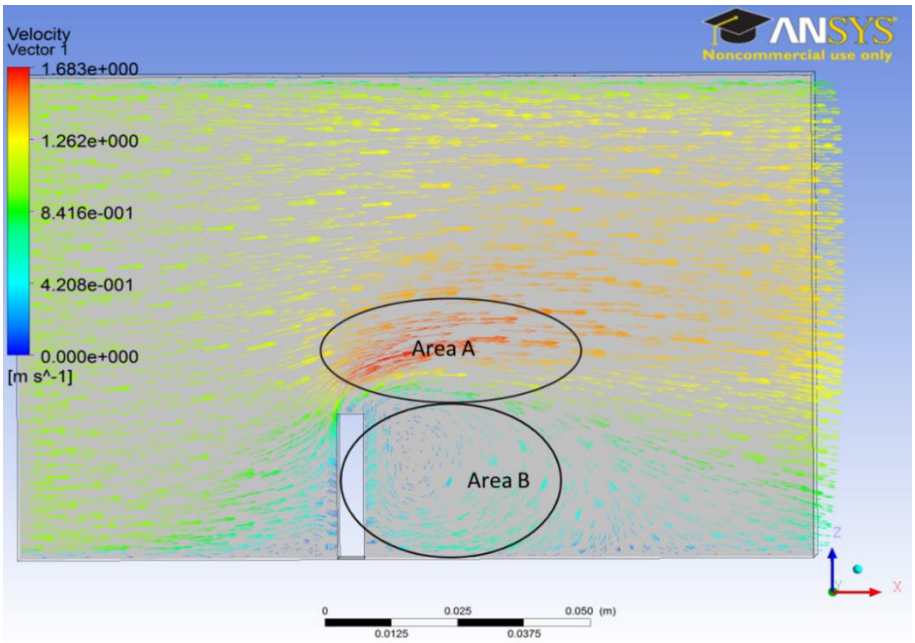

Figure 4.3: Flow speed distributions around the bluff body (Inlet wind speed = 1 m/s).

Secondly, simulations were run by placing the bluff body in front of the flapping part at different positions with the same attack angle and airflow speed. At different positions, velocity distributions above and under the surface of the aerofoil are different, leading to different lift forces acting on the aerofoil and beam, as shown in Figure 4.4. For this reason, the position of the bluff body, in other words, the height and distance between the bluff body and the aerofoil are important factors that should be studied further.

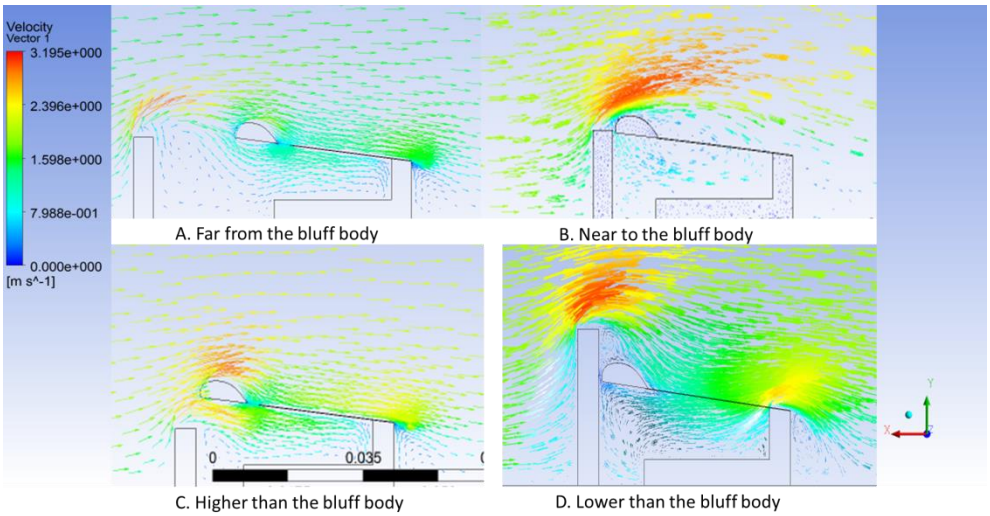

Figure 4.4: Flow speed distributions around aerofoil at different positions (Inlet wind speed = 2 m/s)

To investigate these parameters, two schemes were defined to estimate the lift force applied on

the aerofoil. The first one is at a fixed attack angle, firstly changing the height of the bluff body while maintaining a fixed distance from the aerofoil. The other scheme was to vary the distance between them with a certain height of the bluff body. These adjustments were done with ANSYS Design Optimization. Results of the simulation are presented in the form of lift force applied on the aerofoil as seen in Figure 4.5.

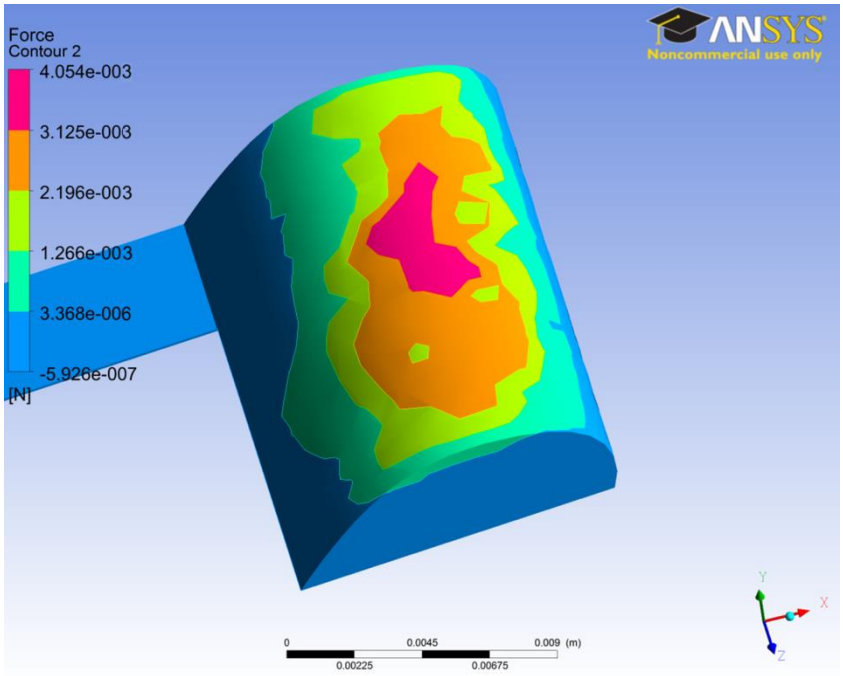

Figure 4.5: Lift force distributions on the aerofoil and cantilever (Inlet wind speed = 1 m/s).

A 3D response surface of the lift force at an attack angle of 5º with different heights and distances from the bluff body is plotted in Figure 4.6. The colours in the figure represent the force distribution where red corresponds to higher force level. From the response surface, distribution of the maximum values of force concentrates at distances from 3 mm to 10 mm and heights from 18mm to 21mm.

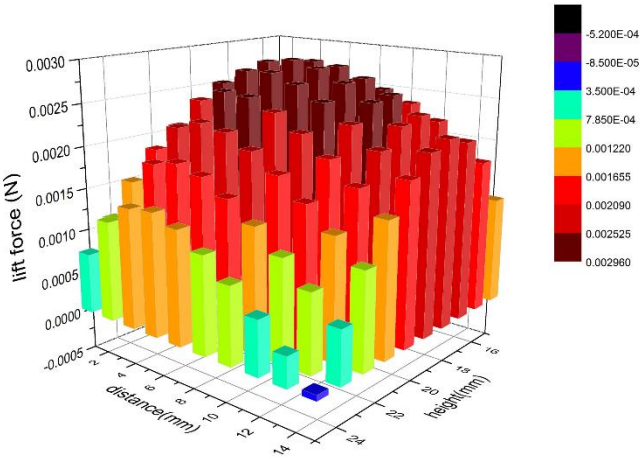

Figure 4.6: 3D bar chart of the lift force with different heights and distances from bluff body (Attack angle = 5º).

The attack angle of the aerofoil also has an influence on performance. The investigation of attack angle was carried out by setting it as the input parameter ranging from 0º to 30º with a step of 1º while the height and distance of the bluff body was fixed at 18 mm and 5 mm respectively. The Lift force on the aerofoil at different attack angles are plotted in Figure 4.7. It can be seen that with the same height and distance, the lift forces at attack angles smaller than 8º are relatively higher than the other values. However, when attack angle is larger than 15º, the lift force decreased significantly with the increase of angle.

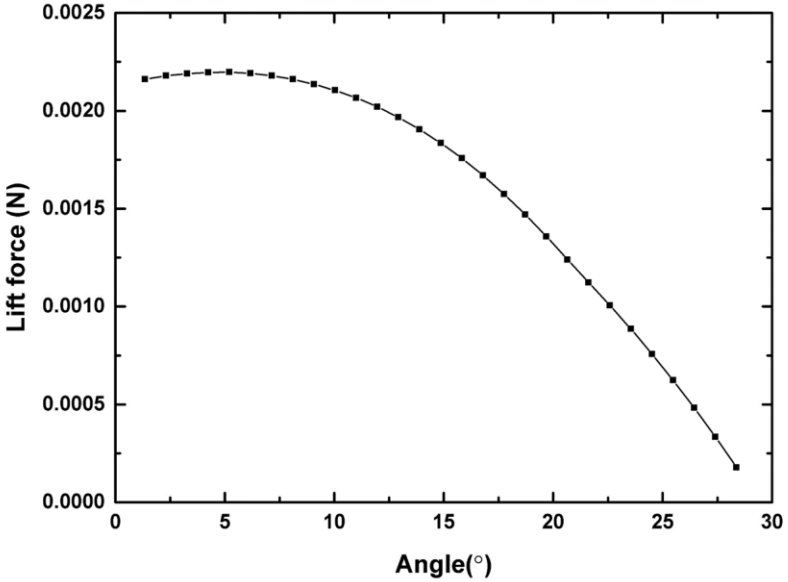

Figure 4.7: Lift force at different attack angles with the fixed height and distance.

Finally, the optimum configurations are summarized by combining the best values from above results, shown below in Table 4.3.

Table 4.3: Design values for parameters optimization.

Designing Point	Height of bluff body	Distance between bluff body and aerofoil	Attack angle of aerofoil
1	21 mm	3 – 4 mm	1º-8º
2	20 mm	5 – 7 mm	
3	19 mm	8 – 9 mm	
4	18 mm	11 mm	

4.4 Testing of the Wind Harvester

4.4.1. Experimental Setup

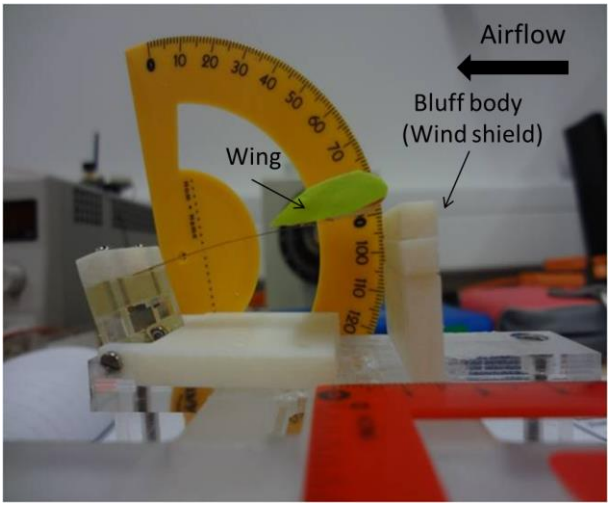

Figure 4.8: Prototype of the harvester in this work.

To verify the simulation model, a prototype of the harvester only consisting of mechanical parts (i.e. no transducer), as illustrated in Figure 4.8, was fabricated and tested in the air duct. All the tests were done in the centre of a wind tunnel as shown in Figure 4.9(a). The air flow was generated by a centrifugal fan which was then conducted along a steel air duct of approximately 2 m in length. The harvester was placed in the final 40 cm of the duct which is a transparent plastic section and enables the oscillation of the harvester to be observed during the test. The cross section of the duct was 20 cm × 35 cm. Small holes were drilled in the 20 cm long steel

section in front of the harvester to enable the insertion of an anemometer probe to measure the flow speed. The anemometer has a 2% precision error. The airspeed can be adjusted by controlling the fan speed, which allows tests from 0 to 8 m/s. A flow speed profile was measured at different positions in the air duct through these holes and plotted in Figure 4.9(b). Since the onset speed and prevalent of air turbulence changes slightly at different positions in the wind tunnel, the harvester was placed near to the end of the duct in the centre where the air flow is most steady and can easily be observed. All tests were done at room temperature. During the tests, the threshold wind speed was measured by the aerometer; meanwhile amplitude of the oscillation was measured using a protractor fixed on one side of the harvester. Testing here should be precise and accurate and required a long time because of some periodic instability. Short videos were also taken to find average values of the amplitude.

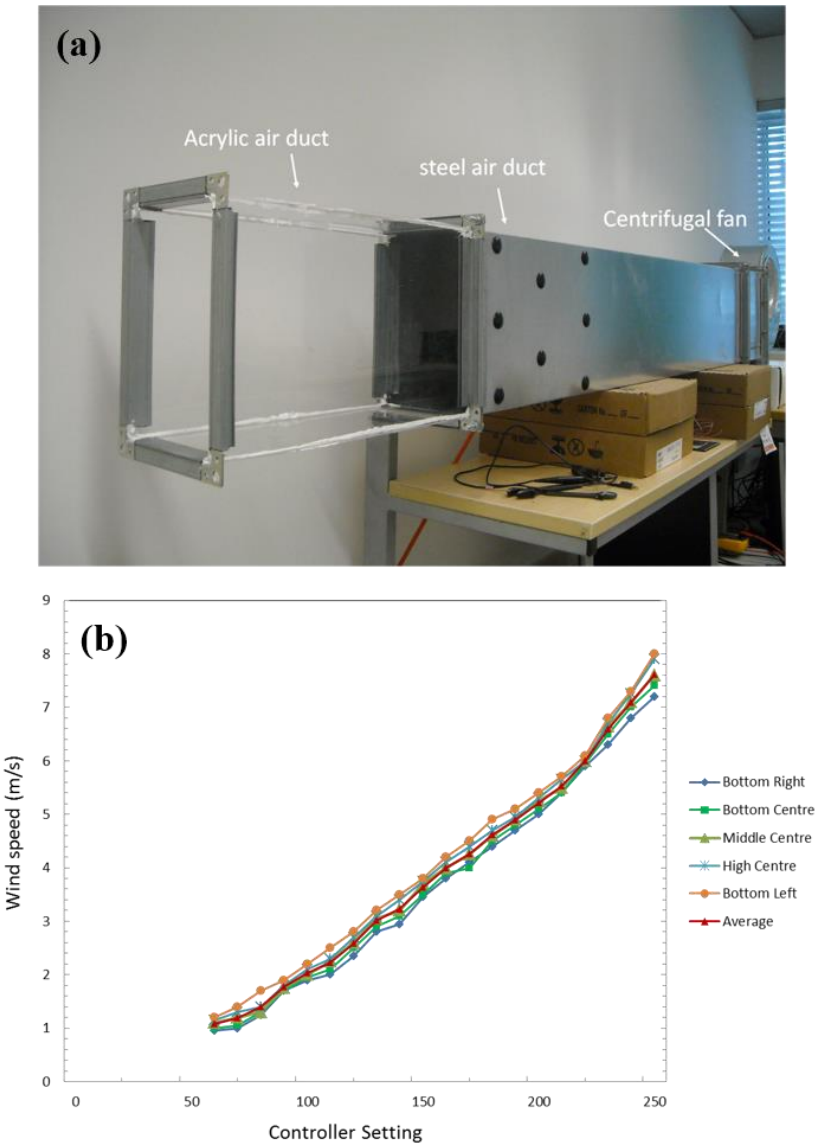

Figure 4.9: (a) Wind tunnel used in this work; (b) The flow speed profile in the wind tunnel.

The generator was also tested on a shaker table operated in sinusoidal vibration over a range of different frequencies close to the resonant frequency of the cantilever beam. The acceleration level was maintained at a constant level by using a feedback system as shown in Figure 4.10. The accelerometer in the shaker measures the actual value of frequency and acceleration level and is feedback into the control processor. A processed signal is then generated and amplified to drive the shaker to produce the desired acceleration level at a given frequency. The displacement was measured using a KEYENCE laser displacement meter LC-2450 and subsequently converted to a digital signal and is measured with a National Instrument Sequence Test Programme.

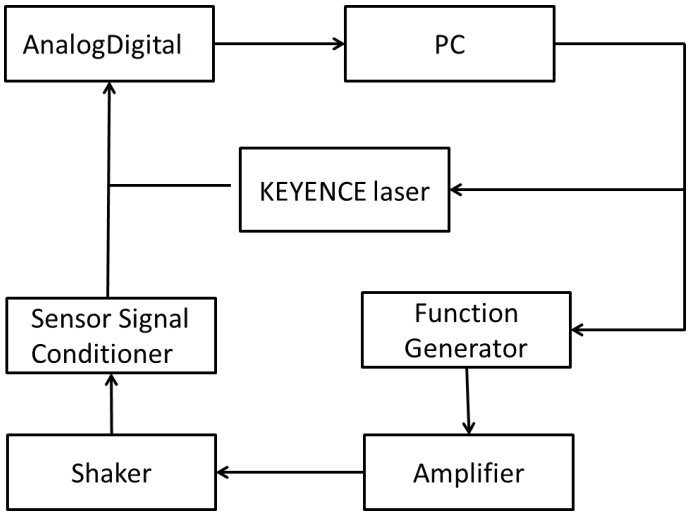

Figure 4.10: Diagram of a sequence test system.

4.4.2. Experimental Results

Experimental results were used to estimate the performance of the harvester focusing on two aspects; the threshold wind speed and the tip displacement. The threshold wind speed here is defined as the lowest airflow speed at which the steady peak-to-peak displacement of the wing exceeds 1 cm as displacement smaller than this value is not easy to be observed.

4.4.2.1 Attack Angle

The attack angle is of significant importance in this structure. The investigation of the influence was carried out by determining the threshold wind speeds at variable attack angles with different combinations of distances and heights of the bluff body. The attack angles were tested ranged from 0^o to 30^o with a step of 1^o. For different bluff body height and distance combinations, the threshold wind speed at different attack angles changes roughly towards the same trend. Figure 4.11 illustrates this trend where the distance and the height between the

bluff body and the wing are 5 mm and 20 mm respectively. It can be seen that with the same height and distance, the threshold wind speeds are the lowest (below 1 m/s) for attack angles from 5º to 8º. In addition, when the attack angle is larger than 15º the threshold wind speed increases rapidly. More figures can be found in Appendix A.

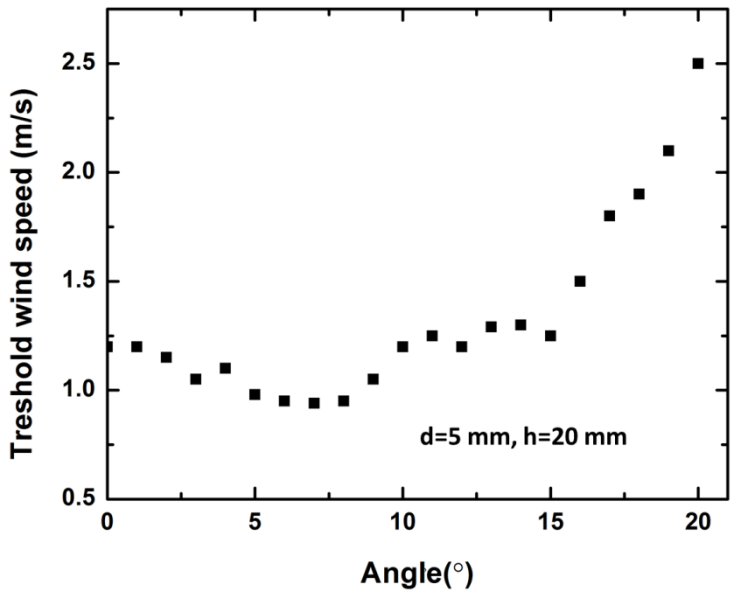

Figure 4.11: Threshold wind speed at different attack angle the same height and distance (d = 5 mm, h = 20 mm).

4.4.2.2 Distance of the Bluff Body

The position of the bluff body is another key factor which has influence on the performance of the harvester. Tests were carried out both on horizontal and vertical distances (height) between the aerofoil and bluff body. During the tests, horizontal distance was changed from 1 mm to 15 mm by a step of 2 mm while the vertical distances changing from 15 mm to 25mm. In this section, a parameter of Δh is introduced and it refers to the gap between the bluff body and the wing. For instance, 5 mm means the bluff body (which is 25 mm high in total) is 5 mm higher than the leading edge of the wing, likewise –5 mm means the bluff body (which is 15 mm high in total) is 5 mm lower than the wing.

Experiments showe that a value of height larger than 1 mm always leads to a high threshold wind speed. The values of the threshold wind speed at varying distances and heights are shown in Figure 4.12. Lower threshold wind speeds are found at horizontal distances ranging from 3 mm to 11 mm with vertical distances varying from 0 mm to –4 mm. Two relations are observed between the distance and the threshold wind speed with different height conditions as shown

in Figure 4.13. When the bluff body is lower than the leading edge of the wing, the threshold wind speed reduces with the increasing distance in a certain range before rising again. On the other hand, when the bluff body is higher than or at the same height of the wing, increasing distance results in higher threshold wind speed for operation. It has also been found that to achieve the lowest threshold wind speed, lower heights are favourable for further distances. More figures can be found in Appendix B.

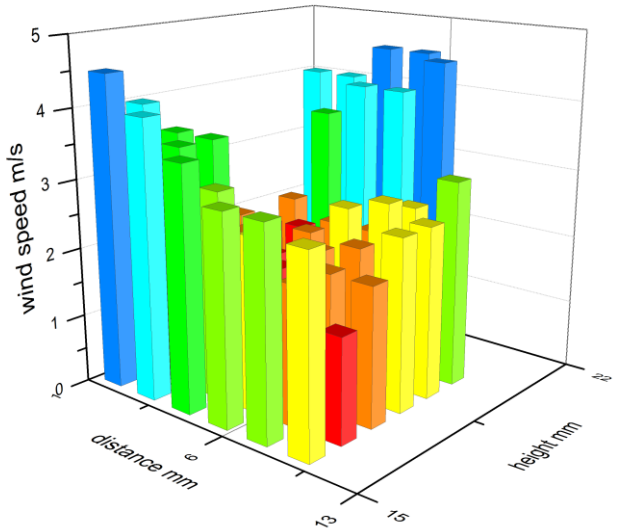

Figure 4.12: A 3D bar chart for threshold wind speed with variable distances and heights of bluff body (attack angle = 5º).

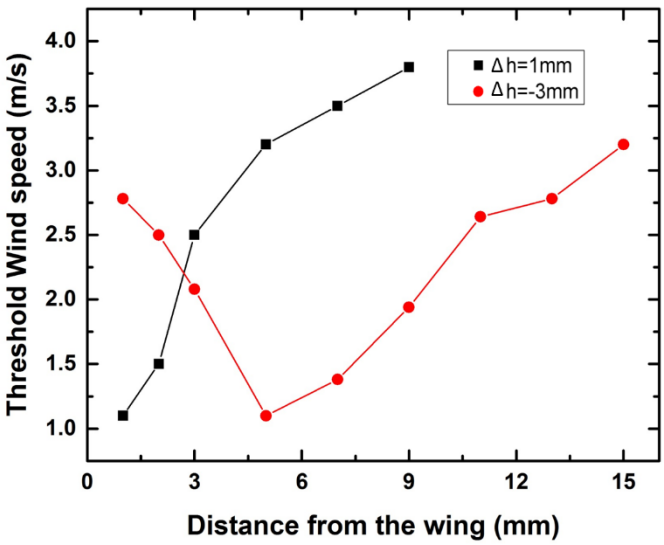

Figure 4.13: Threshold wind speed with variable distances with the bluff body 3 mm lower and 1 mm higher than the wing (attack angle = 5º and lines plotted are used to indicate the trend).

Figure 4.14 illustrates this relationship between the height and the distance at a fixed attack angle. After optimising the distance of the bluff body and the attack angle, the lowest threshold of the device is lower than 1 m/s.

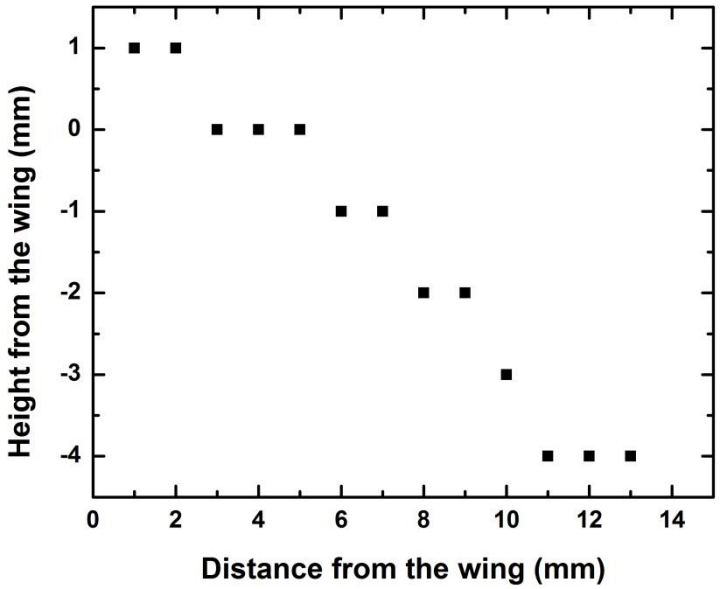

Figure 4.14: Relationship between the height and the distance (attack angle = 5º).

4.4.2.3 Shape of the Wing

Two main factors may have influence on the performance of the wing are the length and the width. Experiments were carried out using a model wing with the shape of flat plate, so that the variations could be easily adjusted. During the experiments, the attack angle was set to 5º and the distance and height of the bluff body were set to 5 mm and 20 mm respectively. Figure 4.15(a) and (b) illustrate the threshold wind speed of the wings at different length and width respectively. Results show a plate of around 30 mm long and 11 mm wide are the most optimising size, which can further decrease the threshold speed to 0.9 m/s. Wings longer than that length resulte in an increase in twist. More figures can be found in Appendix C.

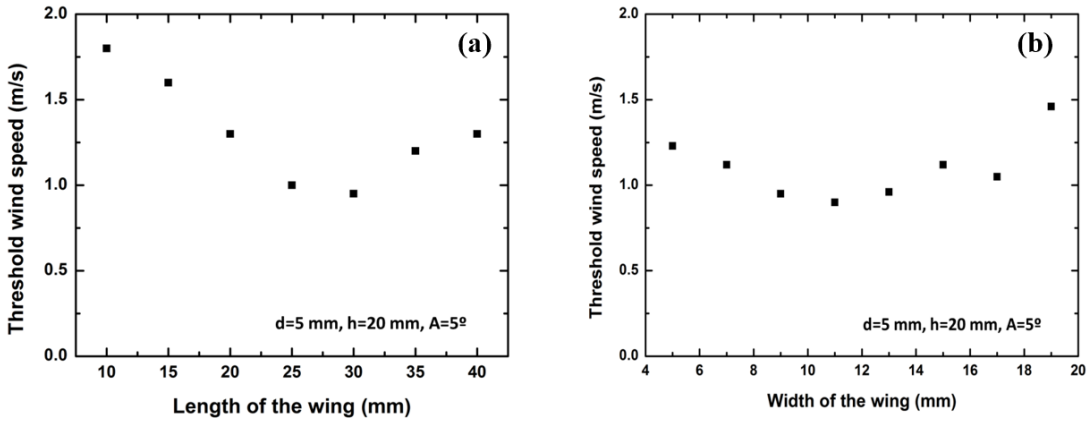

Figure 4.15: (a) Threshold wind speed with different lengths of the wing; (b) Threshold wind speed with different widths of the wing.

Three different wing profiles were tested to investigate the effects of the aerodynamic characteristics of the wing on the harvester performance. These geometries selected were flat plate; NACA 0024 aerofoil and. NACA 4424 aerofoil. The flat plate represents the simplest and cheapest possible design while the NACA profiles are selected for different thickness and cambers of the aerofoils. In order to compare the aerodynamic characteristics of the profiles only, those wings were build and weighted to closely matching mass and size. And tests were carried out for different wings at the same construction of the harvester. Table 4.4 shows the geometry parameters and the threshold wind speed for operation of the wings.

Table 4.4: Comparison of four Wings Parameters.

Wing type	**Wing mass**	**Wing length**	**Wing width**	**Wing maximum thickness**	**Threshold wind speed**
Flat Plate	0.16 g	30 mm	11 mm	3 mm	0.9m/s
NACA 0024 aerofoil	0.21 g	30 mm	11 mm	3 mm	0.85 m/s
NACA 4424 aerofoil	0.25 g	30 mm	11 mm	5 mm	0.8 m/s

From the results it can be seen that the NACA 4424 aerofoil showed better performance with a lower threshold wind speed (0.8 m/s) notably than the others. The reason is the asymmetric aerofoil shape is more preferable to maximise the lift force acting on it. Consequently, it was used for the harvester for further investigation.

4.4.2.4 Attached Mass

Considering that adding proof mass could alter the amplitude of the oscillation and increase the power output, investigation was taken in the influence of adding mass. Tests were carried out by measuring the threshold wind speed and the amplitude of the wing with variable weights of mass at different attack angles. The weight of the attached mass was ranging from 0.1 g to 2 g with a step of 0.2 g. All the masses were placed under the wing in the centre of the cantilever tip. During the experiments, the distance and height of the bluff body were set to 5 mm and 20 mm respectively. The origin attack angle was set to 5º and increased with the increase values of added mass. The threshold wind speed and amplitude at 2 m/s with a variety of proof mass are plotted in Figure 4.16 respectively. It is found adding weights of the proof mass can magnify the amplitude; however it increases the threshold speed as well. In order to control the threshold wind speed below 1.5 m/s, the maximum proof mass should be lower than 2 g.

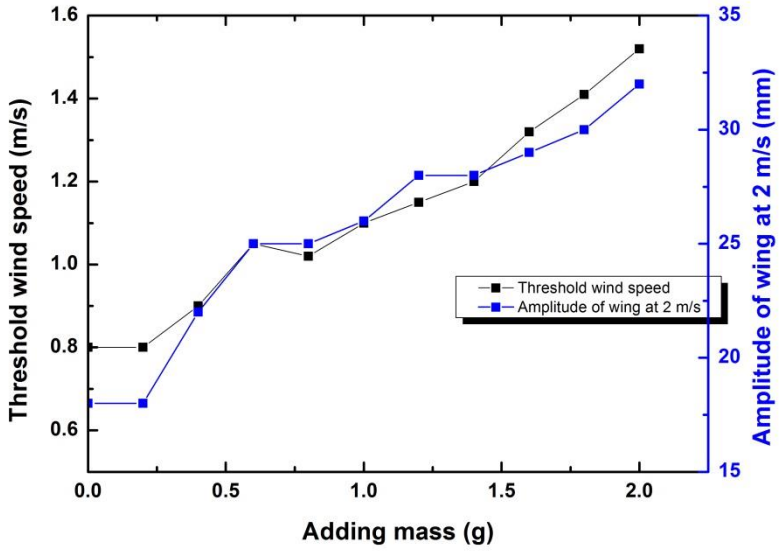

Figure 4.16: Threshold wind speed and amplitude with variable weights of masses (plotted line was used to indicate the trend).

The device was tested on the shaker operated as Figure 4.10 to estimate the natural frequency of the cantilever beam with four different proof masses attached under the wing in the centre of the cantilever tip. Figure 4.17 shows a typical frequency response for the cantilever. The cantilever without proof mass has a resonant frequency of around 12.8 Hz, and this value decrease with increasing proof mass attached on the cantilever. With proof mass of 2 g, the resonant frequency can be reduced to 7.1 Hz.

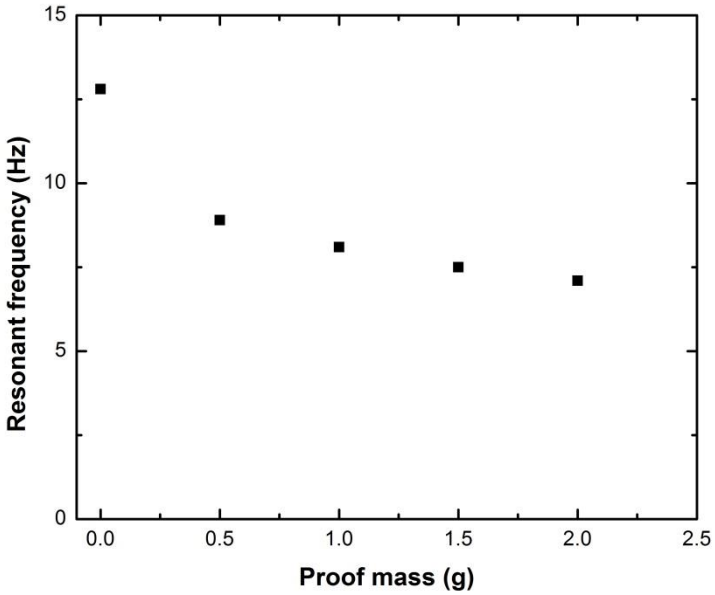

Figure 4.17: Experimental results for resonant frequency with different proof mass.

4.4.2.5 Final Results

After testing the influence of all factors mentioned above, a list of optimum configurations of the harvester is shown in Table 4.5.

Table 4.5: Optimum structure of the harvester in this work.

Angle of blade	**Distance from the blade（mm）**	**Height from the blade（mm）**	**Mass（g）**	**Threshold wind speed (m/s)**	**Amplitude at 2 m/s (mm)**	**Natural frequency（Hz）**
5°	3	0	/	0.8	18	12.8
6°	5	0	/	0.8	22	12.8
7°	7	-1	/	0.8	18	12.8
8°	11	-4	/	0.8	20	12.8
7°	3	0	0.5	1	25	8.9
9°	5	0	1	1.1	26	8.1
10°	7	-1	1.5	1.3	28	7.5
12°	11	-4	2	1.5	32	7.1

To summarize, the configuration of the harvester has great influence on the performance. Experiments showed that the threshold wind speeds are lowest at attack angles between 6º to 10º. Lower bluff body heights should be combined with increased distances for the lowest threshold wind speed. It has also been demonstrated that adding mass can increase the amplitude and reduce the natural frequency significantly. However it also increases the threshold wind speed. As it has been restricted to 1.5 m/s, the maximum value of the proof mass added is 2 g.

4.5 Comparison

4.5.1. Optimum Mechanical Structure

Structure simulations by ANSYS CFX were used to investigate the influence on threshold wind speed of the harvester with different configurations. Results of the simulation are presented by using the lift force as a guide to determine threshold the wind speed of the device. It is assumed that the lift force acting on aerofoil will provide an indirect indication of the threshold wind speed, optimum configurations in simulation should demonstrated maximum lift force. A set of diagrams comparing the simulation results and the experimental results is shown in Figure 4.18. Both simulation and test results verify that optimum positions of the bluff body are approximately between 3 mm to 11 mm in horizontal distance and 18 mm to 20 mm in vertical distance. Relations between the distance and the threshold wind speed at certain height of the bluff body have the same trend in the simulations and tests. For instance, if the bluff body (with height of 17 mm) is 3 mm lower than the wing, lift force increases initially and then begins a gradual decrease when the distance is larger than 8 mm (Figure 4.19(a)). Accordingly, during the tests, a decrease was observed in the threshold wind speed with the increasing distance in a certain range before rising again. On the other hand, if the bluff body (with height of 21 mm) is 1 mm higher than the wing, further distance results in lower lift force level, which in turn leads to higher threshold wind speed as seen in Figure 4.19(b). However, there is a slight rise before the significant drop in lift force, which is not observed during the tests. Regard to the attack angle, largest lift force are generated at attack angle from 1º to 8º, while the lowest threshold wind speeds are found at attack angle between 5º to 8º. This difference is due to the static model in ANSYS simulation, which does not involve the small bending of the cantilever because of the gravity. However, the influences of the attack angle in computational and experimental work are similar. Figure 4.20(a) showes a smooth increase of the lift force around 6º and a significant decrease when the attack angle was larger than 15º in simulation. And the same trend is also found in the experiments as shown in Figure 4.20(b). In the test results, the variation curve is not as clear as that plotted in ANSYS; however, results follow a similar trend.

Table 4.6 shows the comparison of the simulation and the experimental results.

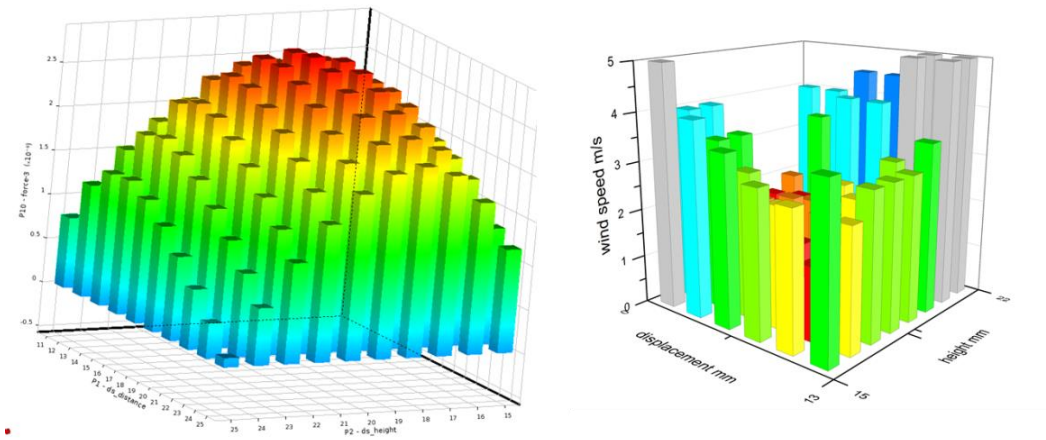

Figure 4.18: (a) Lift force and (b) threshold wind speed as functions of different distances and heights of bluff body from simulation in ANSYS (attack angle = 5˚).

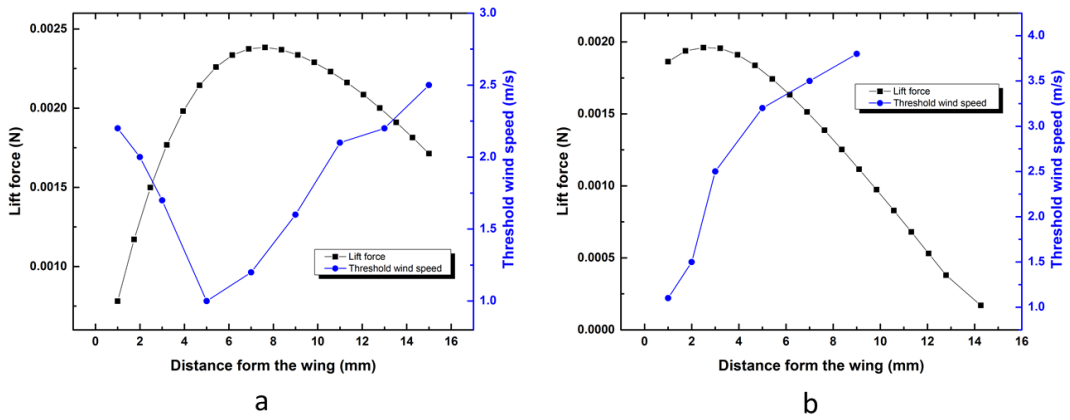

Figure 4.19: (a) Lift force and (b) threshold wind speed a function of different distances and heights of bluff body from simulation in ANSYS (attack angle = 5˚, lines plotted are used to indicate the trend).

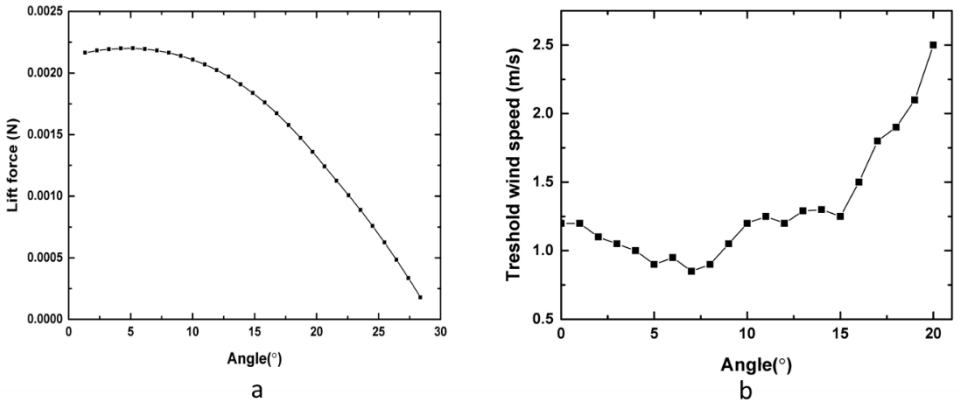

Figure 4.20: (a) Lift force and (b) threshold wind speed a function of different attack angles from simulation in ANSYS (distance = 3 mm, height = 19 mm, lines plotted are used to indicate the trend).

Table 4.6: Comparison of optimal configurations of the harvester in simulation and test results.

	Simulation Analysis	**Wind Tunnel Tests**
Attack angle of aerofoil	1° - 8°	5°-8°
Height of the bluff body	18 mm - 21mm	16 mm - 20 mm
Distance between bluff body and aerofoil	3 mm - 11 mm	3 mm - 11mm

To sum up, although it is not possible to vary and correspond all of the parameters that were computationally examined, the experimental results generally show good correlation with the predicted results, thus validates the simulation model used in this study.

4.5.2. Natural Frequency

As discussed in Chapter 3, known values of elastic modular E and the density of material, the thickness, width, active length of the cantilever, its natural frequency can be predicted theoretically using Equation 3.17. Figure 4.21 shows the comparison of the resonant frequencies of the cantilever in experimental results and theoretical calculation. As can be seen form the figure that the theoretical values are higher than the experimental results in general. For example, without proof mass, the theoretical resonant frequency is 13.3 Hz and the experimental one is 12.8 Hz, which is quite close. However with proof mass of 0.5, the theoretical value is 11.1 Hz, while the experimental result shows a resonant frequency of 8.9 Hz. This is because in the theoretical calculation, the effective mass of end mass distributes evenly along the tip while during the experiments the end mass is in the middle of the cantilever.

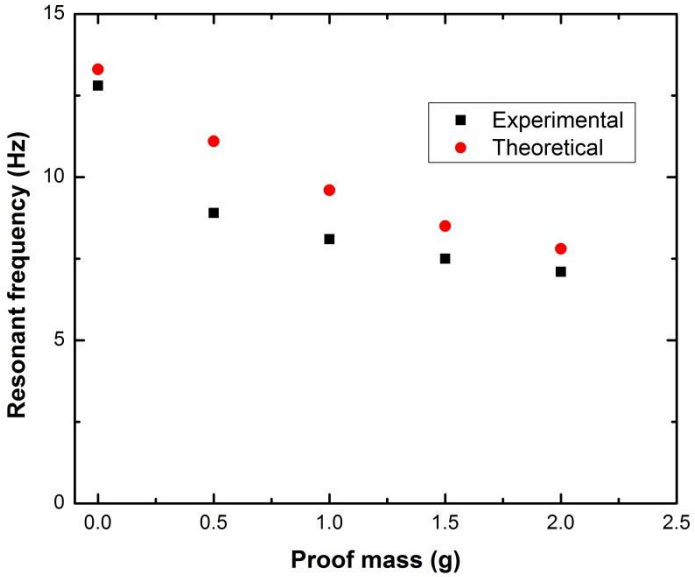

Figure 4.21: Comparison of the experimental results with the theoretical calculation for resonant frequency with different proof mass.

4.6 Conclusion

In this chapter, in order to assess the effect of the bluff body and the attack angle of the aerofoil, computational simulations were conducted using ANSYS. The lift force applied on the aerofoil was used as a guide to determine the threshold wind speed. Results from different configuration arrangements were compared and plotted using ANSYS commercial package of Design Optimization. As seen in the figures, both simulation and test results verified that optimum positions of the bluff body were approximately between 3 mm to 11 mm in horizontal distance and 18mm to 20 mm in vertical distance. The optimum values of attack angle were from 5° – 8°. Moreover, relations between the distance and the threshold wind speed at certain height of the bluff body had the same trend in the simulations and tests. It could be observed that lower heights of the bluff body were favourable for further distances to achieve the lowest threshold wind speed. These similar trends between the simulation and experimental results showed good correlations, which validated the simulation model used in this study. It should be noted that simulation in this section was purely on mechanical structure and the transducer was not taken into account.

Other parameters such as the shape of the wing and the influence of the mass added were also investigated during the tests. The results showed that adding mass with suitable weight can increase the amplitude slightly but increases the threshold wins speed at the same time. In order

to restrict the value of threshold wind speed to 1.5 m/s, the maximum value of the proof mass added is 2 g.

The next chapter will investigate the performance of the harvester with piezoelectric transducer. The design and fabrication of a prototype of the harvester will be presented. After processing, performance of the generator will be tested and evaluated.

Chapter 5 Piezoelectric Wind Generator

For most flow-induced energy harvesters, piezoelectric generators and electromagnetic transduction are used as major transduction mechanisms. Generally piezoelectric generators are favourable for miniature devices when size is the main concern. In this chapter, piezoelectric generator will be used to convert mechanical energy into electrical power. The typical piezoceramic material, PZT, is chosen to fabricate the transducer. The design and fabrication of a prototype of the harvester is presented. After processing, performance of the generator will be tested and evaluated.

5.1 Transducer Design

For piezoelectric transducers in airflow energy harvesting systems, piezoelectric polymers are attractive materials because of their flexibility, but suffer from low charge constant thereby giving low surface energy density. Some researchers developed wind harvesters using piezoelectric ceramics, which are manufactured in bulk form commercially, for its high level of piezoelectric behaviour. However, due to the relatively large thickness, it is not compatible with miniature size devices such as being developed in this work. Therefore a screen printable version has been developed and this has previously been optimised to maximum performance. In addition, as the beam is designed to vibrate at low frequency, the excited amplitude will become large, resulting in a relatively high stress on the beam. As PZT is brittle, the cantilever has to operate within the limit of stress that the material can withstand. Therefore suitable design of the geometry of the PZT layer is important for energy transfer capability.

5.1.1. Design Configuration

For this device, the piezoelectric transducer was designed in form of a cantilevered beam with bimorph structure which consists of PZT attached to both sides of the beam. For each side, a sandwich layer of electrode-PZT-electrode on the dielectric layer was deposited on the beam as shown in Figure 5.1. When the cantilevered beam is purely moving along the *z* axis, the maximum stress induced at the bottom area, close to clapping edge of the cantilever. Therefore in order to optimise electrical energy generation, piezoelectric material should be printed

concentrating on the end of the clamped area of the beam. This structure is commonly used piezoelectric generators, and the actual device will be fabricated based on this model. The limitation of the fabrication technology (in this case, thick-film technology) and the physical constrains of the real device for a robust piezoceramic structure should be considered.

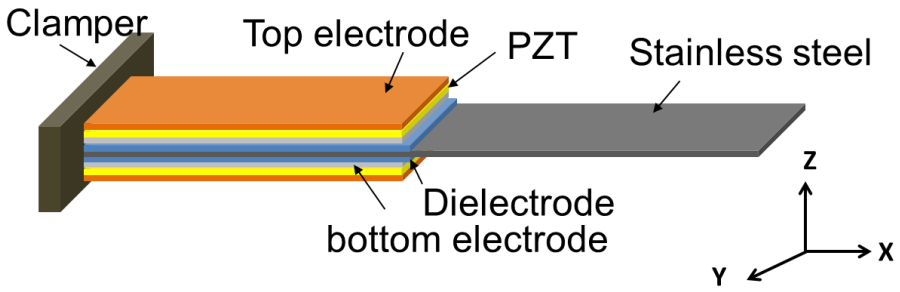

Figure 5.1: Schematic of a cantilevered beam with bimorph structure.

5.1.2. Material Chosen

In this chapter, stainless steel, instead of beryllium copper, was chosen because it is compatible with the firing temperature required by the screen printable piezoelectric and conductive pastes. The type of piezoelectric material selected for a harvester can have a major influence on the functionality and performance. A common type used in energy harvesting applications is lead zirconium titanate (PZT) due to its ability to efficiently transform mechanical energy to electrical energy. The paste should be compatible with the substrate material, (304-type stainless steel in this case). Gold (Au) paste is commonly used to fabricate the bottom electrodes due to its good wire bondability and conductivity. Additionally it does not migrate into the PZT at high temperature. Usually, Pt or Pd are added to form alloys to form a better soldering pad material for thick-film applications. As the gold bottom electrode cannot be printed directly onto the stainless steel substrate, an isolating dielectric layer must be printed. Silver conductor paste is another alternative electrode material with poorer performance but lower cost of fabrication compared with Au. It is used to fabricate the top electrodes due to the low curing temperature, which can minimise lead loss form the PZT. More information of the fabrication materials will be listed in the following section.

5.1.3. Modal Analysis

ANSYS is used to estimate the frequency response and power output produced when the cantilever is driven with base excitation under harmonic vibration in the direction normal to the base. The purpose of this simulation is to investigate the effect of the structure geometry to the resonant frequency and output power with a focus on the PZT layer. The power generated

from the simulation is useful for designing a feasible piezoelectric transducer. The simulation parameters include the length, width, thickness of each layer and the proof mass, and the constants used in the simulation are the elastic modulus, Poisson ratio and density of the material. Simulation is carried out by varying one parameter at a time while fixing the other parameters to estimate the resonant frequency and output power. For simplification, a bimorph cantilever structure consisting of a sandwiched layer as illustrate in Figure 5.1 is designed with different dimensions to investigate the performance. The aerofoil is not taken into account in this structure (shown in Figure 5.2(a)). Firstly, a cantilever with dimensions in Table 5.1 was used for the analysis. Figure 5.2 (b) showed that a fundamental resonant frequency of 50.7 Hz were generated form the simulation. By connecting a resistance load of 900 kΩ (the value of the optimum load is tested in Section 5.4) between the upper and lower electrodes, an output voltage can be obtained for power calculation.

Table 5.1: Parameters for ANSYS piezoelectric simulation in this work.

	Parameter	**Unit**	**Value**
l_b	Beam length	mm	30
w_b	Beam width	mm	5
t_b	Beam thickness	μm	80
l_p	PZT layer length	mm	10
w_p	PZT layer width	mm	5
t_p	PZT layer thickness	μm	80
l_d	Dielectric layer length	mm	10
w_d	Dielectric layer width	mm	5
t_d	Dielectric layer thickness	μm	20
l_{e1}	Top electrode length	mm	10
w_{e1}	Top electrode width	mm	4
t_{e1}	Top electrode thickness	μm	10
l_{e2}	Bottom electrode length	mm	10
w_{e2}	Bottom electrode width	mm	4
t_{e2}	Bottom electrode thickness	μm	10
ρ_b	Density of stainless steel	kg/m^3	7750
ρ_d	Density of dielectric material [126]	kg/m^3	2230
ρ_{e1}	Density of Ag	kg/m^3	9320
ρ_p	Density of PZT [127]	kg/m^3	5440
ρ_{e2}	Density of Au	kg/m^3	19280
β_b	Stainless steel Poisson ratio	dimensinless	0.26
β_p	PZT Poisson ratio [127]	dimensinless	0.35
β_d	Dielectric material Poisson ratio	dimensinless	0.2
β_{e1}	Ag Poisson ratio	dimensinless	0.38
β_{e2}	Au Poisson ratio	dimensinless	0.42
E_b	Stainless steel Young's Modulus	GPa	180
E_p	PZT Young's Modulus [127]	GPa	60
E_d	Dielectric material Young's Modulus [126]	GPa	64
E_{e1}	Ag Young's Modulus	GPa	110
E_{e2}	Au Young's Modulus	GPa	80

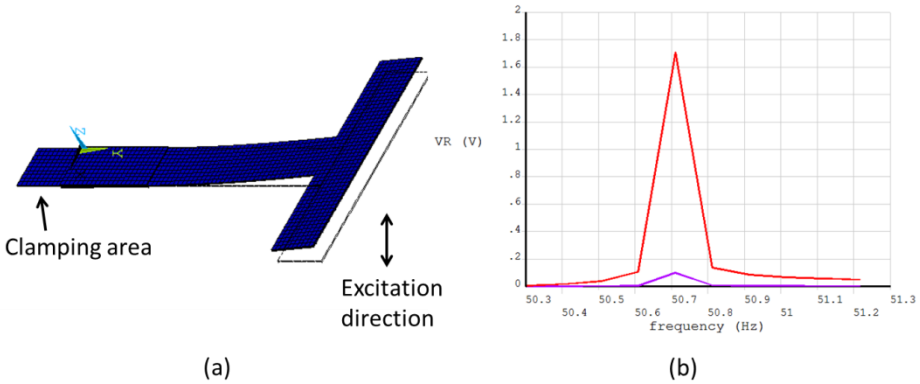

Figure 5.2: (a) Diagram of the cantilever with dimensions in Table 5.1; (b) Diagram of the output voltage generated by the cantilever.

Analytically, it is confirmed that increasing both the width and length of the PZT layer helped increase charge output, and that increasing the width is more effective than the length [128]. As a consequence, printing the PZT layer along the total width and length of the beam can achieve the maximum output charge. However, this will increase the total thickness of the beam, leading to a high resonant frequency which is not suitable for wind generator. Consequently, optimising the size of the PZT layer is necessary for trade-off between the electrical energy output and the resonant frequency. Additionally increasing the PZT thickness also increases the charge output. In this section, the thickness of the PZT layer is fixed at be 80 µm.

Simulations with different lengths and widths of the PZT layers were carried out to investigate resonant frequency and output charge. The width of the PZT layer does not have great influence on resonant frequency; therefore printed width of the PZT material should be the same value as that of substrate, which is 5 mm in this case. On the other hand, the length of the PZT layer affects the performance a lot. As shown in the Figure 5.3, length with values from 11 mm to 16 mm can achieve better output power than the others. However, a larger length significantly increases the resonant frequency at the same time. An important method to reduce resonate frequency and magnify the output power is by adding mass, which could be the aerofoil in this case.

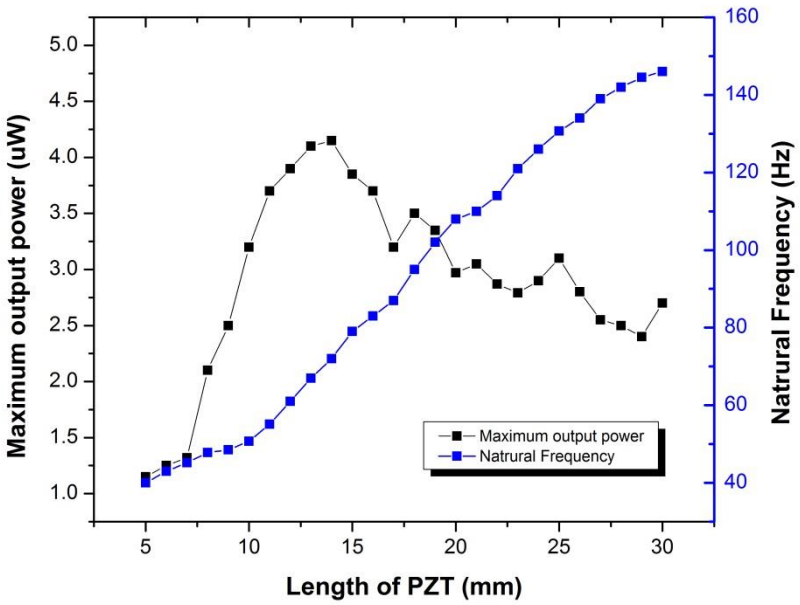

Figure 5.3: Natural frequency and output power with different lengths of the PZT layer (lines plotted are used to indicate the trend).

Simulations were also run with aerofoil attached to the tip of the beam, fully covered the T-shape extension tip of the beam. The simulation parameters are listed in Table 5.2. Results are plotted in Figure 5.4. It can be seen that by attaching wing as the proof mass at the tip of the cantilever, resonant frequency can be reduced significantly and the output power increases as well. For example, with a PZT length of 11 mm, the resonant frequency decreases from 55 Hz to 16.5 Hz while the power output increases from 3.2 µW to 4.5 µW. As a result, PZT lengths from 11 mm to 16 mm are chosen for experiments in the following section.

Table 5.2: Parameters of aerofoil for simulation.

	Parameter	**Unit**	**Value**
l_w	Aerofoil length	mm	30
w_w	Aerofoil width	mm	11
t_w	Aerofoil thickness	mm	5
ρ_w	Density of balsa wood	kg/m^3	350
β_w	Balsa wood Poisson ratio	dimensinless	0.4
E_w	Balsa wood Young's Modulus	GPa	11

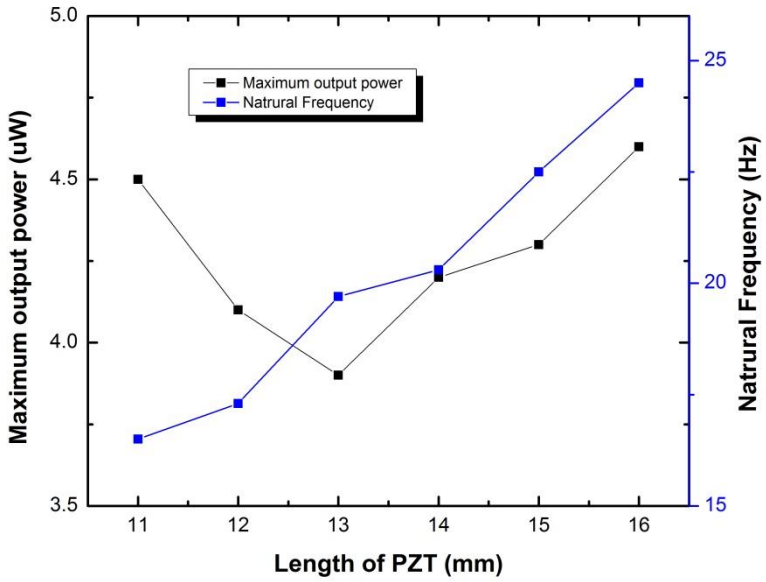

Figure 5.4: Natural frequency with different lengths of the PZT layer after adding the aerofoil.

5.2 Screen Printing Design

5.2.1. Substrate Design

An I-shaped beam was designed as shown in Figure 5.5. The tip extension of the beam is used to support the length of the aerofoil, while the bottom extension is to form the electrode pads for soldering. This kind of shape is preferable rather than a traditional simple rectangular shim sheet as the differing air flows along the length of the blade might lead to a periodic and random twist during oscillation. Layout of the beams on a metal foils (15 cm × 15 cm), was designed with Autodesk Inventor software and illustrated in Figure 5.6. Grooves with small connections are made along the edges of beams and used as mask patterns during the machining process, which will subsequently be etched off to form the beam profiles. The joints can also reduce the warping effect caused by thin metal foil undergoing high temperature firing process.

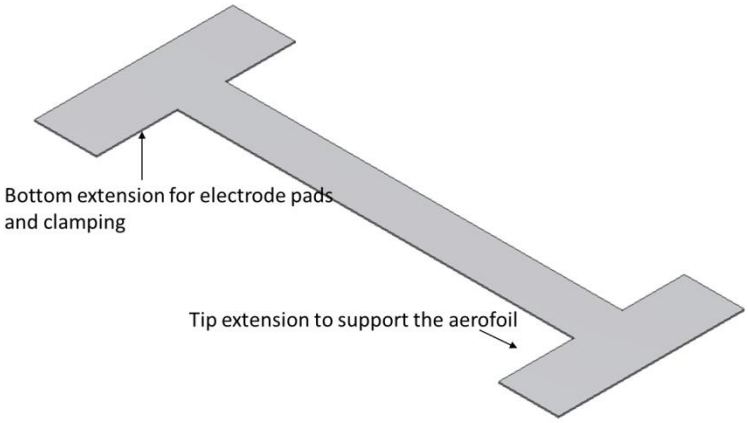

Figure 5.5: Design schematic of the cantilever beam used in this work.

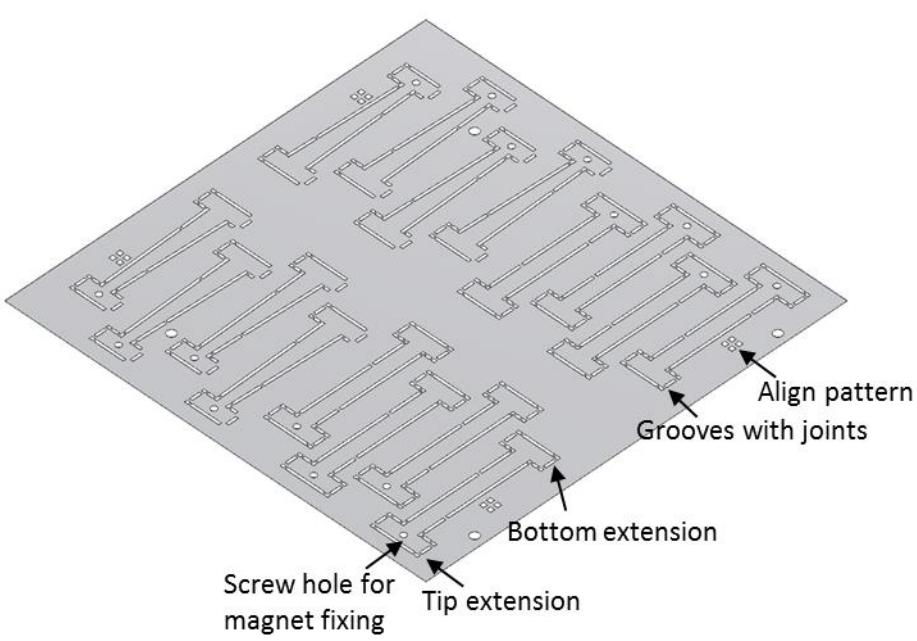

Figure 5.6: Layout of the Cantilever beams on a metal foils in this work.

5.2.2. Screen Design

The structure of a piezoelectric cantilever beam is illustrated in Figure 5.7(a). The PZT layer was designed to be 0.5 mm shorter than the dielectric layer, while the bottom and top electrodes were 0.5 mm narrower peripherally than the piezoelectric material. This is to give a margin for

printing tolerance to prevent a short circuit between those electrodes. Each layer of the composite structure was designed with Autodesk Inventor software and converted separately into photo-plotter format (DXF) which could be translated into a patterned thick-film printing screen. As shown in Figure 5.7(b), four screens were needed to fabricate different layers of the structure.

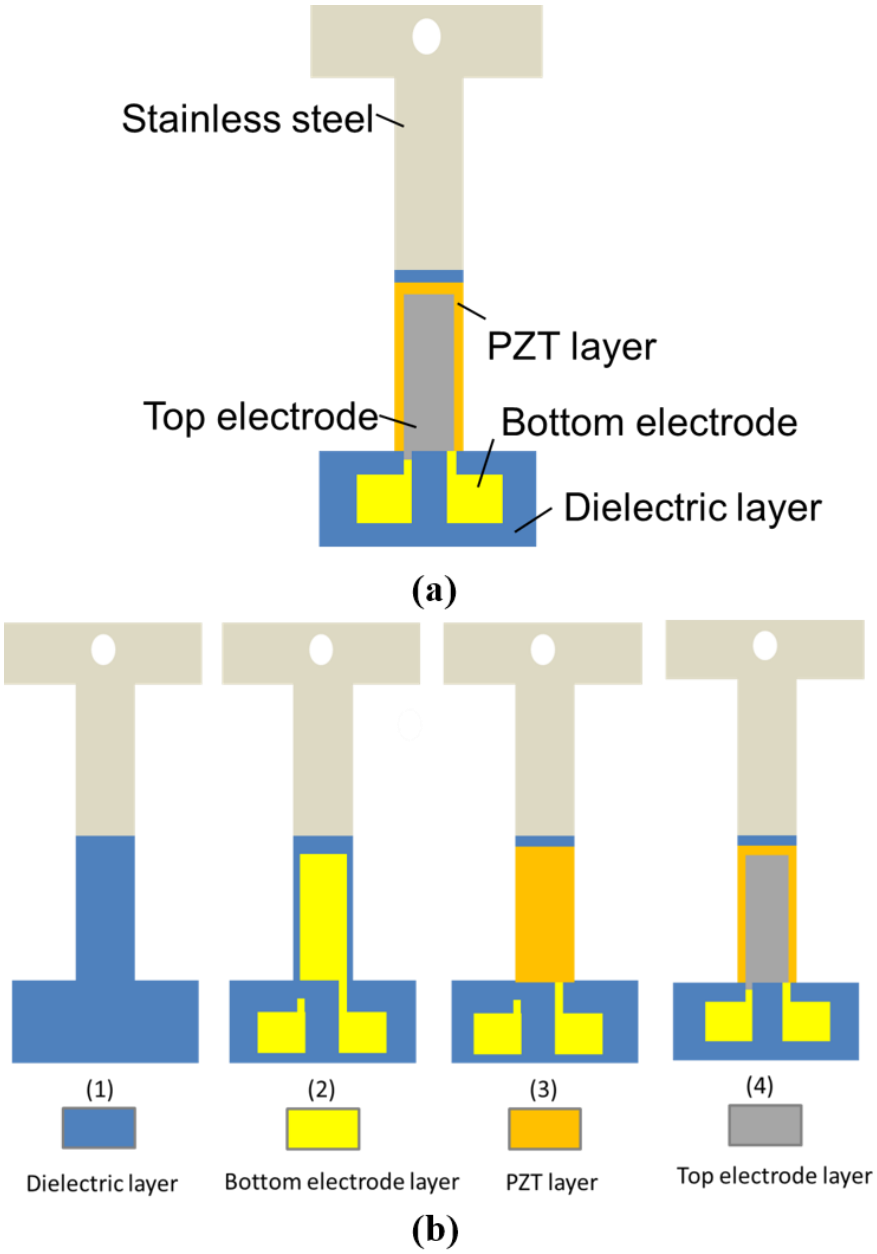

Figure 5.7: (a) Layout of the piezoelectric cantilever structure; (b) 4 layers on the cantilever structure.

Geometry of the piezoelectric cantilever was also investigated in simulation. Moreover, screens were designed for thick-film screen printing process. All the simulation results will finally be

compared with experimental results in the next section.

5.3 Fabrication of the Piezoelectric Cantilever

The piezoelectric cantilever is produced by normal thick-film printing steps, including paste preparation, screen-printing deposition, drying, firing and finally poling process.

5.3.1. Materials Preparation

The ingredients for fabricating the piezoelectric cantilever consist of dielectric pastes, PZT pastes, conductor pastes and the base substrate.

The PZT used in this paste preparation is based on Morgan Electro Ceramics, Southampton, UK, PZT-5H by blending the power of different particle size (ball milled and attritor3 milled). This material exhibits high levels of piezoelectric activity with a low Curie temperature compared to alternative compositions [30]. The particle sizes available had an average diameter of 2 μm and 0.8 μm for the ball and attritor3 milled PZT power respectively. Lead borosilicate glass (CF 7575) is used as the permanent binder. Table 5.3 shows the components of PZT paste formulation, each of which is expressed as a percentage of the total weight of the paste.

Table 5.3: Components of the PZT paste used in this work.

Components	% by Total Weight
PZT-5H(2 μm)	72
PZT-5H (0.8 μm)	18
CF7575	10

The substrate is the essential material on which films or layers of screen printable materials are deposited and processed to build a whole device. Depending on the process of fabrication, a range of substrates can be used for thick-film devices such as alumina, silicon, stainless steel, polymer and glass. Since the device is used for airflow induced cantilever structure, elastic material is more preferable. Consequently stainless steel is selected for the substrate. There are various types of stainless steel according to different alloy compositions. In this study, the type of 302/304 is used because it is compatible with the firing temperature required by the screen printable pastes. The final substrate with a thickness of 80 μm is shown in Figure 5.8, fabricated by Tecan Ltd using photo chemical machining process technology.

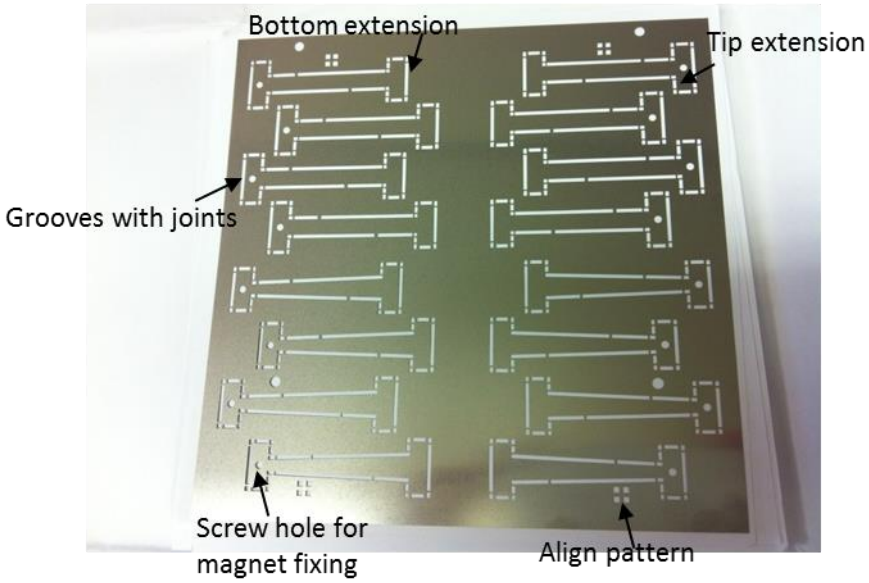

Figure 5.8: Stainless Steel substrate fabricated in this work.

All fabrication materials and their properties are summarized in the following table.

Table 5.4: A summary of f materials deposited in this work.

Layer	Material/Paste
Substrate	Type 304/302 Stainless Steel
Dielectric	ESL 4916
Bottom Electrode(Au)	ESL 8884
Top Electrode (Ag)	DuPont 5000
PZT	PZT-5H University of Southampton

5.3.2. Screen Printing Process

The substrate was printed in University of Southampton Class 100 clean room using a DEK 248 CERD printer. A process flow chart outlining all the steps employed in the report was listed in Figure 5.9. The screen printing process commenced with one layer of dielectric material printed to cover the substrate. The film was then dried in a belt furnace at 125˚C for 15 minutes. A sequence of printing and drying a dielectric layer on the other side of the substrate was repeated to create a bimorph structure for the PZT layers. Both dielectric layers were subsequently fired on the thick-film belt furnace with a peak temperature of 850˚C. Once the dielectric layer was fired, two single bottom electrode layers of gold were added on both sides of the substrate using the same process. On the bottom electrode, the PZT layer was added consisting of two prints. The first layer was dried at 125˚C for 15 minutes, and then a second layer was printed directly on top and dried. After the PZT layers were fired, top electrode layers of silver were printed and dried as well using the same process. This printing and curing

sequence avoids firing the device at high temperature again. Drying and firing conditions depend on the type of printed material and substrate. A summary of drying and firing profile for each layer of material is shown in Table 5.5. The furnace operator can control the peak temperature, through speed, and drying time.

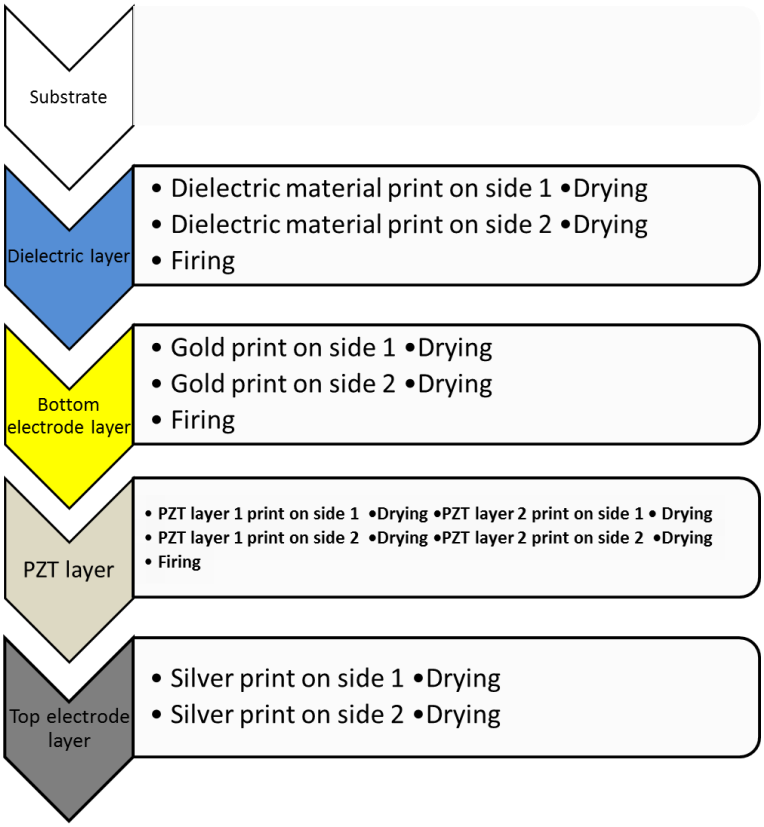

Figure 5.9. Flow chart of the screening printing process.

Table 5.5: Drying and firing conditions of materials printed.

Material	Drying Temperature (℃)	Time (mins)	Curing Temperature (℃)	Peak Time (mins)
Dielectric ESL 4916	125	15	850	10
PZT 5H	125	15	850	10
Au ESL8884	125	15	850	10
Ag DuPont5000	125	15	/	/

Two pieces of substrates were fabricated using above processing and a photograph of the final device cutting from the metal sheet is shown in Figure 5.10.

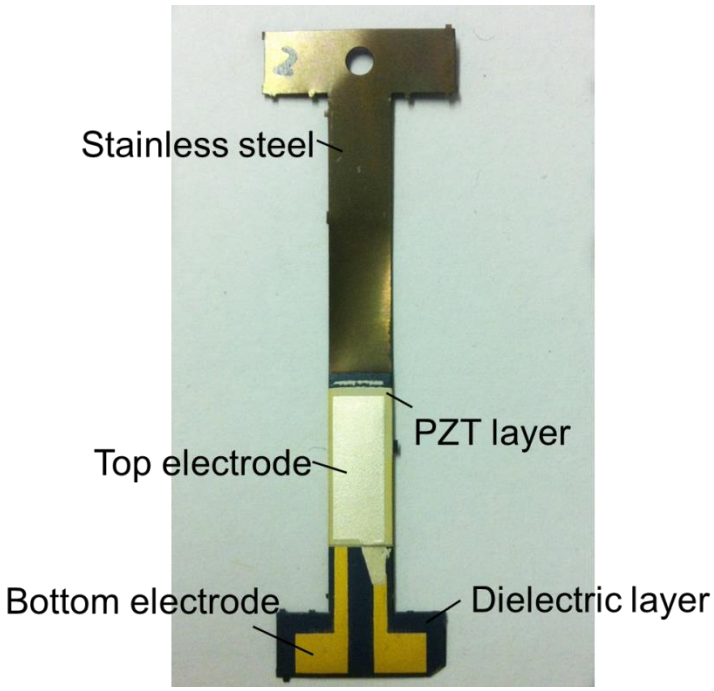

Figure 5.10: Photograph of a printed piezoelectric cantilever in this work.

5.3.3. Poling

Polarisation is the final fabrication step, which is used to enhance the piezoelectric properties of the PZT. The general process of poling involves the following steps: the material is heated up to and held at an elevated temperature (typically around 150˚C). A sufficiently high electric field (usually 2 – 5 MV/m) is applied to the material for certain time to let all ferroelectric domains get oriented in the direction of the electric field, and the material attains saturation polarization. Then the material is allowed to cool down to room temperature with electric field kept on. This is to prevent the sample from depolarising below Curie temperature. Finally the electric field is removed. The material remains in the maximum polarization state with most of the domains oriented in the same direction. A set-up of the polarisation is shown in Figure 5.11. The poling process was undertaken in a chamber with a temperature-controlled hotplate for heating up. Devices were connected electrically to a high voltage DC power supply. Two clips were used to connect electrodes on different sides together, thus the PZT layers on both sides can be poled simultaneously. One alumina block was placed on top to press the beam close to the hotplate surface avoiding nonuniform temperature caused by the interspace between them.

The d_{33} values were measured using a commercial Berlincourt piezometer as shown in Figure 5.12. However, clamping effects of the substrate may reduce the effective d_{33} coefficient in this measurement [129]. The effect of poling conditions including temperature, time and electric field on this piezoelectric material will be further discussed in the next section.

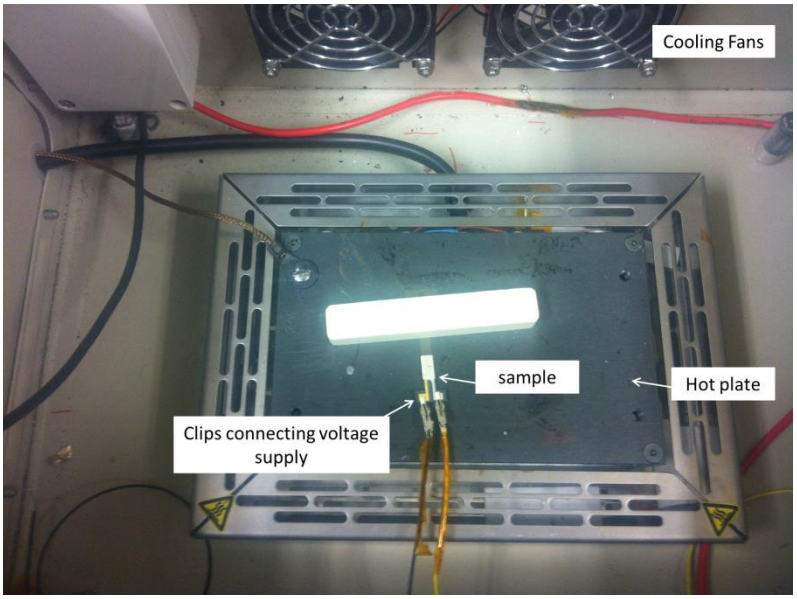

Figure 5.11: The setup of the polarisation process.

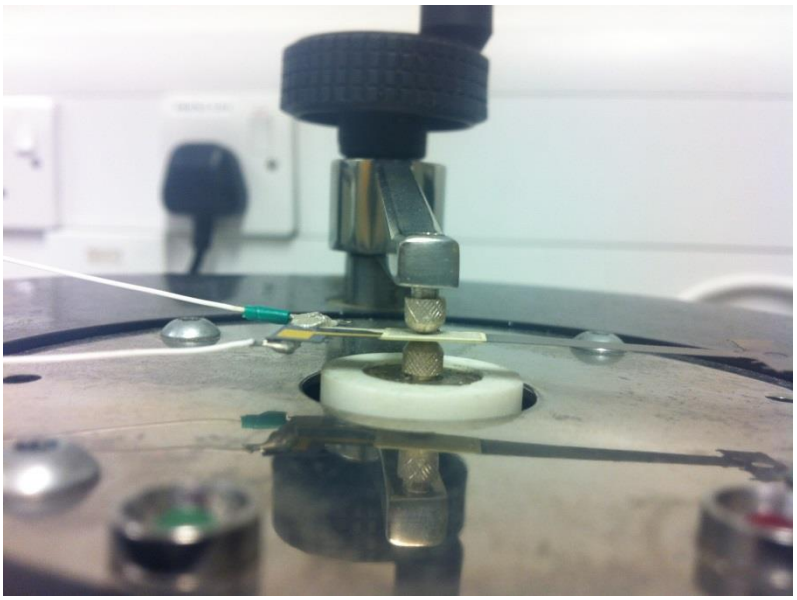

Figure 5.12: The setup of the d_{33} measurement by piezometer.

5.3.4. Results and Discussion

After printing four pieces of substrates, 36 samples were finally achieved and poled. Other samples were failed because of a short circuit causing by cracks on the PZT layer during firing process. It was found that a maximum value of d_{33} obtained was around 90 pC/N when the polarisation temperature, time and field strength are 225˚C, 30 minutes and 4 MV/m respectively.

5.3.4.1 Firing Condition

The furnace firing profile affects the piezoelectric properties due to the change in stoichiometry of the film and the degree of particle sintering occurred during the firing process [30]. Typical firing temperature for screen-printed PZT thick films is 800˚C – 1000˚C as PZT films at temperature above 800˚C show acceptable adhesion and sintering. In some research, the higher firing temperature produces an increase d_{33} value [129], hence two firing profiles with different temperatures (950˚C and 850˚C) were used for two substrates respectively.

After firing, however, some devices failed due to electrical shorting between the top and bottom electrodes. Since they had not been subjected to a high-voltage treatment prior to measurement; the most likely explanation is a conductive path has been induced between the electrodes through the PZT layers. An examination of the device surface under microscope (Figure 5.13(a)) shows the presence of some cracks on the PZT layer. If the cracks span the entire thickness of the layer, it is possible for a conductive path between the upper and lower surface of the layer to be created. These through-thickness cracks are not present on the other substrate (Figure 5.13(b)); thus it is reasonable to surmise that they arose as a consequence of the high firing temperature.

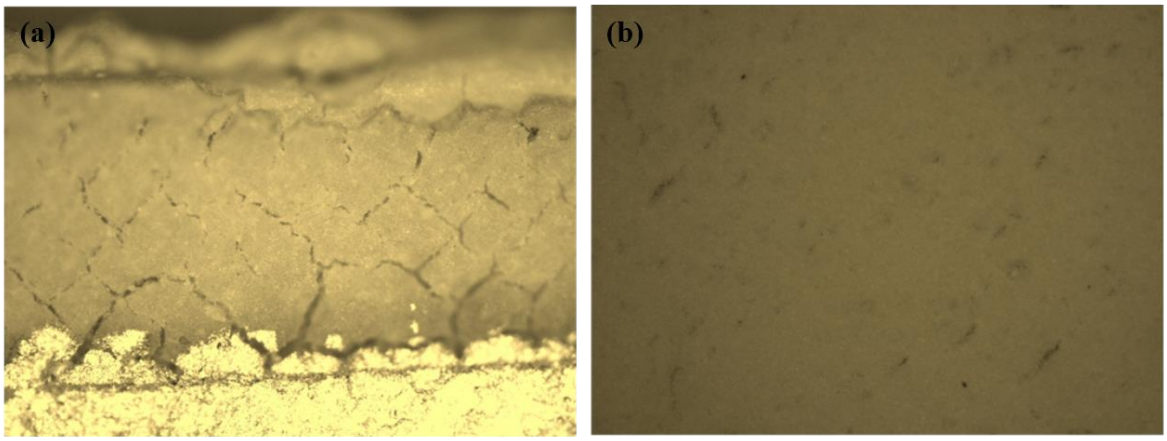

Figure 5.13: Microscope images of PZT surface fired at (a) 950°C and (b) 850°C.

5.3.4.2 Poling Conditions

In this report, six samples divided into two batches were prepared for poling parameter optimization. In all cases five readings were taken on each device with an average recorded. The necessary poling voltage was calculated by:

$$V_{poling} = \text{field strength} \times \text{PZT thickness} \qquad \text{(Equation 5.1)}$$

Where the thickness of the PZT layer was measured using electric micrometre.

The first batch was poled at constant field strength of 3 MV/m with temperature varying from 150˚C to 225˚C for duration of 10 – 120 minutes. At each of four temperatures with five different time periods, one sample was poled as described above. Results in Figure 5.14 show that the value of d_{33} increases with both temperature and time of poling. Devices poled at higher temperatures achieve a higher value of d_{33} at a faster rate. For instance, at 150˚C the value of d_{33} achieved after 30 minutes is 62% of the value after 120 minutes. While at 225˚C the 30 minute values were 93% of 120 minutes values. However, beyond 225˚C samples are found to be short circuit. Therefore the optimal value of temperature should be 225˚C. If this poling process was continued for longer time periods, the increase would prove to be exponential as a maximum polarization is achieved [130].Consequently long poling times are not necessary to obtain reasonable d_{33} values. In addition, the increase of d_{33} over 30 minutes is not significant, thus a poling time of 30 minutes is enough for sufficient d_{33} values achieving.

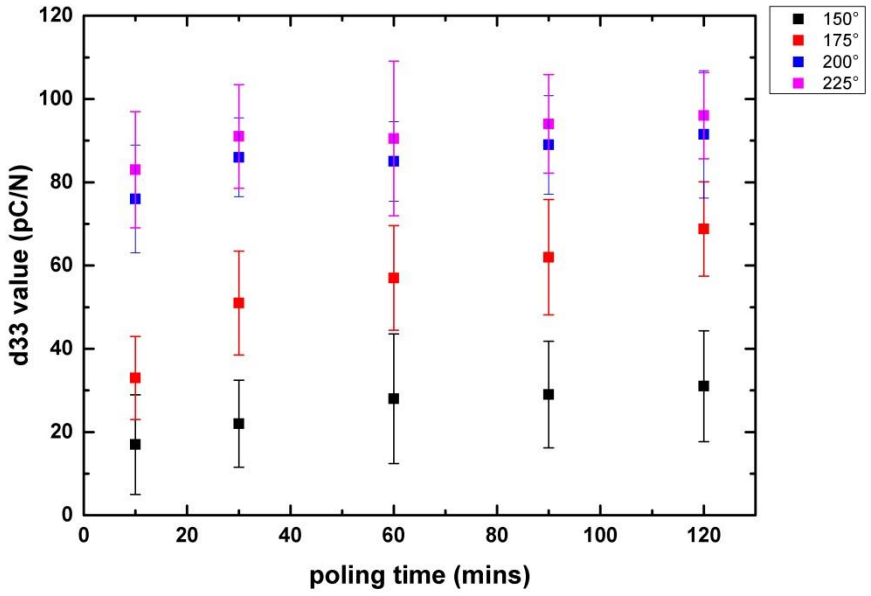

Figure 5.14: Measured d_{33} values with variatiosn of poling temperature and time at a field strength of 3 MV/m.

Next, a study of the electric field was conducted. Two samples were poled at temperature of 225˚C with electric field strength ranging from 1 MV/m to 5 MV/m and poling duration of 30 minutes. As shown in Figure 5.15 it is found that improved value of coefficient is achieved when the poling voltages are increased. Nevertheless the piezoelectric layer suffered electrical

short circuits when it is polarised with electric field strength greater than 4 MV/m. Therefore, all the samples were polarised at slightly lower field strengths to prevent the high voltage from damaging the device.

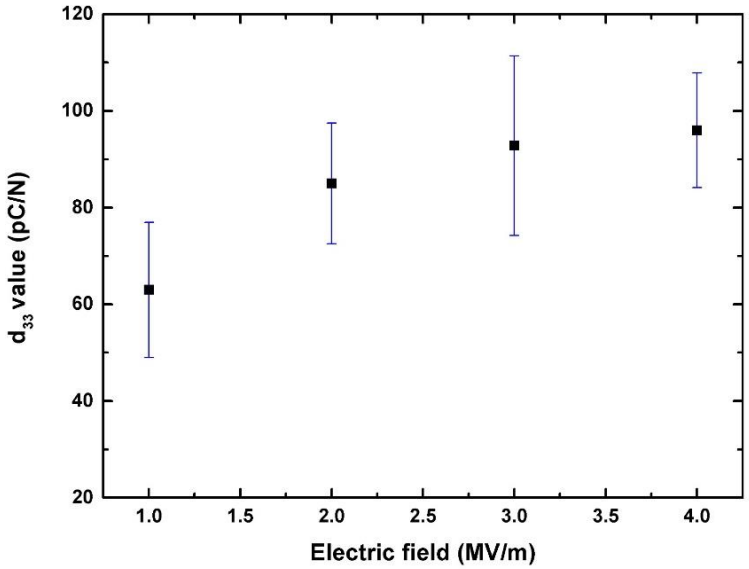

Figure 5.15: Measured d_{33} values at different electric fields.

During the polarization, the combined effect of high electrical field and high temperature applied sometimes led to increased conductivity or even electrical breakdown. To maintain the high level of poling, this needs to be avoided by reducing the temperature or poling field. Alternatively, using pulsed fields to apply electric field for short periods of time is an effective way.

5.4 Testing of the Wind Generator

A prototype was fabricated based on the results from Chapter 4, which has a total volume of 37.5 cm^3 as shown in Figure5.16. Then experiments on a shaker and in an actual airflow were carried out to investigate the performance of the harvester. Based on the testing result in Section 4.4, experiments in this chapter will further optimise the structure to achieve the lowest threshold wind speed as well as the highest power output of the device. Adjustable parameters include the position of the bluff body, the attack angle of the aerofoil, the length of the PZT layer and the adding mass. Testing the energy harvester required a long time because of some periodic instability.

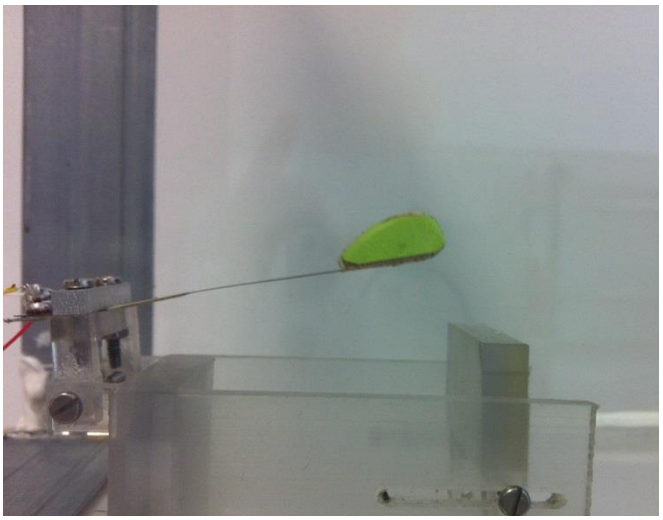

Figure 5.16: The prototype piezoelectric harvester fabricated in this work.

5.4.1. Experimental Setup

The average wind speed in the environment is around 5 m/s, depending on the area, the season and the time of the day [115]. Close to the ground however, important effects of viscosity appear and lead to a reduction of the velocity. For internal flow, such as ventilation ducts, the air velocity can be up to 8 m/s in large ducts and down to 1 – 2 m/s close to the exit in rooms. The air duct application has significant advantages for wind energy harvester, the constancy of the wind, the absence of rain; snow and ice provide a well-controlled environment.

Airflow experiments were carried out in the centre of a wind tunnel, as illustrated in Figure 4.9 with the same conditions. During the tests, the voltage across a load resistance was measured with an oscilloscope in order to determine the power generated by the wind energy harvester, meanwhile the operation wind speeds of the harvester were measured by the anemometer.

As shown in Figure 5.17, testing of the harvester was also performed on the shaker with an accelerometer to determine its resonance frequency. The structure was firmly attached to the vibrating stage and the harvester voltage output was monitored on an oscilloscope. A programmable resistance box and a PC with LabVIEW software was used to collect the data.

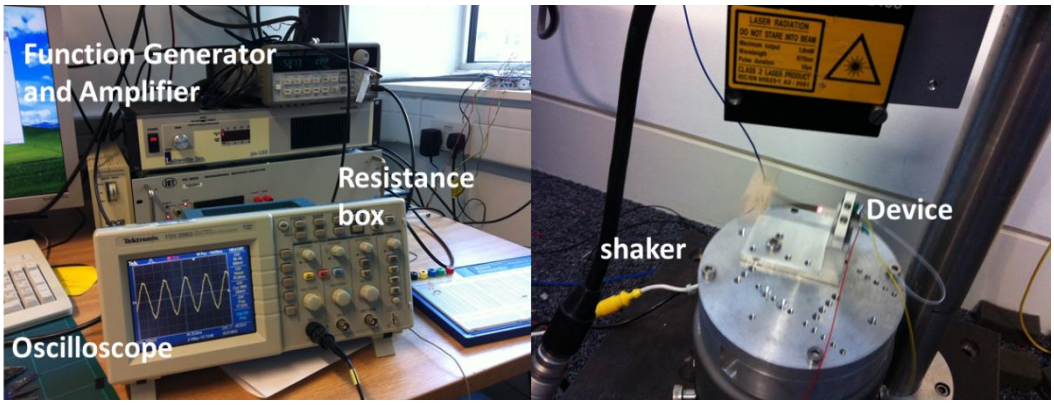

Figure 5.17: Setup of the testing process on the shaker.

5.4.2. Experimental Results

Experimental results were used to estimate the performance of the harvester focusing on two aspects; the threshold wind speed and the output power. When reading the output voltages, for each measurement the average voltage was calculated from three observed values.

5.4.2.1 Attack Angle

The piezoelectric generator has the same structure as the prototype in Chapter 4. However, the PZT element printed at the root of the cantilever changes the total stiffness of the beam, thus altering the dynamic behaviour of the cantilever. In this way, for a given attack angle the position of the wing is slightly higher than that without magnets attached. Therefore further testing was undertaken to investigate the optimal attack angle of the wing with piezoelectric material (length of 13 mm) attached on the beam. Figure 5.18 illustrates the threshold wind speed at different attack angles with the same position of bluff body (distance of 5 mm, height of 20 mm). The attack angle tested was ranging from 0° to 30° with a step of 1°.It can be seen that the trend of threshold wind speed at different attack angles are similar to the results in the previous chapter. The optimum attack angle at which the threshold wind speeds are lowest (below 2 m/s) is between 4° and 10°. When attack angle is larger than 10°, the threshold wind speed increases dramatically with the increasing angle.

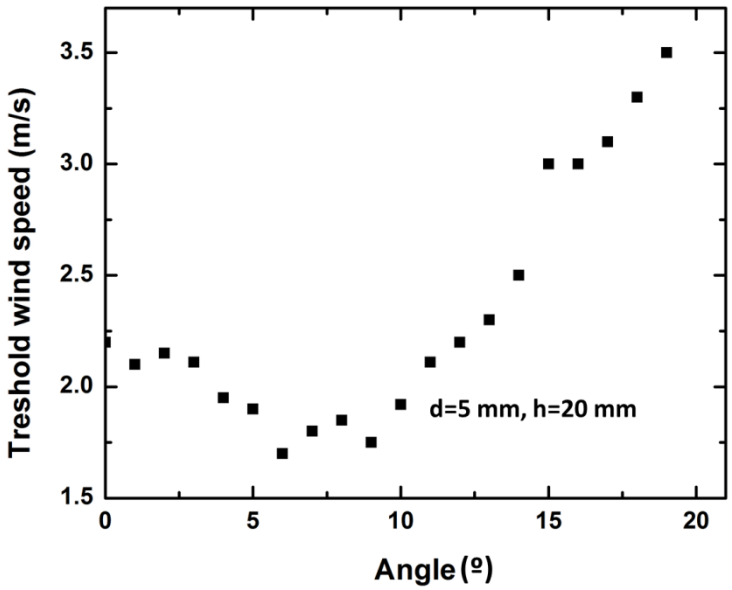

Figure 5.18: Threshold wind speed at different attack angle (distance = 5 mm, height = 20mm).

5.4.2.2 Position of Bluff Body

The piezoelectric generators in this chapter have the same mechanical structure as that in Chapter 4; consequently the influence of the bluff body should also be the same. The optimum position of the bluff body has already been investigated numerically and experimentally in previous chapters, the results shown in Table 4.5 were using as a reference for the bluff body position in this section. As listed in Table 4.5, four optimum positions of the bluff body are: distance of 3 mm, height of 20 mm; distance of 5 mm, height of 20 mm; distance of 7 mm, height of 19 mm; and distance of 11 mm, height of 16 mm. The performance of the harvester was tested in these four configurations. As shown in Figure 5.19, testing of the output power with various bluff body positions is performed at airspeed of 2 m/s to 7 m/s with a resistor of 900 kΩ. The maximum RMS output power occurs in 7 m/s wind from a configuration with distance of 11 mm and height of 16 mm. It can be observed that at distance below 5 mm, the performance at high wind speed (higher than 4 m/s) is not stable, thus resulting in even lower power output. Therefore, for further tests the position of the bluff body is chosen to be 11 mm in distance and 16 mm in height.

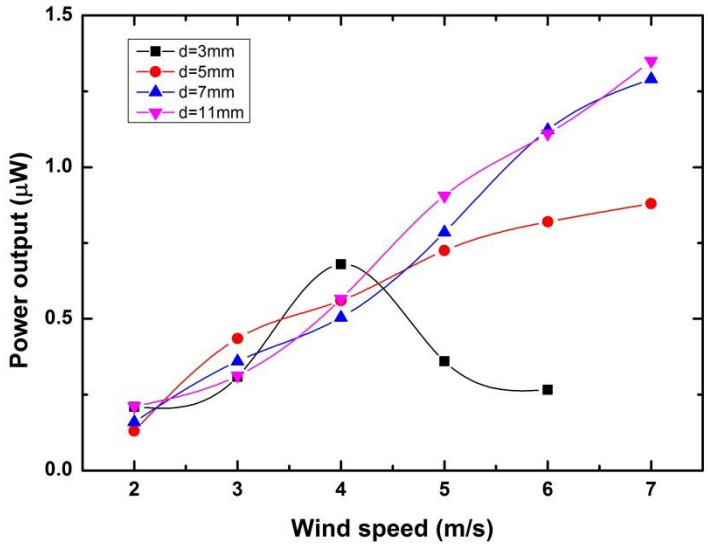

Figure 5.19: RMS power output vs. wind speed for four configurations (distances of 3 mm, 5 mm, 7 mm and 11 mm; height of 20 mm, 20 mm, 19 mm and 16 mm respectively; attack angle = 6°, lines plotted are used to indicate the trend).

5.4.2.3 Adding Mass

Considering that adding proof mass could increase tip amplitude of the cantilever as discussed in Section 4.4, the addition of extra mass was also investigated. Tests were carried out by measuring the threshold wind speed and the power output for different values of added mass. The additional mass was ranged from 0.1 g to 2 g with increments of 0.2 g. All tests were carried out with the optimum position of the bluff body. The attack angle was set to 6° originally and varied with different values of mass added as shown in Table 4.5. It is found that increasing the proof mass causes an increase in the threshold speed as shown in Figure 5.20. For further investigation, additional mass with four different values were placed under the wing in the centre of the cantilever tip to measure effect of increasing mass on the output power. Results verify that adding suitable weight of mass does not show a significant improvement in the output power, and furthermore it is not desirable to increase the threshold wind speed (shown in Figure 5.21).

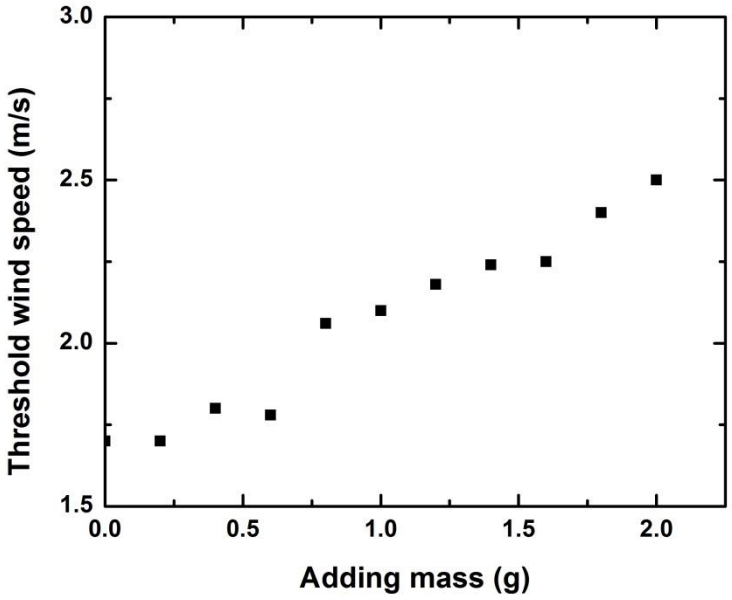

Figure 5.20: Threshold wind speed with variable weights of masses (distance = 11 mm; height = 16 mm).

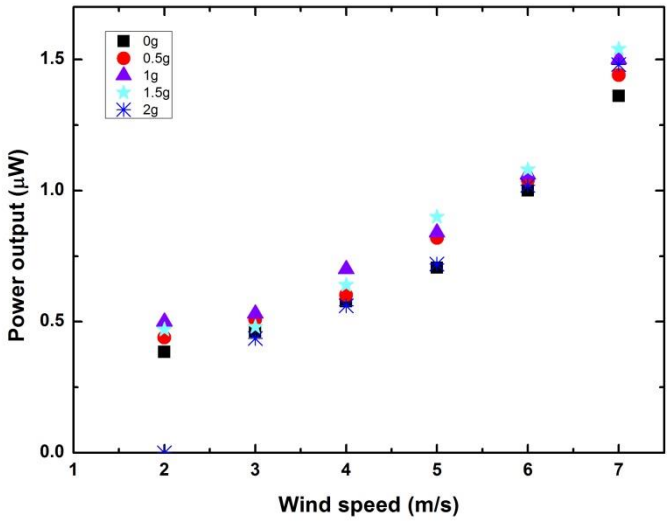

Figure 5.21: RMS power output at variable wind speed with different weights of masses (distance = 11 mm; height = 16 mm; load resistance = 800 kΩ).

5.4.2.4 Length of the PZT

The length of the PZT layer is an important consideration for the performance of the harvester as discussed in Section 5.13. For testes in previous sections, the length of the PZT was 13 mm,

which can achieve a maximum output power at 1.35 μW. However, this value is quite low compare with the simulation result. Therefore six samples were tested to evaluate the influence of the PZT with lengths varying from 11 mm to 16 mm respectively. Figure 5.22(a) shows the natural frequencies of the cantilever with different lengths of PZT section. The performance of these samples is compared in Figure 5.22(b) with the optimum structure obtained above. It can be seen that although PZT layer with the length of 16 mm has a slightly higher threshold wind speed (2 m/s) and natural frequency (20 Hz), it achieves the maximum RMS power output. As a result, this length is chosen for the further testes and the final performance of the device.

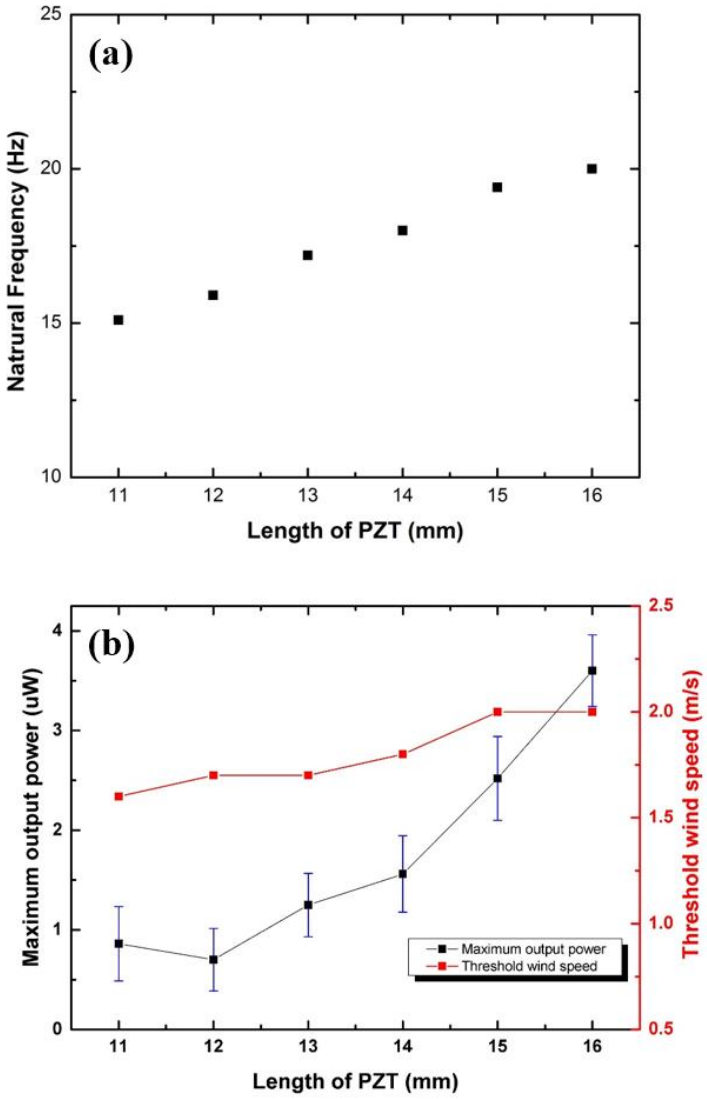

Figure 5.22: (a) Natural frequencies of the cantilever with different PZT lengths; (b) RMS power output and threshold wind speed versus different PZT lengths (attack angle = 6°; distance = 11 mm; height = 16 mm; load resistance = 900 kΩ, lines plotted are used to indicate the trend).

5.4.2.5 Optimum Load

For tests in previous sections, the resistive load was set to be 900 kΩ. When the piezoelectric harvester is placed on the shaker table at the resonance frequency, namely 20 Hz, a standard curve for load resistance is noted, as seen in Figure5.23. The maximum power output is found paired with a resistor of 900 kΩ. In the wind tunnel, the output power of the harvester for a variety of resistive loads is also plotted in Figure5.24. At different levels of wind speed, the ideal value is not as clearly defined; however, results follow a similar trend. The power output at the chosen resistance of 800 kΩ is comparable to maximum power for all test cases, and is thus determined to be a sufficient load for these initial investigations.

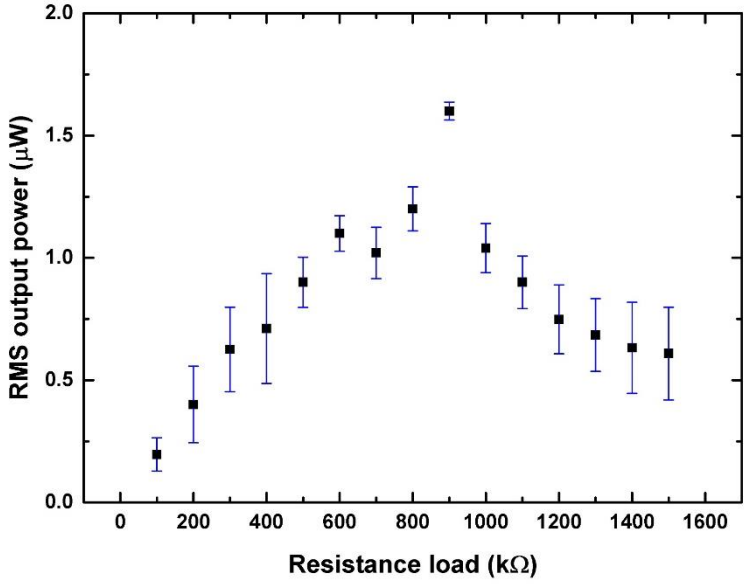

Figure 5.23: Output power with a varying resistive loads on the shaker.

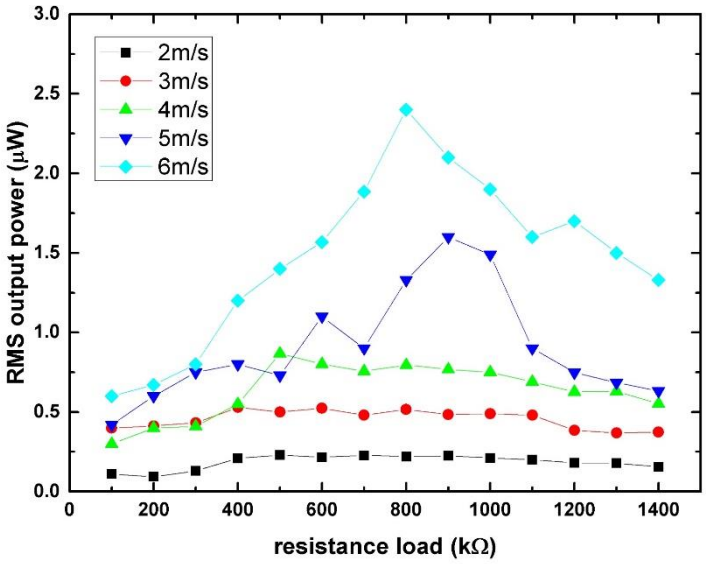

Figure 5.24: Output power with varying resistive loads at different wind speeds in the air duct (lines plotted are used to indicate the trend).

5.4.2.6 Final Performance

For the results presented in the previous four sections, a final design was identified that optimized the parameters of this device as listed in Table 5.6. The graph in Figure5.25 (a) shows the ideal performance that could be achieved for the wind harvester in varying flow speed conditions. As can be seen from the graph, the maximum output power (3.6 μW) is achieved at wind speed of 6.5 m/s. However, the performance of the device is not stable at this wind speed. The value of the output voltage has a large variation which can be seen form the error bar in the figure. In addition, at wind speed larger than 6.5 m/s, the performance is more unstable and results in even lower power outputs. The open-circuit output voltage curve with the maximum RMS value of 1.8V is shown in Figure5.25 (b). However due to the high impedance, this value may not be sufficient for simple power conditioning circuitry as when the device is connected to the power conditioner, the voltage can drop to unacceptably low level.

Table 5.6: Optimal parameters of the final device.

	Unit	Value
Distance of the bluff body	mm	11
Height of the bluff body	mm	16
Attack angle	º	6
Length of PZT	mm	16

Optimum Load	kΩ	800

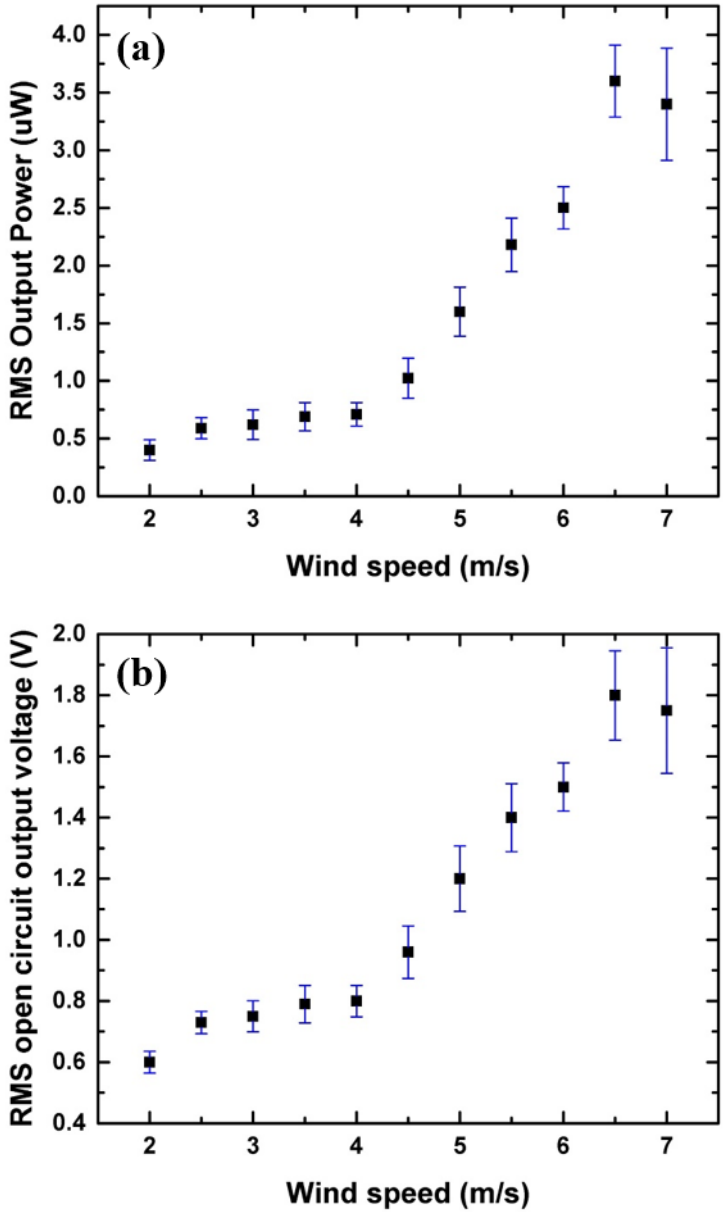

Figure 5.25: (a) RMS Output power in varying flow speed conditions with optimal configuration and load. (b) RMS open circuit output voltage in varying flow speed conditions with optimal configuration.

5.4.3. Comparison

5.4.3.1 Output Power

In this section, both natural frequency and the output power with different lengths of PZT layer were compared. The natural frequency from experimental and simulation results were plotted in Figure 5.26. It can be seen that estimated natural frequencies from the simulation result are higher than the experimental results. The reason could be the dimensions of the screen printed parts on the beam as well as the aerofoil are slightly different from the simulation parameters.

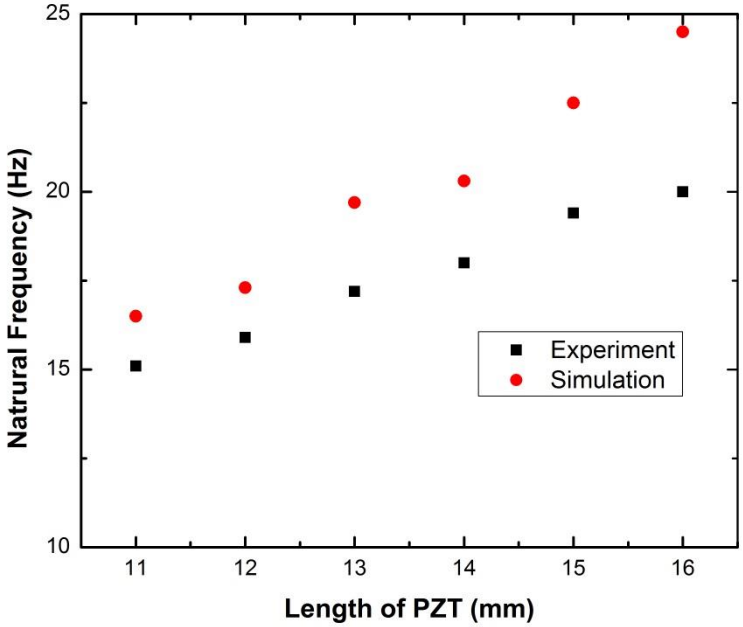

Figure 5.26: Comparison of natural frequency of the cantilever from simulation and experimental results with different PZT lengths.

The damping ratio for the cantilever is an important parameter used to calculate piezoelectric properties, and it can be estimated by:

$$\zeta_T = \frac{1}{2Q_T} \qquad \text{(Equation 5.2)}$$

Where Q_T, the total Q-factor can be determined from an experiment by dividing the measured fundamental natural frequency of the structure f_0, by the full width at half maximum electric output power Δf, according to

$$Q_T = 2\pi \frac{Stored\ vibration\ energy}{Energy\ lost\ per\ cycle\ of\ vibration} = \frac{f_0}{\Delta f} \qquad \text{(Equation 5.3)}$$

The experiments were carried out on the shaker in Figure 5.17. The cantilever was excited over a range of frequencies and the value of the full bandwidth at half maximum electrical output power was taken into equation above to calculate the damping ratio. Figure 5.27 shows that the

calculated values of the total damping ratio for different cantilevers with the measured Q-factor value.

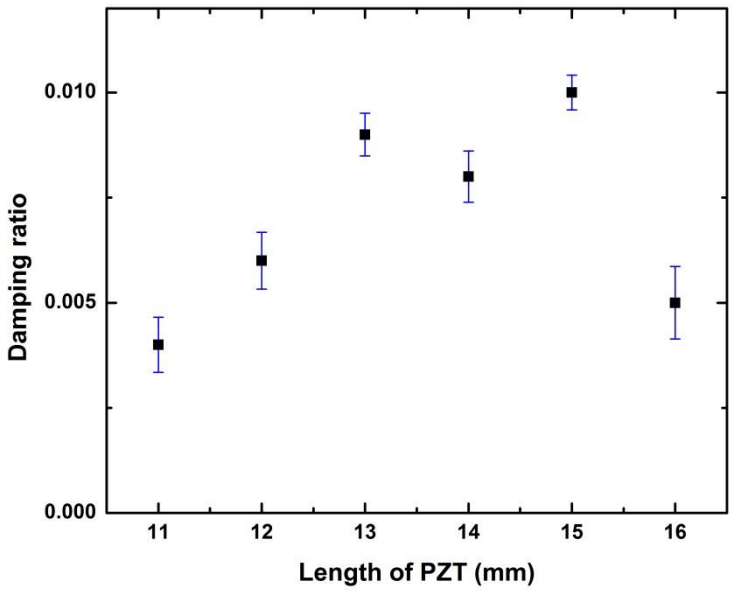

Figure 5.27: Calculated damping ration with different length of PZT layer.

With the damping values tested, the output power could be estimated using Equation 3.25. Figure 5.28 compares the output power from theoretical calculation, experimental work and simulation result. It is obvious that the output powers in the tests were much lower than the expectation values of the calculation and simulation results. Especially with the 11 mm long PZT layer device, a low output power of 0.86 μW was achieved, which was much lower than the calculation (4.76 μW) and simulation result (4.5 μW). The most likely explanation for this could be the reduced displacement of the part of the cantilever that has the PZT element printed on it. The PZT element adds stiffness to the beam due to the presence of the printed piezoelectric and electrode layers. As the stiffness of the printed and unprinted sections of the cantilever are quite different, the majority of the overall cantilever displacement might only be occurring on the unprinted section and the PZT element experiencing lower than expected strains. However, with the increasing length of the piezoelectric part of beam, the problem could be reduced. In order to verify this assumption, displacements at different points on the beam with 11 mm long PZT layer were measured in both simulations and the experiments.

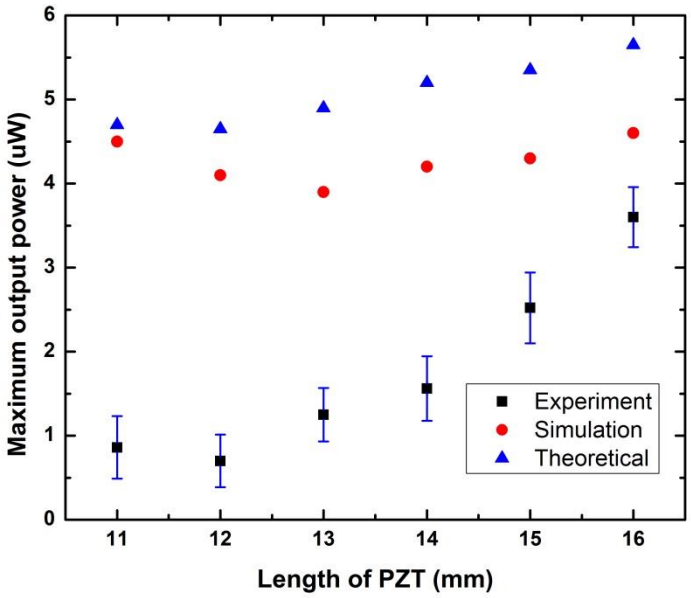

Figure 5.28: Power outputs from simulation and experimental results with different PZT lengths.

5.4.3.2 Displacement

In the simulation, 8 key points are selected along the beam at different lengths. They are 1mm, 4mm, 7mm, 10mm, 15mm, 20mm, 25mm, and 30mm from the clamping edge respectively. In the experiments, 8 points at the same positions were also selected for measurement as shown in Figure 5.29,

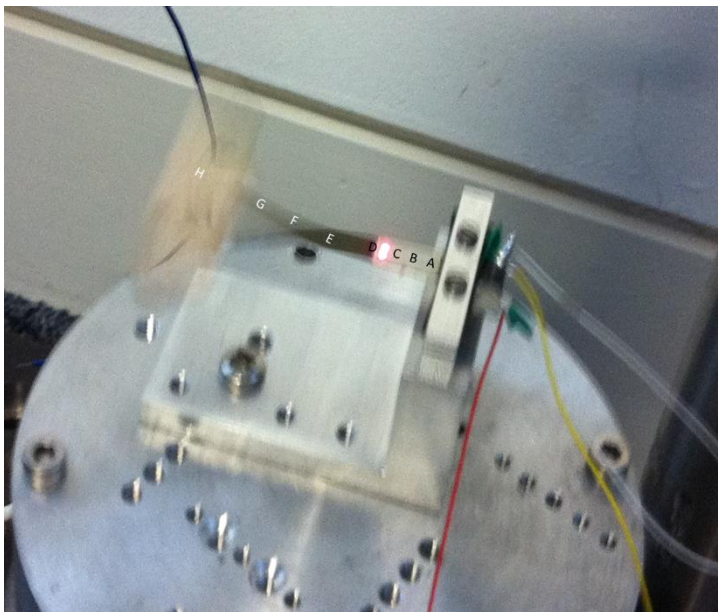

Figure 5.29: Points selected on the cantilever for the displacement measurements.

Results were plotted in Figure 5.30. From experimental results, a significant displacement was observed at points E, F, G, and H, while the displacements of the other points were less than 0.2 mm. Therefore the PZT element is experiencing low levels of strain and hence generating relatively low level of power. However, this trend is not obvious in simulation result. Consequently it is reasonable to surmise the low output power in the experiments as a result of the added stiffness of the beam from the presence of the printed piezoelectric layers. This reason can also explain the fact that increasing the inertial mass did not increase the power output as expected. The adding mass does increase the cantilever displacemnt as discussed in Chapter 4, but not the strain on the PZT section.

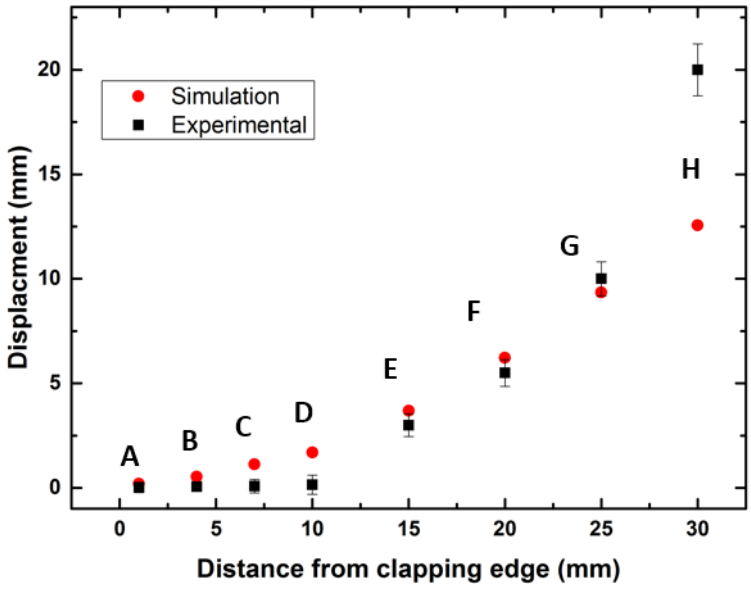

Figure 5.30: Measured cantilever displacements at different points

5.4.3.3 Different Materials

Due to the added stiffness of the PZT material resulting in low power output, the performance could be improved by using a flexible piezoelectric material such as PVDF. To estimate the result of this, simulations were also run with PVDF material using the same dimensions as PZT devices. As the PVDF device will not be fabricated and tested, the properties of the material are from the Piezotech leaflet [128]. The physical properties of PVDF material are listed in table 5.7. In the simulation, the PVDF patches are laminated to the beam with epoxy matric. The results of simulation are shown in figure 5.31. It can be seen that with PVDF materials, the power outputs are all below 0.5 μW. This is mainly because of the low piezoelectric charge

constant of PVDF material. Therefore using flexible piezoelectric materials cannot solve the low power output problem.

Table 5.7: Parameters of PVDF device.

	Parameter	Unit	Value
l_{pv}	PVDF layer length	mm	11
w_{pv}	PVDF layer width	mm	5
t_{pv}	PVDF layer thickness	μm	60
ρ_{pv}	Density of PVDF	kg/m^3	1780
ρ_{ep}	Density of Epoxy matrix	kg/m^3	2150
l_{ep}	Epoxy matrix layer length	mm	11
w_{ep}	Epoxy matrix layer width	mm	5
t_{ep}	Epoxy matrix layer thickness	μm	20

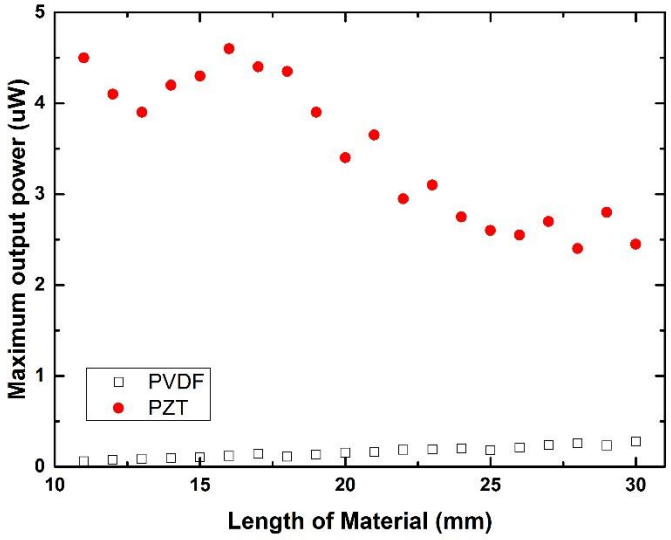

Figure 5.31 Output power of PZT and PVDF materials with differnent lenghts

5.5 Conclusion

In this chapter, a prototype of piezoelectric wind harvester with a total volume of 37.5 cm^3 (5 cm × 3 cm × 2.5 cm) was fabricated and tested. The dimensions of the beam are 35 mm×5 mm×0.1 mm and the dimensions of the aerofoil are 30 mm ×11mm with a maximum oscillating amplitude of 20 mm. The piezoelectric transducer was produced by normal thick-film printing steps, including paste preparation, screen-printing deposition, drying, firing and poling process. Properties of the piezoelectric cantilever depended on poling conditions including the temperature, time and electric field applied. With optimal combinations of these parameters, a maximum value of d_{33} of 92 pC/N was obtained.

A set of experiments both on shaker and in the air duct were carried out to investigate the performance of the harvester. After testing, the results showed relatively good correlation with the previous ones in Chapter 4, thus validating the model in this study. Further investigation of the performance was carried out with four configurations and the power outputs with various bluff body positions were tested. The maximum output power occurred in 6.5 m/s wind speed from a configuration with distance of 11 mm and height of 16 mm, which was chosen for final tests. It can also be observed that at distance smaller than 5 mm, performance at high wind speed was not stable, which resulted in a lower power output.

The length of the PZT layer was also investigated by testing six samples with different lengths from 11 mm to 16 mm respectively. Results showed that with the length of 11 mm, the threshold wind speed was around 1.5 m/s, but the maximum output power was only 0.86 μW because of the added stiffness of the beam from printed PZT parts. This power generation could be improved by increasing the volume of the piezoelectric part of the beam. However, such configurations also suffer from the increasing natural frequency as well as the stiffness of the beam, resulting in relatively high threshold wind speed. As a result, prototype of a length of 16 mm was chosen for the final tests. The optimized device achieved a working wind speed range from 2 m/s to 8 m/s. The power output with optimal load (800 kΩ) was ranging from 0.35 μW to 3.6 μW and the open-circuit output voltage was from 0.6 V to 1.8 V. Results verified the harvester can effectively convert wind energy into large amplitude mechanical vibration without strict frequency matching constraints.

Chapter 6 Electromagnetic Wind Generator

Compared with piezoelectric generators, electromagnetic transducers have the advantage of higher efficiency if there is no size constraints applied. This chapter represents the design and the fabrication of the electromagnetic transducer for the miniature wind generator application where the transducer is constrained in size. Prototypes with the same size as the piezoelectric one are made to test the performance of the harvesters and these will be compared with the piezoelectric version.

6.1 Transducer Design

6.1.1. Design Considerations

The basic operating principle of a magnetic induction system was discussed in Chapter 3. As mentioned, altering geometric configurations will affect the output power of the harvester. Considering the arrangements of electromagnetic transducers presented in this section, changing the geometric configurations include changing the geometries of the magnets and the coils as well as the gap between them. In addition, increasing the magnetic flux density of the magnets and the number of coil turns or decreasing the coil resistance should increase the power output as well. However, increased power output indicates an increased current flow, resulting in a stronger electromagnetic drag force on the magnet, and the oscillation of the harvester may be difficult to start. Thus there will be some complexity to the relationships between these parameters and the power output. It should also be noted that the magnetic flux density can be increased by using a more highly magnetized material or by increasing the size of the magnet. However increasing the size of the magnet will increase other parameters, such as the mass of the magnet and the size of the coil. Another concern should be taken into account in this design was that a moving magnet design in practice is simpler to fabricate as it avoids electrical connection to the mass, while the coil required wires, and moving at high speed could easily break the wires from cyclic stresses. Moreover, the moving magnet attached on the beam will increase the proof mass of the system, which could also increase the electrical power.

6.1.2. Design Configuration

Two commonly used arrangements of electromagnetic transducers were implemented in this work, which were the magnet-through-coil (MTC) induction and magnet-across-coil (MAC) induction as shown in Figure 6.1 and Figure 6.2 respectively. The magnet-through-coil induction consisted of a bar magnet that translates through a cylindrical coil. According to Faraday's Law, when the magnet moves towards and away from the coil, the magnetic flux moves thus inducing an Electromotive Force or emf, in other words a voltage across the coil ends. The magnets-across-coil induction systems consisted of two magnets separated by an air gap, in which the coil is located. The magnets are fixed to the cantilever and move relative to the fixed coil thus generating a voltage across the coil. Both systems used essentially similar methods of implementing an electromagnetic transducer with magnets attached to the wing for oscillation while the coil is fixed to the base.

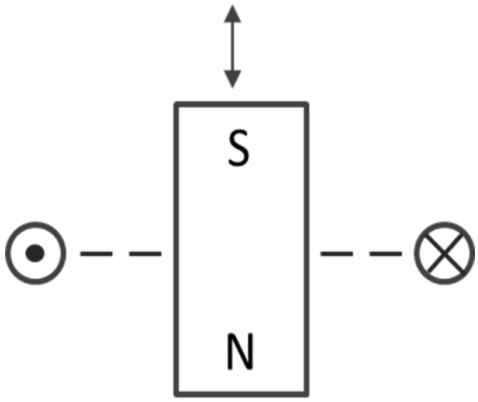

Figure 6.1: Cross-sectional view of the electromagnetic transducer with magnet through coil induction.

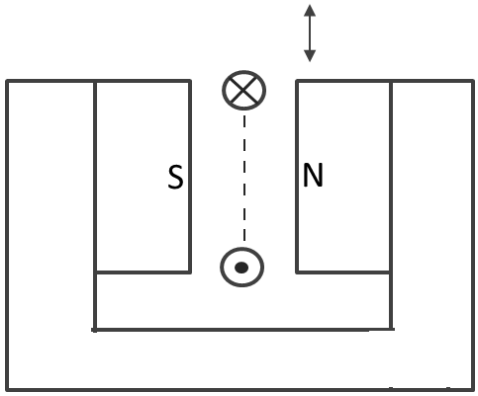

Figure 6.2: Cross-sectional view of the electromagnetic transducer with magnet across coil induction.

6.1.2.1 Magnet-through-coil Induction Design

In this design, the magnet was mounted in the middle of the underside of the cantilever while the coil was fixed under it. Due to the air flow, the beam oscillated with the magnet moving towards and away from the coil to produce electricity. The advantage of this kind of magnetic induction system is easy to build. However the coil never experiences a complete flux reversal, thus resulting in relatively low voltage and power generation. In order to improve the output, the magnet was extended further from the wing. The system was implemented as seen in Figure 6.3.

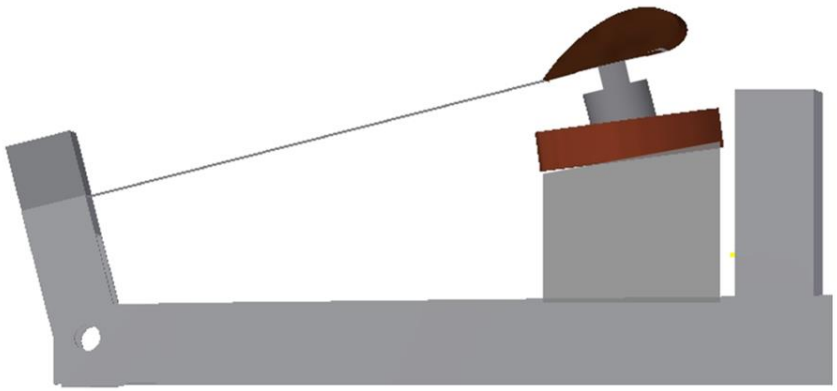

Figure 6.3: Transduce design with magnet through coil induction in this work.

6.1.2.2 Magnets-across-coil Induction Design

In this design, one stator coil was fixed and two translator magnets were attached onto the cantilever. A schematic diagram of the electromagnetic generator was showed in Figure 6.4. Although this design is more complicated to build than the former one, it had a higher potential power output from the transducer because the coil experience complete flux reversals. However two magnets attached onto the beam increased the proof mass, which could result in relatively high threshold wind speed for operation. Since the permeability of a magnetic material like steel is higher than that of air, steel magnet keeper was used to form a magnetic flux path linking the magnets and maximising the flux density through the coil. A gap was required between the magnets for the coil to pass through.

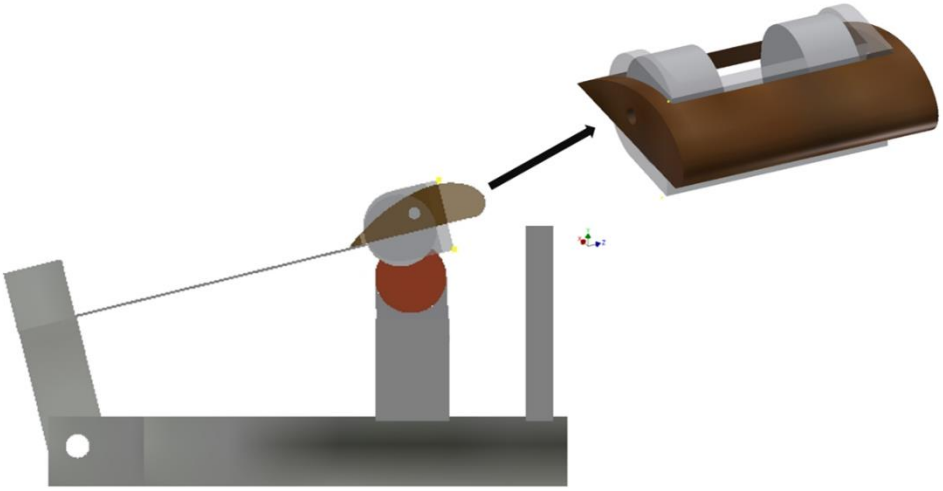

Figure 6.4: Transduce design with magnet across coil induction in this work.

6.1.3. Materials Chosen

It is important to choose a type of magnet that will produce a strong flux density. As NdFeB has a large energy density than most of other permanent materials, NdFeB magnets are being widely used in electromagnetic power generators as high performance magnets. Therefore in this work, high grade (N52) NdFeB magnet bars were selected for the transducer. The wire wound coils were fabricated from enamelled copper wire, which has the lowest resistivity of any metal at room temperature except silver. Beryllium copper was selected to fabricate the beam because it is a spring material with high fatigue strength.

6.2 Testing of the Wind Generator

Two prototypes were fabricated and tested in the air duct to investigate the performance of the harvester.

6.2.1. Prototype Fabrication

The actual devices were shown in Figure 6.5 and Figure 6.6. The cantilevers both had dimensions of 30 mm×5 mm×0.08 mm. As tested in Chapter 4, attached mass should be lighter than 2 g to achieve a threshold wind speed below 1.5 m/s. The magnets sizes available vary from Ø3 mm×1 mm, Ø3 mm×3, and Ø4 mm × 3, Ø5 mm × 3 mm to Ø5 mm × 8 mm. The largest bar magnet size of Ø5 mm × 8 mm, which has a mass of 1.17 g was selected as for the MTC generator design. It was fixed in the middle of the backside of the wing with extension part, which makes the total mass up to 1.62 g. The lowest point of the magnet was positioned

around 1 mm above the coil due to the cantilever banding. The coil was wound using 60 μm thick copper wire. Its outer and inner diameters were 15 mm and 6.5 mm, respectively. The thickness is 3 mm. The coil had a static resistance of 1020 Ω and approximately 3500 turns. For the MAC design, two bar magnets with diameters of 5 mm and thicknesses of 4 mm, which together have the same mass as the magnet of MTC generator, were placed below the wing with an air gap of 5 mm between each other. After adding the steel magnet keeper, the total mass was up to 1.85 g. The static coil had an outer diameter of 6 mm and in inner diameter of 1 mm with a thickness of 3 mm. The wound wire was also 60 μm thick. The resistance of the coil was 260 Ω and about 2100 turns. Both generators had the same overall dimensions with the piezoelectric harvester presented in Chapter 5 of 50 mm× 25 mm×15 mm.

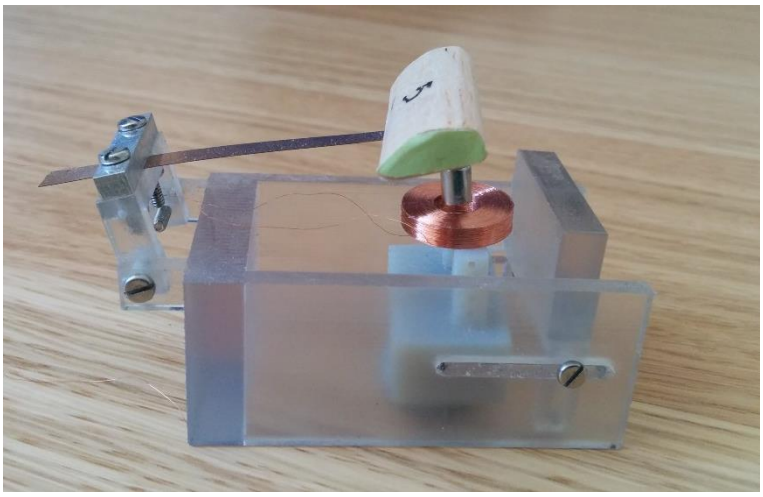

Figure 6.5: Prototype of the MTC harvester fabricated in this work.

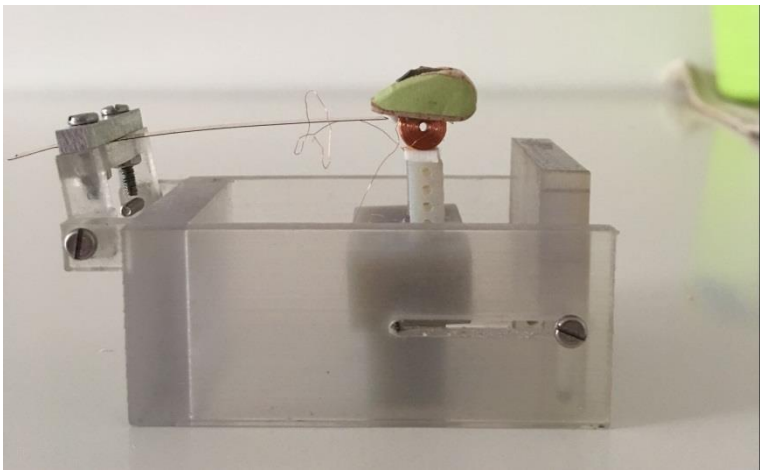

Figure 6.6: Prototype of the MAC harvester fabricated in this work.

6.2.2. Experimental Setup

The experimental work was set up as described in Chapter 5. Tests were carried out in the centre of a wind tunnel with the air flow generated by a centrifugal fan (seen in Figure 4.9), and airspeed can be adjusted from 0 to 8 m/s. During the tests, the harvester was placed near to the end of the steel duct where the air flow is most steady. The voltage across a load resistance was measured with an oscilloscope, meanwhile the wind speeds of the harvester were measured by the anemometer. To get accurate readings of the output voltages, three values were recorded and an average was taken for each measurement. All tests were done at room temperature.

6.2.3. Experimental Results

Experimental results were used to determine the performance of the harvester by means of the threshold wind speed and the output power.

6.2.3.1 Attack angle

In electromagnetic generators, moving magnets were attached on the underside of beam, which increased the proof mass of the system and then increased the electrical power. In this situation, the cantilever initially bends downwards due to the mass of the magnets. Then the position of the wing was lower than that without magnets attached. As a result the optimum attack angle should be different from the results in Chapter 4. Testing was undertaken to investigate the optimal attack angle of the wing with magnets attached. The position of the bluff body was set as 11 mm in distance and 16 mm in length as this is the optimum position for the piezoelectric device. Figure 6.7 and Figure 6.8 illustrated the threshold wind speed at different attack angles of MTC generator and MAC generator respectively. The attack angle tested was ranging from 0° to 30° with a step of 1°. It can be seen that with the same position of the bluff body, the trend of the threshold wind speed at different attack angles were similar. For MTC generators, threshold wind speeds at attack angles from 6° to 11° were lower than the others indicting the optimum angle is in this range, and for the MAC generator, the optimum angle range was 7° to 12°. Those values are slightly higher than the piezoelectric one (4° to 10°) due to extra bending of the beam caused by attached magnets In addition, for attack angles greater than 15°, a threshold wind speeds of both devices were found to increase with increasing angle.

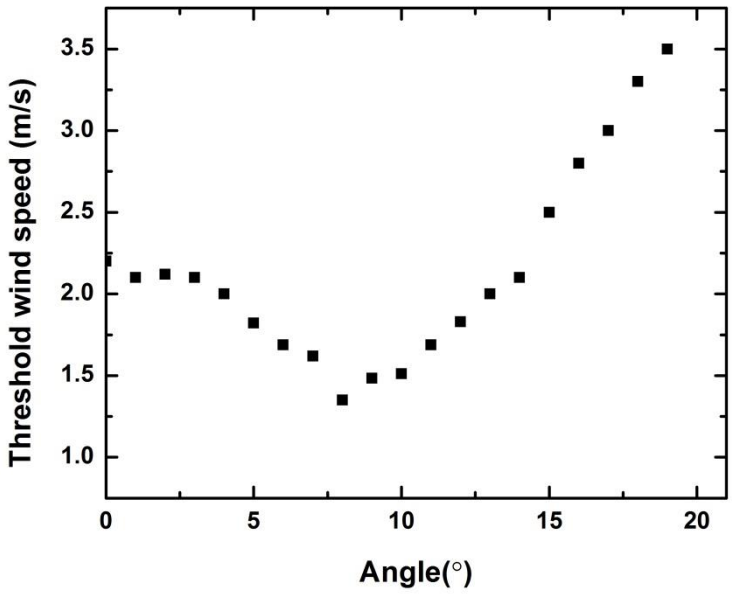

Figure 6.7: Threshold wind speeds at different attack angles in MTC generator (distance = 11 mm and height = 16 mm).

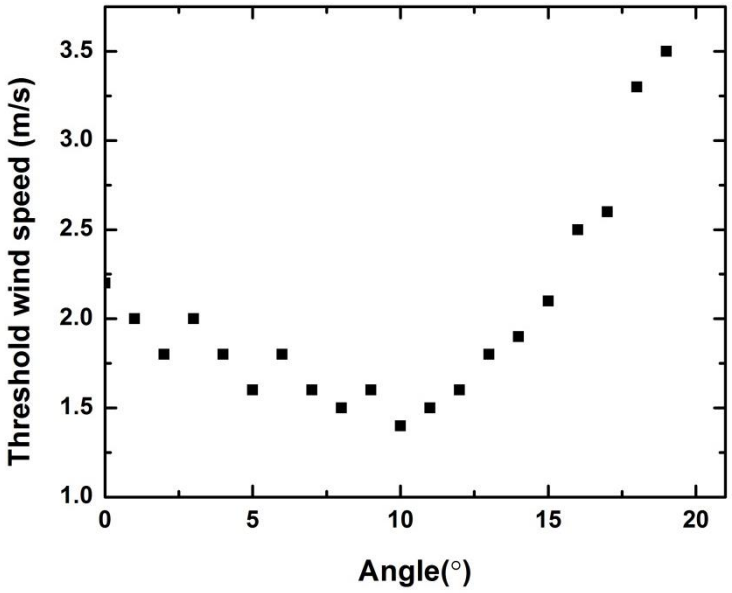

Figure 6.8: Threshold wind speeds at different attack angles in MAC generator (distance = 11 mm and height = 16 mm).

6.2.3.2 Resistive Loads

In order to determine the optimum value of the resistive load for the generators, experiments

were carried out in the wind tunnel. The attack angle was set as 10°, which is within the optimum range for both devices. The position of the bluff body was set as 11 mm in distance and 16 mm in length. The output power of the MTC generator for a variety of resistive loads was tested and plotted in Figure 6.9. It was found that, the optimised resistive load decreased with increasing airflow speeds, from 7.4 kΩ to 2.6 kΩ. The reason is when the airflow is strong; the force acting on the wing to overcome total damping became larger, resulting in larger energy extraction. Figure 6.10 shows the optimum load resistance values at different wind speeds, for the MAC harvester, where the results followed a similar trend clearly. The optimum load decreased from 1.9 kΩ to 0.6 kΩ.

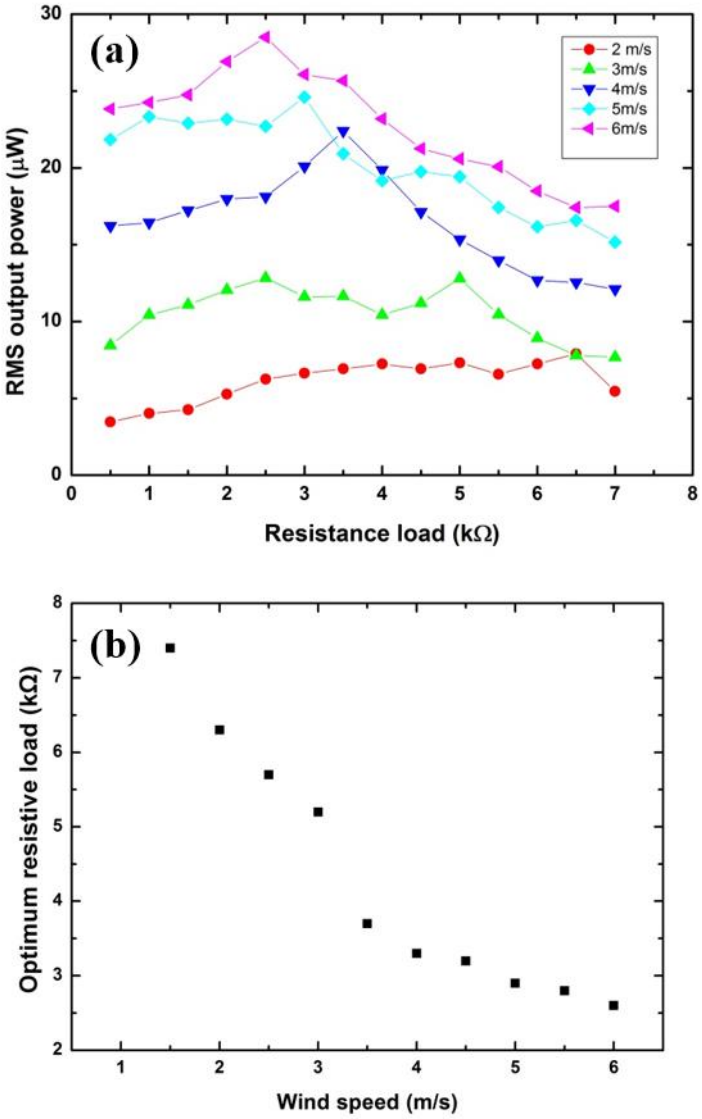

Figure 6.9: (a) Output power with a variety of resistive loads at different wind speeds for MTC generator (lines plotted are used to indicate the trend); (b) Optimum resistive loads at different wind speeds for MTC generator in this work.

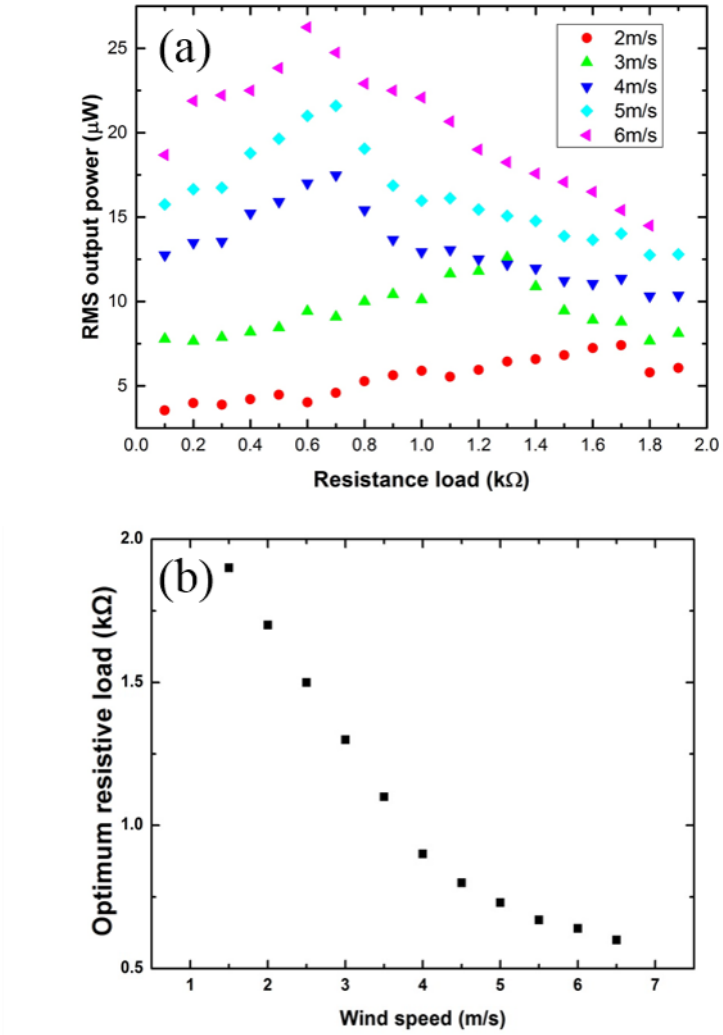

Figure 6.10: Optimum resistive loads at different wind speeds for MAC generator in this work.

6.2.3.3 Position of the bluff body

As tested in Chapter 4 and Chapter 5, the optimum position of the bluff body was already listed in Table 4.5. However, since the electromagnet transducers needed more space for coil and magnets, the distance of the bluff body should be larger than 5 mm from the wing. In addition, involving the magnets and coils changed the structure of the device; therefore position of the bluff body might be different from the previous devices in Chapter 4 and Chapter 5. In order to estimate this influence, tests were carried out on threshold wind speed with different positions of the bluff body. The values of the threshold wind speed at varying distances and heights are shown in Figure 6.11. As can be seen from the 3D bar charts, both MTC and MAC generators were found that distances ranging from 5 mm to 11 mm and height varying from 16 mm to 20 mm were the optimum positions to achieve lower threshold wind speed.

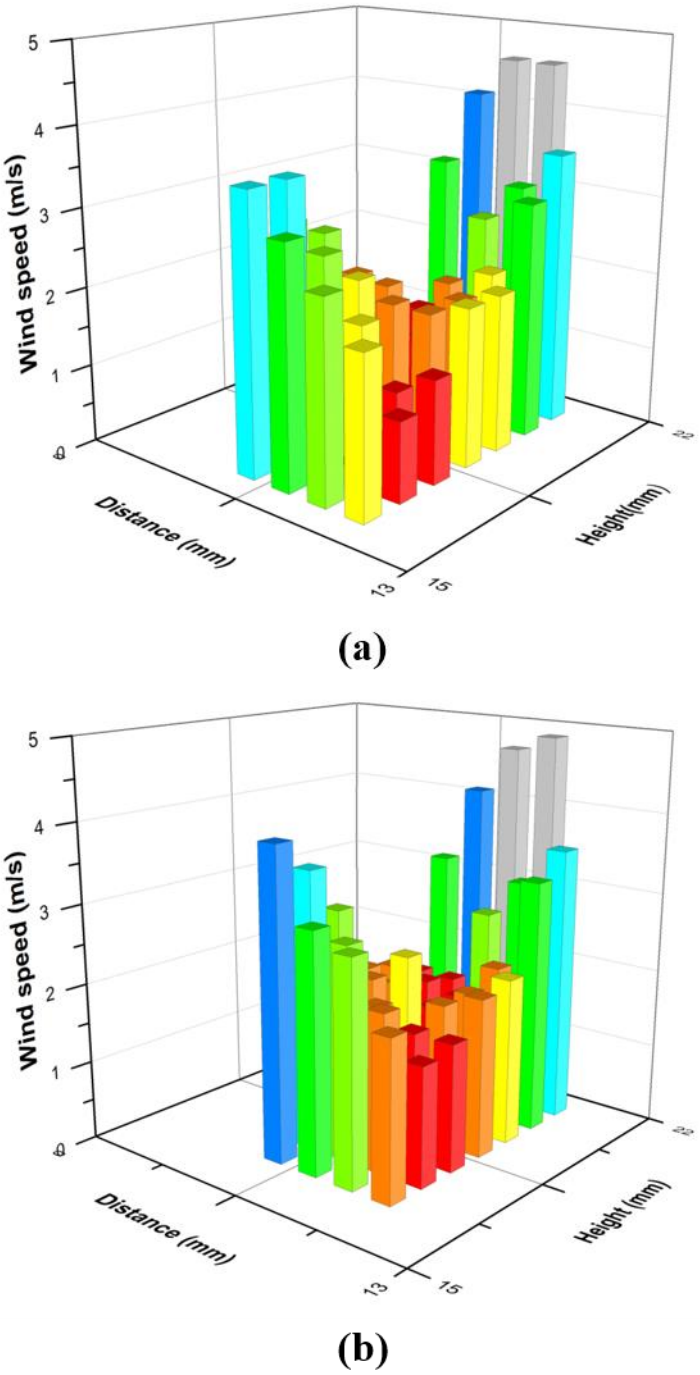

Figure 6.11: Threshold wind speeds with variable distances and heights of the bluff body for the (a) MTC generator and (b) MAC generator at the attack angle of 10°.

Four configurations were further investigated for performance of the harvester. They are distance of distance of 5 mm, height of 20 mm; distance of 7 mm, height of 19 mm; distance of 9 mm, height of 17 mm and distance of 11 mm, height of 16 mm respectively. The output

power with various bluff body positions was plotted in Figure 6.12 with the same attack angle of 10°. The maximum output power occurred with airspeed of 7 m/s from a bluff body configuration with distance of 11 mm and height of 16 mm. As with the piezoelectric generator, at distance of 5 mm, the power generations deceased with increasing wind speeds due to unstable performance at high wind speed.

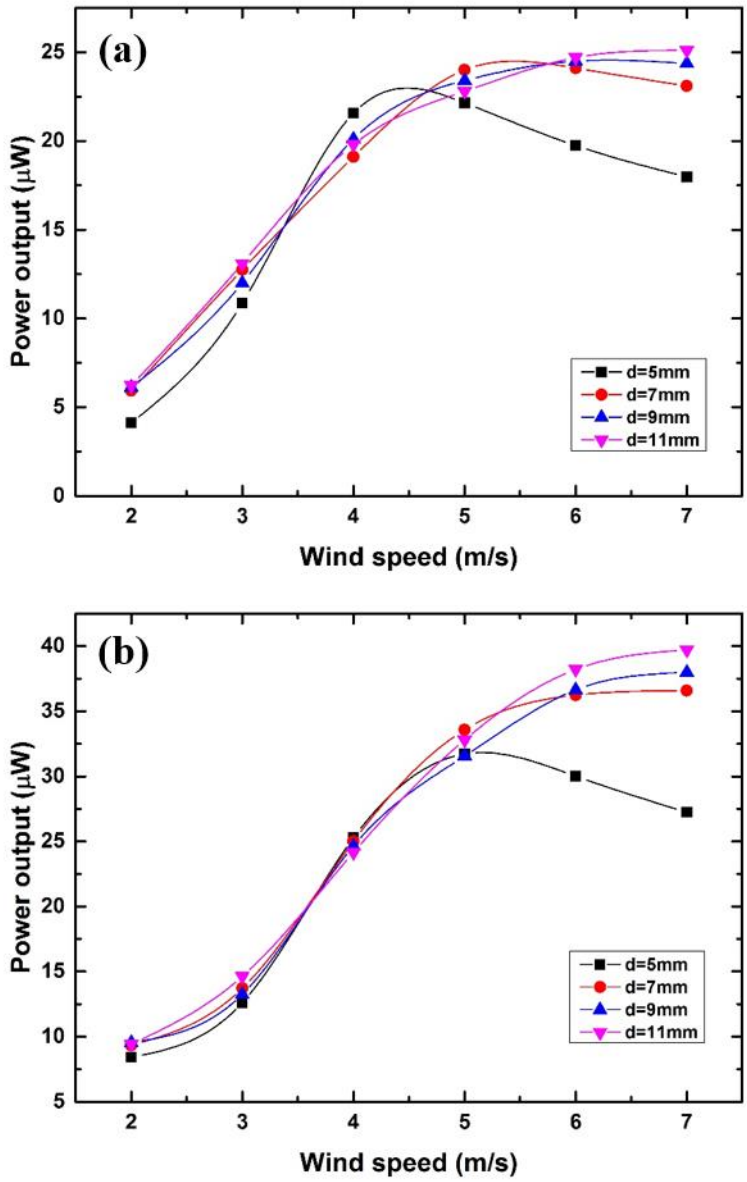

Figure 6.12: RMS Power versus wind speed for four configurations with (a) MTC generator and (b) MAC generator at the attack angle of 10° (lines plotted are used to indicate the trend).

6.2.3.4 Final Performance

The final designs were finished with optimum parameters (attack angle of 10°; distance of 11 mm; height of 16 mm; load values from Figure 6.9 and Figure 6.10) using the testing results and performances as shown in the following figures.

Figure 6.13(a) showed the optimum performance that could be achieved for the MTC generator in varying flow speed conditions. As can be seen from the graph, the harvester started operation from a wind speed of 1 m/s, and the maximum output power was 29.8 μW, which was achieved at a wind speed of 6 m/s. An output voltage curve with the RMS value of 293 mV (shown in Figure6.13 (b)) was obtained at the same wind speed.

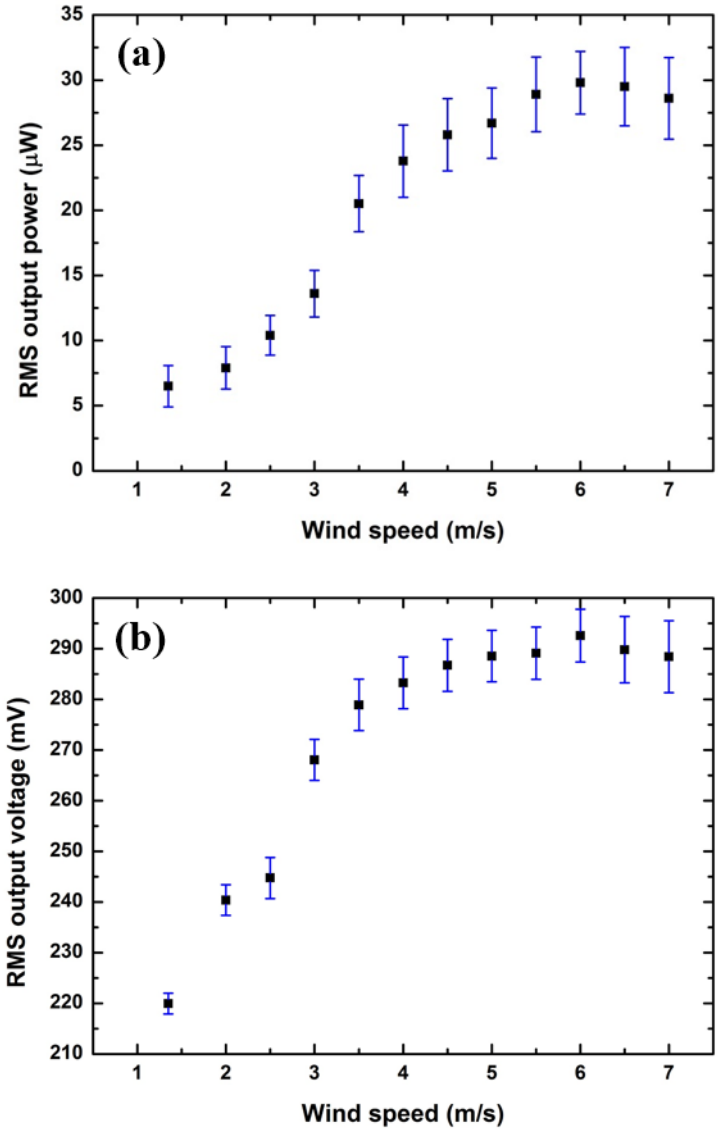

Figure 6.13: RMS output (a) power and (b) voltage in varying flow speed conditions with optimal configuration and load of the MTC generator fabricated in this work.

While for the MAC generator, the threshold wind speed for operation was 1.5 m/s, which was slightly higher than the MTC generator due to the extra mass of the attached magnets. However, the maximum power output was higher up to 41.2 μW as shown in Figure 6.14.

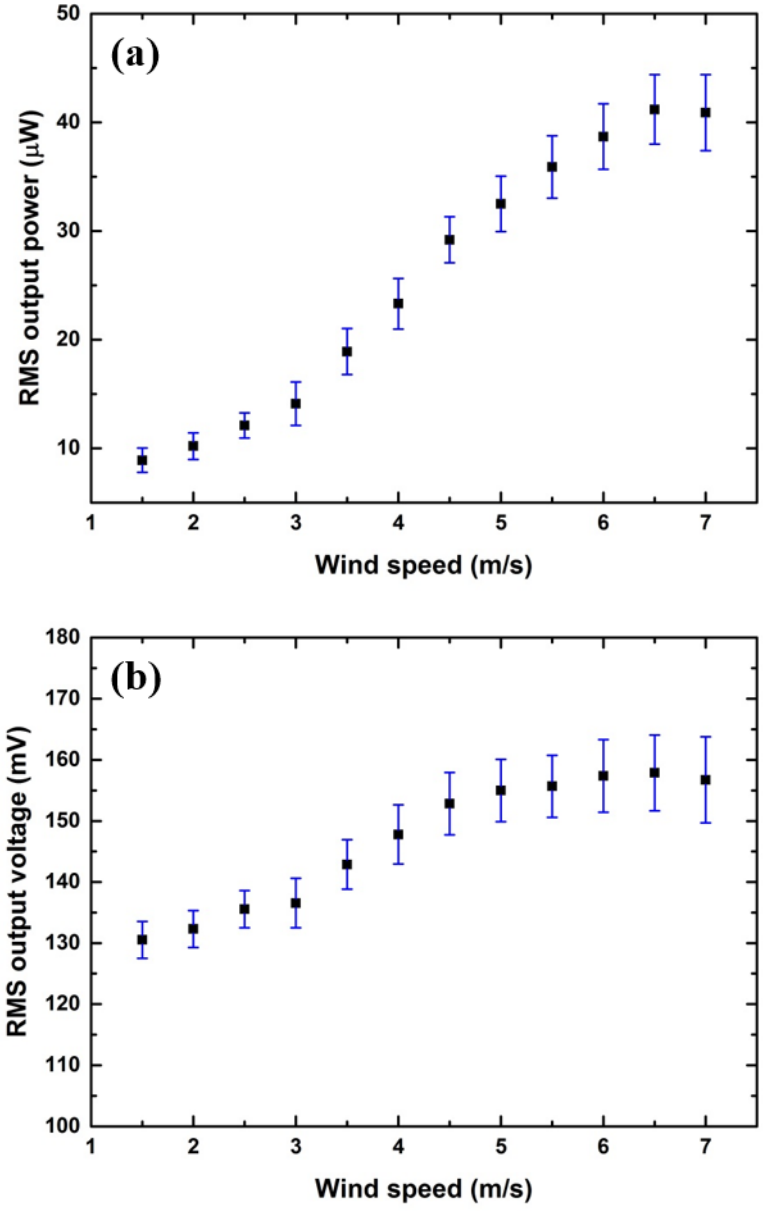

Figure 6.14: RMS output (a) power and (b) voltage in varying flow speed conditions with optimal configuration and load of the MAC generator fabricated in this work.

In addition, it can be observed that a working wind speed range from 1 m/s to 7 m/s was achieved by the MTC generator, and the wind speed range of the MAC generator was from 1.5 m/s to 7 m/s.

6.2.4. Comparison

6.2.4.1 Electromagnetic Coupling

As mentioned in previous section, the output power of the harvester depended on several parameters, and the electromagnetic coupling is always important. In order to achieve maximum power output, the electromagnetic coupling should be strong. However, fully coupled transducer may result in higher wind speed to start the operation. Therefore, the electromagnetic transducer should not be coupled too well in low air speed condition. And once the stable oscillation is maintained, the coupling can be strong with the optimum electrical load to extract maximum power output. As a result, an adjustable load is required for varying conditions.

6.2.4.2 Comparison with Piezoelectric generator

The optimum parameters of both piezoelectric generator and two electromagnetic generators were tabulated in Table 6.1:

Table 6.1: Comparison of the optimum parameters in the three devices fabricated in this work.

Parameters	The PE generator	The MTC generator	The MAC generator
Optimum attack angle	4˚-10˚	6˚-11˚	7˚-12˚
Optimum position of the bluff body	d=3-11 mm h=20-16 mm	d=5-11 mm h=20-16 mm	d=5-11 mm h=20-16 mm
Threshold wind speed	2 m/s	1.35 m/s	1.5 m/s

The attack angle of both piezoelectric and electromagnetic generator has the similar influence on threshold wind speed according to previous tests. The lowest threshold wind speeds only exist within a range of attack angles. However for different devices, these ranges are slightly different. As can be seen for Table 6.1, the optimum attack angles of the electromagnetic generators are larger than the piezoelectric one. This is because the cantilever initially bends downwards due to the mass of the magnets and the position of the wing was lower than that without magnets attached. In addition, when the attack angle is higher than a certain value (15˚ for instance), the threshold wind speed will increase dramatically. The optimum positions of the bluff body of these devices are similar as well except for the EM generator the distance has to be larger than 5 mm for the space of attached magnets and coils. During the final performance tests, the positions of the bluff body for all devices are the same, which are 11 mm in distance and 16 mm in height. This is because smaller distance of the bluff body causes

unstable oscillations at high wind speed thus results in lower power outputs. The piezoelectric generator has the highest threshold wind speed compare with the other two, due to added stiffness of the beam from the printed piezoelectric layers. All three generators can operate below 2 m/s of wind speed and operate throughout the entire range of flow speeds in HVAC ducts.

Table 6.2 summarises the electrical output performance between both systems through various comparison points. The power density is calculated dividing the maximum generated power by the volume of the device. And the power efficiency is defined as dividing the electric power output by the power of wind which can be calculated through Equation 3.8, where the windward area is defined as the sweeping area of the wing.

Table 6.2: Comparison of the performances in the three harvesters fabricated in this work.

Performance	The PE generator	The MTC generator	The MAC generator
Optimum load	800 kΩ	7.4 kΩ -2.6 kΩ	1.9 kΩ–0.6 kΩ
RMS maximum voltage	1.8 V	293 mV	158 mV
RMS maximum power	3.6 μW	29.8 μW	41.2 μW
Maximum power density	0.09	0.8	1.1
Efficiency	0.01%	0.5%	0.7%

The optimum loads of the piezoelectric generator and the electromagnetic generator that maximise the power output are not in the same range. For piezoelectric generator the value is 800 kΩ, but for electromagnetic devices, the optimised resistive load are several kΩ and the value decreases with increasing airflow speed. It should also be noticed that piezoelectric generators provided typically high peak voltage and low power from the airflow, while electromagnetic generators provided higher power with less available voltage. With similar threshold wind speed (1.5 m/s), the MAC generator has higher output power than the MTC one. Both MTC and MAC generators have higher power density and efficiency. The main issue of the piezoelectric generator is the small displacement of the active part as well as the limited value of the charge constant of screen printed PZT materials.

6.2.4.3 Comparison with other Devices

Figure 6.15 compares the performance of various airflow energy harvesters mentioned in the literature review and the generators presented in this thesis. As shown in Figure 6.15(a), both electromagnetic generator (MAC) and piezoelectric generators here had lower power outputs than other devices in the review part. The main reasons for this include most devices are designed for high wind speed operation and they have larger sizes compared with devices in this work. Figure 6.15(b) illustrates the power densities of these devices at different wind

speeds. As the output power is proportional to the cubic of the wind speed, this rough comparison focuses on the power density as power divided by the cubic of its corresponding wind speed and the volume of the main components (transducers and mechanical parts for vibration).

Although the generators presented in this work had lower power outputs than other devices due to the size constrain, the power densities comparison of these devices had different results. The EM generator in this report had the highest power density when it was operated at 1.5 m/s. However, the performance of the PE generator was not as well as the EM one. The main issue of the PE generator could be the added stiffness of the PZT part as well as the limited value of the charge constant of screen printed PZT materials. Moreover, both harvester presented here had low threshold wind speeds (1.5 m/s and 2 m/s respectively) compare with other devices in the review.

6.3 Conclusion

In this chapter, two prototypes of electromagnetic wind harvester with MTC and MAC designs were fabricated and tested. NdFeB magnet bars were selected as the moving parts for the transducers. The coils were wound by 60 μm thick copper wire with different designed dimensions.

A set of experiments in the air duct were carried out to investigate the performance of the harvesters. After testing, the results again showed relatively good correlation with the previous ones in Chapter 4. The optimized device for the MTC generator achieved a threshold wind speed of 1.35 m/s. The maximum output power was 29.8 μW, which was achieved at wind speed of 6 m/s. An output voltage with the RMS value of 293 mV was also obtained at the same wind speed. For the MAC generator, the threshold wind speed for operation was 1.5 m/s, which was slightly higher than the MTC generator. However, the maximum power output was higher (41 μW) as well. These performances together with the PE generator in Chapter 5 were compared via mechanical and electrical output performance. It is found that both the piezoelectric generator and the electromagnetic generator had similar optimum parameters in mechanical parts. The optimum attack angles and the position of bluff body are within the similar ranges. Particularly for best electrical output performance, the positions of the bluff body are all the same (11 mm in distance and 16 mm in height). The piezoelectric generator has the highest threshold wind speed compare with the other two. The MAC generator has a higher threshold wind speed than the MTC generator because of the larger mass of the magnets. All three generators can operate below 2 m/s of wind speed and operate throughout the entire range of flow speeds in HVAC ducts.

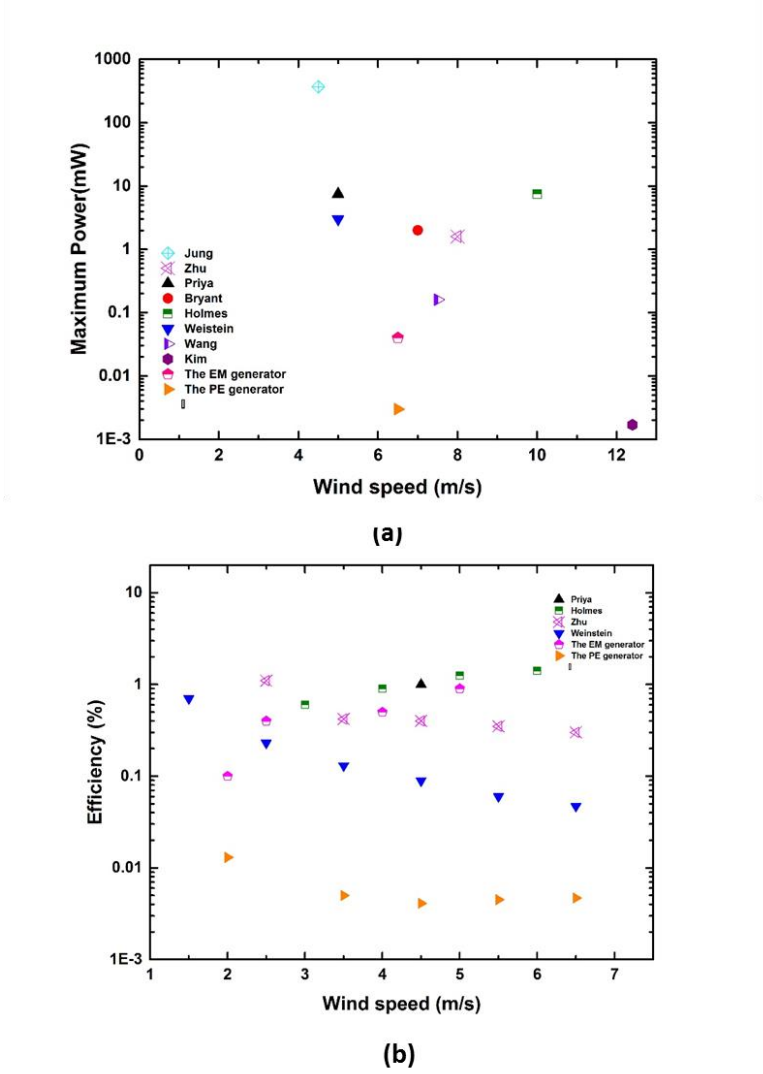

Figure 6.15: Comparison of (a) maximum power output, (b) efficiency between the airflow energy harvesters fabricated in this work and other reported works.

Figure 6.16: Comparison of (a) maximum power output, (b) efficiency between the airflow energy harvesters fabricated in this work and other reported works.

The electromagnetic generators have higher power output, as well as the efficiency than the piezoelectric one. However, the piezoelectric one has higher output voltage. In addition, the optimum loads of the piezoelectric generator and the electromagnetic generator that maximise the power output are not in the same range. For the electromagnetic generator, an adjustable load is needed for the EM generator. The EM transducer should not be coupled too well in low air speed condition to achieve a low threshold wind speed for operation. However, once the stable oscillation is maintained, the coupling should be strong enough to extract the maximum

power output. Therefore with varying conditions, the load should be adjustable for the optimum performance.

Performance of the generators was also compared with various airflow energy harvesters mentioned in the literature review. It is shown that the generators presented in this work had higher power densities and lower threshold wind speeds than the other devices.

Chapter 7 Conclusion and Future Work

This thesis has presented the design, simulation, fabrication, measurement and performance of a miniature wind energy harvester for HVAC systems in the buildings. This final chapter will give a brief overview of the research presented in this thesis, address how this work contributes to field of wind energy harvesting and other applications, and then present some possibilities for future research.

7.1 Summary of Achievement

In Section 1.3, the objective of the research was to design, fabricate and characterise an airflow energy harvester which can effectively convert the energy of a uniform and steady flow into periodic motion of the solid structure. These have been achieved, and specifically the following technical areas have been investigated in detail:

- Modelling the mechanical structure of the harvester in ANSYS CFX.
- Development of piezoelectric generator fabrication processes.
- Characterising the performance of the harvester
- Maximisation on electrical output by optimising the structures

The main results and conclusion will be summarised in more detail.

7.2 Summary of Contributions

The major contributions of the research are mainly divided into three major parts; modelling and optimization, fabrication, characterisation and comparison.

7.2.1. Modelling and Comparison

The first part of the research was to investigate the performance of wind energy harvesters and the current state in this field. From the literature review in Chapter 2, as miniature wind turbine systems suffered from high threshold wind speed for operation and complicated fabrication process, most researchers put their emphasis on flow-induced harvesters. However, none of

these harvesters were designed for low wind speed operation. In this situation, a flow induced energy harvester with a flapping beam was proposed, which represented a novel opportunity that may achieve low threshold wind speed of operation as well as large amplitude.

After studying the working principle of the harvester, the mechanical structure can be optimised by designing the bluff body and aerofoil in a proper way to achieve a low threshold wind speed for operation. In order to assess the effect of the design parameters, simulation with finite element analysis software such as ANSYS is necessary. The investigation successfully employed CFX-ANSYS in constructing a model for examining the aeroelastic phenomena. The static model was 3-dimensional and encompassed the main components in the mechanical structure. The lift force applied on the aerofoil was used as a guide to determine the threshold wind speed. A major contribution of the model is estimating the optimum structures of the device to achieve a low threshold wind speed. A prototype of the harvester was also fabricated for experimental work. Both simulation and experimental results are compared and results show a similar range of optimum positions of the bluff body and the attack angle. Moreover, relations between the distance and the height of the bluff body have the same trend in the simulations and tests. These similar trends between the simulation and experimental results show good correlations, which validates the simulation model used in this study.

In Chapter 5, the modal analysis in ANSYS was also used to estimate performance of the piezoelectric generator. Simulations with different lengths and widths of the PZT layers were carried out to investigate the effect of the structure geometry to the resonant frequency and output power. In order to compare the simulation result with the experimental result, a prototype was fabricated and tested. It is found that estimated natural frequencies from the simulation results are higher than the experimental results. The reason could be the dimensions of the screen printed parts on the beam as well as the aerofoil are slightly different from the simulation parameters. Regarding to the power output, the testing values are much lower than the expectation values of simulation results. Especially with the 11 mm long PZT layer device, an output power of 0.86 μW was achieved, which was much lower than the simulation result (4.5 μW). The most likely explanation is the reduced displacement of the part of the cantilever that has the PZT element printed on it due to added stiffness to the beam. This assumption was then verified by measuring the displacements at different points on the beam with 11 mm long PZT layer. However, with the increasing length of the piezoelectric part of beam, the problem could be reduced.

7.2.2. Fabrication

In Chapter 5, a prototype of piezoelectric wind harvester was fabricated by normal thick-film

printing steps. The main materials for fabricating the piezoelectric devices are PZT paste, electrode paste, dielectrode paste and substrate. The PZT paste was based on PZT-5H by blending the power of different particle size. The components of PZT paste formulation were 72% of 2 μm particles, 18% of 0.8 μm particles and 10% of Lead borosilicate glass, which was used as the permanent binder. Two kind of electrode paste were used, which are Au (ESL 8884) for bottom electrode and Ag (DuPont5000) for top electrode. Four layers were designed and printed onto the substrate (302/304 stainless steel). The dielectric layers were printed to cover the substrate and dried at 125°C for 15 minutes. It was then fired with a peak temperature of 850°C. This layer was printed because the gold bottom electrode cannot be printed directly onto the stainless steel substrate. Two single bottom electrode layers of gold were added on both sides of the substrate using the same process. On the bottom electrode, the PZT layer was added consisting of two prints. The first layer was dried at 125°C for 15 minutes, and then a second layer was printed directly on top and dried. Finally, the top electrode layers were printed and dried at 125°C. This printing and curing sequence avoids firing the device at high temperature again thus minimise lead loss from the PZT.

7.2.3. Characterisation and Optimisation

7.2.3.1 PZT Material Characterisation

In Chapter 5, the characterisation results for the fabricated thick film piezoelectric samples are discussed. Two samples at different curing temperature; 850°C and 950°C were inspected under microscope. The micrographs showed that the piezoelectric sample fired at 950°C had cracks on the surface resulting in electrical shorting between the top and bottom electrodes. Therefore the higher firing temperature is not suitable for the PZT paste in this work.

Polarisation was the final fabrication step. The poling conditions including the temperature, time and electric field applied. The measurement results show that a series of samples polarized 150°C for 30 minutes have an average d_{33} of 25 pC/N, which is 62% of the value that after 120 minutes. And at 225°C the 30 minute values were 93% of 120 minutes values. These results verify that the value of d_{33} increases with both temperature and time of poling. However, beyond 225°C samples were found to be short circuit. It is also found that improved value of coefficient is achieved when the poling voltages are increased. Nevertheless the piezoelectric layer suffered electrical short circuits when it was polarised with electric field strength greater than 4 MV/m. When the polarisation temperature, time and field strength were 225°C, 30 minutes and 4 MV/m respectively, a maximum value of d_{33} of 92 pC/N was obtained.

7.2.3.2 Mechanical Characterisation

All devices were tested for their mechanical structure properties. The measurements were carried out both on the shaker and in the air duct to investigate the threshold wind speed and natural frequency of the harvester.

The threshold wind speed depends on several design parameters, and the attack angle and the position of bluff body are of significant importance. Experimental work was carried out by measuring the threshold wind speed at different attack angles and positions of the bluff body. Results show that for all devices, the lowest threshold wind speed can be achieved within a certain range of those two parameters. For pure mechanical structure, the optimum range of attack angle is 5° to 8° and for piezoelectric generator this range is 4° to 10°. Regarding to the electromagnetic generators, the optimum attack angles increase to $6^{\circ} - 11^{\circ}$ (MTC) and $7^{\circ} - 12^{\circ}$ (MAC) as the position of the aerofoil is lower than the piezoelectric one due to the bending of the cantilever caused by attached magnets. In addition, during all tests, it is found that when the attack angle is higher than a certain value, the threshold wind speed of the harvester increases dramatically. The optimum positions of the bluff body of these devices are similar. The experimental results verify that with distance from 3 mm – 11 mm and height from 16 to 20 mm, the threshold wind speeds are the lowest. However, for the electromagnetic generator the distance has to be larger than 5 mm for the space of attached magnets and coils. Other parameters were also tested to investigate the influence on the threshold wind speed. Adding weights of proof mass and increasing the length of PZT layer both increase the threshold wind speed. Final testes show that all three generators can operate below 2 m/s of wind speed.

Natural frequencies of different cantilevers were tested on the shaker table. It is found that adding proof mass can effectively reduce the natural frequency. For piezoelectric generator, the resonant frequency decreases from 55 Hz to 16.5 Hz with added proof mass. For the electromagnetic generator, magnets are used as the proof mass and the natural frequency of the cantilever are reduced from 12.8 Hz to 7.3 Hz. The length of PZT layer also has influence on the natural frequency of the cantilever. Results show that with PZT lengths varying from 11 mm to 16 mm, the natural frequencies increase from 15 Hz to 20 Hz.

7.2.3.3 Electrical Characterisation

The electrical properties were tested through voltage and power output as well as the optimum resistive load of the harvesters. In Chapter 5, the maximum output power of the generator occurred at 7 m/s wind speed from a configuration with distance of 11 mm and height of 16 mm. Different lengths of the PZT layer were also investigated and results showed that with a

shorter length of PZT materials, the output power was small because of the added stiffness of the beam from printed PZT parts. As a result, PZT layer with length of 16 mm has much higher power output than that with length of 11 mm. After testing, the optimized device achieved the RMS power output ranging from 0.35 μW to 3.6 μW and the open-circuit output voltage from 0.6 V to 1.9 V.

In Chapter 6, the maximum output power of both MTC and MAC generators were achieved from a configuration with distance of 11 mm and height of 16 mm, which is the same as the piezoelectric one. For the MTC generator, the maximum output power was 27.2 μW with an output voltage of 293 mV. For the MAC generator, the maximum power output was 41 μW and the voltage was 158 mV. During the tests, it can also be observed that at distance smaller than 5 mm, performance of all devices at high wind speed was not stable, which resulted in a lower power output.

The optimum loads of the piezoelectric generator and the electromagnetic generator that maximise the power output are not in the same range. In Chapter 5, at different levels of wind speed, the ideal value of the optimum load was not as clearly defined; however, results followed a similar trend. The power output at the chosen resistance of 800 kΩ was comparable to maximum power for all test cases, and was thus determined to be the optimum resistive load for the piezoelectric generator. But for electromagnetic devices, the optimised resistive loads are not as clear as the piezoelectric one. It is found that, the optimised resistive load decreases with increasing airflow speeds. The reason is when the airflow is strong; the force acting on the aerofoil to overcome total damping became larger, resulting in larger energy extraction. Considering this situation, an adjustable load is required for the electromagnetic generator at varying conditions.

7.3 Recommendations for Future work

The experimental results presented in this thesis show that the harvester can effectively convert wind energy into large amplitude mechanical vibration without strict frequency matching constraints and can be used as a useful wind energy harvester in the HVAC systems. However, there is still room for improvement and other applications for powering many sensors in air ducts are worth exploring.

The wind harvester in this report was based on a flapping beam with a bluff body to induce the oscillation. Hence, for more accurate dynamic aeroelasticity analysis, a theoretical aeroelastic model should be presented and investigated the operation conditions for energy harvesting.

The PZT material used for the piezoelectric generator in this thesis has a charge constant (d_{33}) value of 92 pC/N, which is normal for screen printed PZT layers. However increasing the charge constant of the PZT material can further improve the electrical output. This can be achieved by using a high piezoelectric activity material.

This thesis put an emphasis on investigating the structure of wind harvester. However, in practical application, a power conditioning and storage circuit is needed, which should be the study of future work. A super capacitor can be used for energy storage and an electronic circuit with rectifier and microcontroller can be used for power management. The control system should also be able to detect the output voltage and adjust the electrical load accordingly.

.

Appendix A

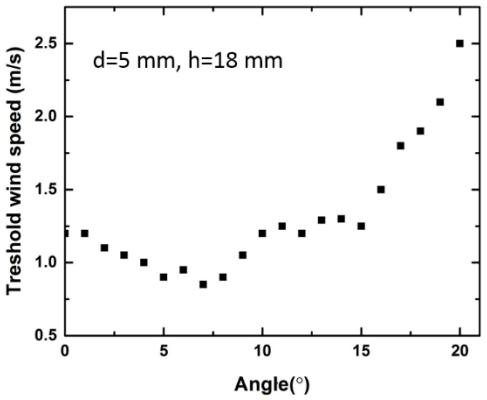
d=5 mm, h=18 mm
Treshold wind speed (m/s)
Angle(°)

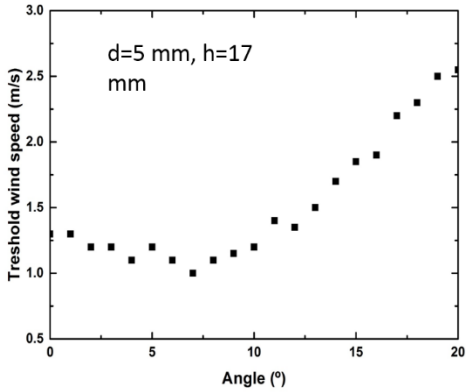
d=5 mm, h=17 mm
Treshold wind speed (m/s)
Angle (°)

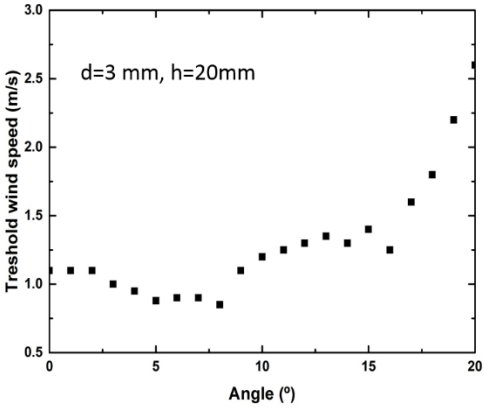
d=3 mm, h=20mm
Treshold wind speed (m/s)
Angle (°)

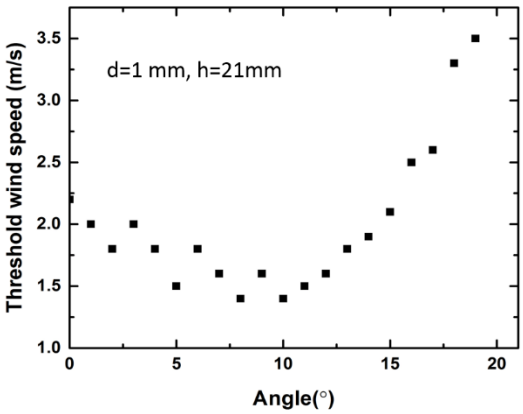
d=1 mm, h=21mm
Threshold wind speed (m/s)
Angle(°)

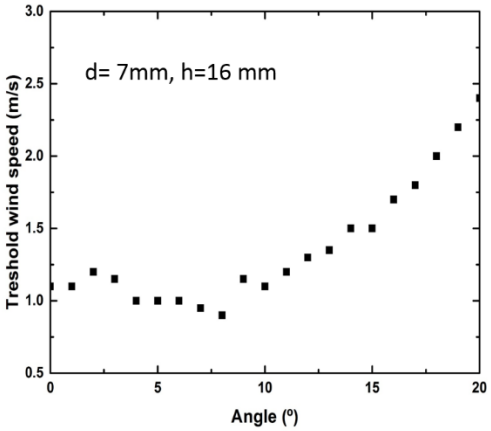
d= 7mm, h=16 mm
Treshold wind speed (m/s)
Angle (°)

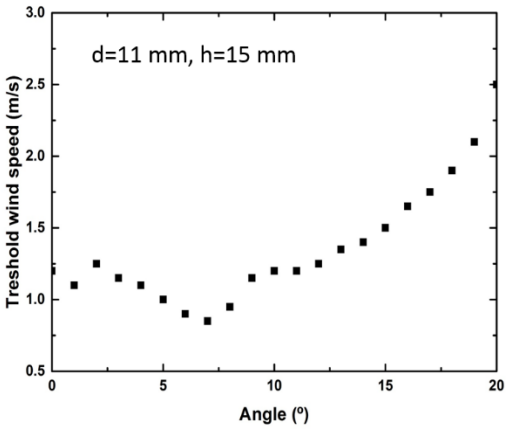
d=11 mm, h=15 mm
Treshold wind speed (m/s)
Angle (°)

Appendix B

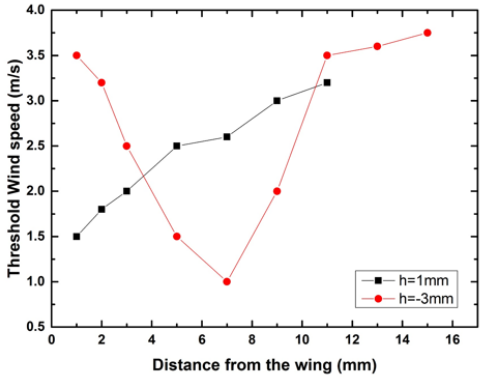

angle = 0°

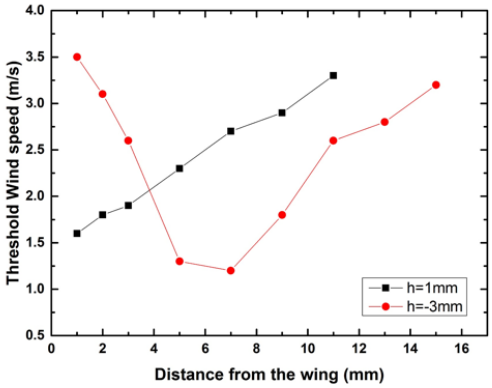

angle = 10°

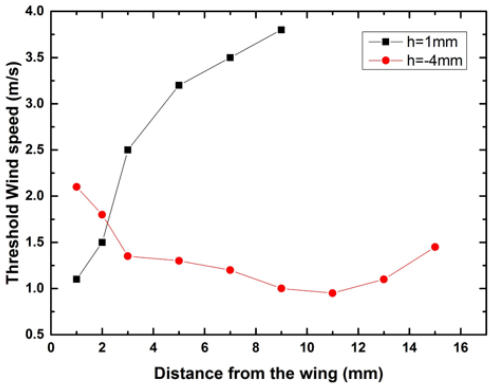

angle = 5°

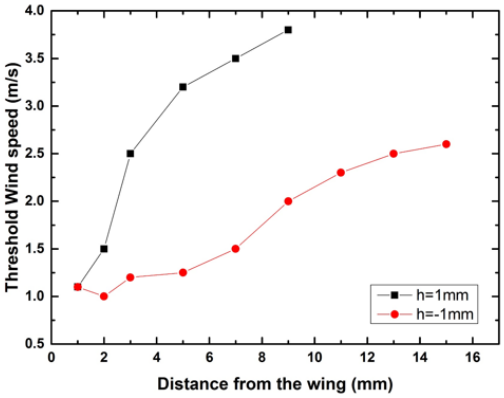

angle = 5°

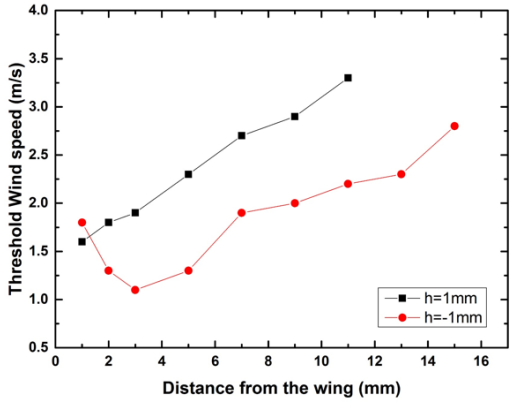

angle = 10°

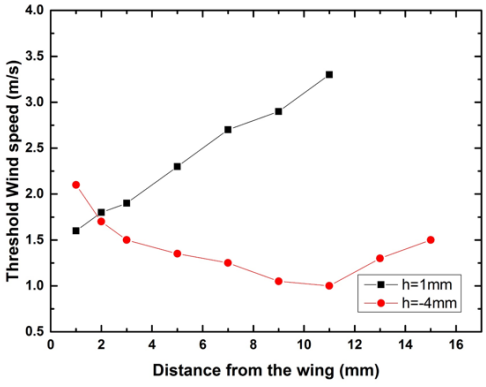

angle = 10°

Appendix C

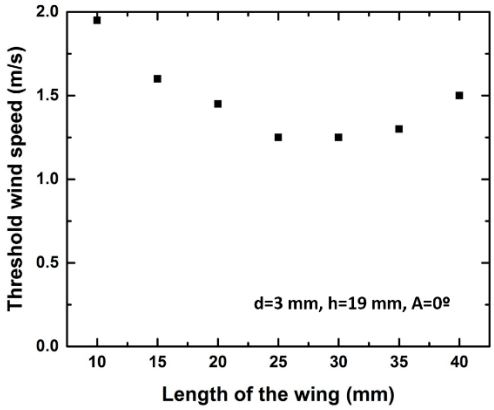
Threshold wind speed (m/s)
Length of the wing (mm)
d=3 mm, h=19 mm, A=0º

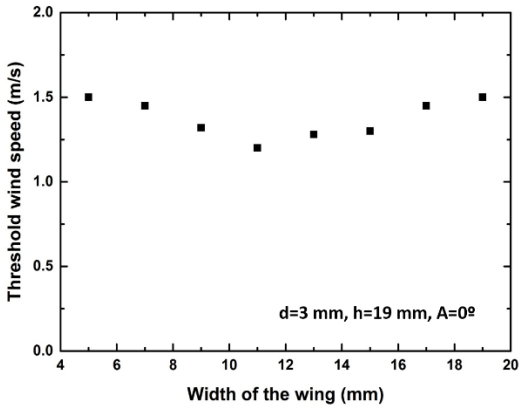
Threshold wind speed (m/s)
Width of the wing (mm)
d=3 mm, h=19 mm, A=0º

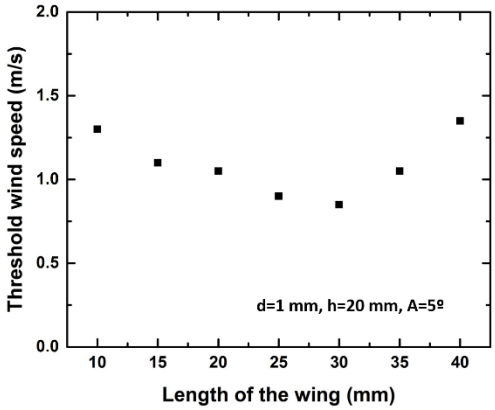
Threshold wind speed (m/s)
Length of the wing (mm)
d=1 mm, h=20 mm, A=5º

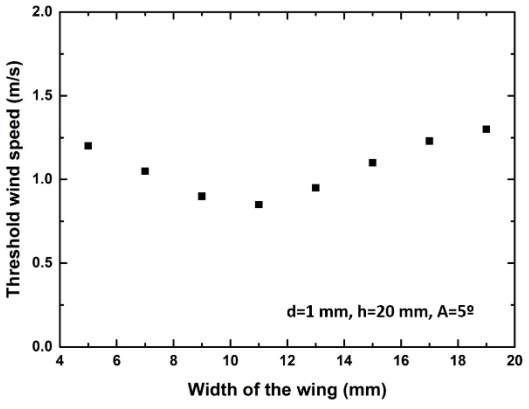
Threshold wind speed (m/s)
Width of the wing (mm)
d=1 mm, h=20 mm, A=5º

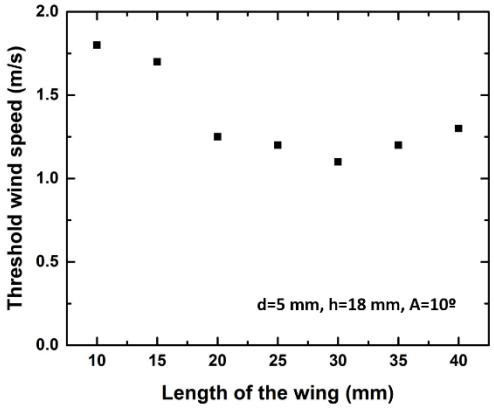
Threshold wind speed (m/s)
Length of the wing (mm)
d=5 mm, h=18 mm, A=10º

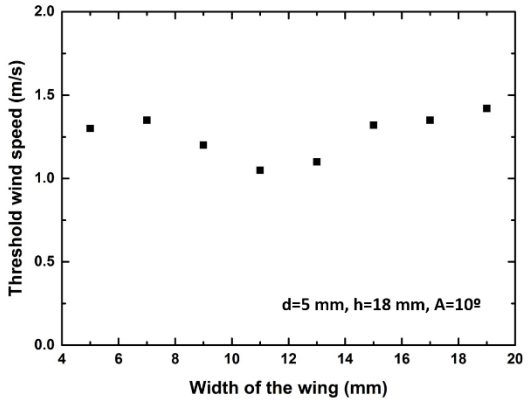
Threshold wind speed (m/s)
Width of the wing (mm)
d=5 mm, h=18 mm, A=10º

Appendix D

The ANSYS model for piezoelectric cantilever analysis.

```
/prep7
ts = 80e-6          ! substrate thickness      (microns)
tpzt = 100e-6             ! pzt thickness            (microns)
te = 10e-6          ! electrode thickness      (microns)
td = 20e-6          ! dielectric thickness     (microns)
tt = 3e-3           ! mass thickness     (microns)
ttl= 2e-4
!---

l = 10e-3           ! beamlength         (mm)
w1 = 5e-3           ! beam width         (mm)
w2= 0.25e-3
w3= 4.75e-3
w4= 0.75e-3
w5= 4.25e-3
g = 20e-3
lc = 5e-3           ! clamping area

!--- mass

l1 = 5e-3           ! l1   length of wing      (mm)
w10 = 10e-3         ! w1   wide of wing  (mm)

!---

t1 = ts/2
t2 = t1+td
t3 = t2+te
t4 = t3+tpzt
t5 = t4+te
t6 = t2+tt


! MODEL COORDINATES
```

```
k ,1,0,0,-t1                ! keypoint 1
k ,2,w1,0,-t1               ! keypoint 2
k ,3,w2,l,-t1               ! keypoint 3
k ,4,w3,l,-t1               ! keypoint 4
k ,5,w4,l+g,-t1                   ! keypoint 5
k ,6,w5,l+g,-t1                   ! keypoint 6
k ,7,-w10,l+g+l1,-t1        ! keypoint 7
k ,8,w1+w10,l+g+l1,-t1            ! keypoint 8
k ,9,w1+w10,l+g,-t1         ! keypoint 9
k ,10,-w10,l+g,-t1          ! keypoint 10

k ,11,0,-lc,-t1                   ! keypoint 1
k ,12,w1,-lc,-t1                  ! keypoint 2


kgen,  2,1,12,,,,ts,500                   ! substrate

kgen,  2,1,12,,,,-td,100                  ! dielectric(b)

kgen,  2,101,104,,,,-te,100         ! electrode1(b)
kgen,  2,201,204,,,,-tpzt,100             ! pzt(b)
kgen,  2,301,304,,,,-te,100         ! electrode1(u)

kgen,  2,501,512,,,,td,100          ! dielectric(u)

kgen,  2,601,604,,,,te,100          ! electrode2(b)
kgen,  2,701,704,,,,tpzt,100        ! pzt(u)
kgen,  2,801,804,,,,te,100          ! electrode2(u)

kgen,  2,107,110,,,,-tt,50          ! mass(b)
kgen,  2,607,610,,,,ttl,50          ! mass(u)

!------------------------

!-- substrate

v ,11,12,6,5,511,512,506,505              ! volume 1
```

```
v ,7,8,9,10,507,508,509,510        ! volume 2

!-- dielectric(b)
v ,11,12,4,3,111,112,104,103              ! volume 3
!v ,7,8,9,10,107,108,109,110              ! volume 4

!-- dielectric(u)
v ,611,612,604,603,511,512,504,503! volume 5


!-- dielectric(u)

!v ,607,608,609,610,507,508,509,510       ! volume 6

!-- mass(b)
!v ,7,8,9,10,157,158,159,160              ! volume 7

!-- mass(u)
!v ,607,608,609,610,657,658,659,660       ! volume 8


!-- electrode1(b)
v ,101,102,104,103,201,202,204,203! volume 9

!-- electrode2(b)
v ,301,302,304,303,401,402,404,403! volume 10

!-- electrode1(u)
v ,601,602,604,603,701,702,704,703 ! volume 11

!-- electrode2(u)
v ,801,802,804,803,901,902,904,903! volume 12

!-- pzt(b)
v ,201,202,204,203,301,302,304,303! volume 13

!-- pzt(u)
v ,701,702,704,703,801,802,804,803! volume 14
```

```
! substrate
!vadd,1,2                          ! volume 15

!-- dielectric(b)
!vadd,3,4                          ! volume 1

!-- dielectric(u)
!vadd,5,6                          ! volume 2

!beam - material - stainless steel
mat, 1              ! material number 1
ET, 1, 45           ! type of material used "solid45"


MP, DENS, 1, 7750   ! density of stainless steel
MP, NUXY, 1, 0.26   ! poissons ratio for stainless steel
MP, ex, 1, 180e9    ! youngs modulus for stainless steel


!dielectric - material 2 - glass dielectric pyrex

mat, 2              ! material number 2
ET, 2, 45           ! type of material used "solid45"

MP, DENS, 2, 2230   ! density of glass dielectric pyrex
MP, NUXY, 2, 0.2    ! poissons ratio for glass dielectric pyrex
MP, ex, 2, 64e9           ! youngs modulus for glass dielectric pyrex

!electriode - material 3 - gold

mat, 3              ! material number 3
ET, 3, 45           ! type of material used "solid45"

MP, DENS, 3, 19280  ! density of gold
MP, NUXY, 3, 0.42   ! poissons ratio for gold
MP, ex, 3, 80e9           ! youngs modulus for gold
```

```
!mass - material - NdFeB

mat, 5              ! material number 5
ET, 5, 45           ! type of material used "solid45"

MP, DENS, 5, 130    ! density of N
MP, NUXY, 5, 0.24   ! poissons ratio for N
MP, ex, 5, 6e9      ! youngs modulus for N

mat, 6              ! material number 5
ET, 6, 45           ! type of material used "solid45"

MP, DENS, 5, 130    ! density of magnetic
MP, NUXY, 5, 0.35   ! poissons ratio for balsa wood
MP, ex, 5, 2.9e9    ! youngs modulus for balsa wood
!pzt - material - pzt

mat, 4              ! material number 4
ET, 4, 5            ! type of material used "solid5"

MP, DENS, 4, 5440   ! density of pzt
MP, NUXY, 4, 0.3    ! poissons ratio for pzt
!MP, DAMP, 4, 4.8e-6
!MP, ex, 4, 15e9           ! youngs modulus for pzt

!--------------------

!   - Material properties for Pzt +
!
/com   Stiffness
TB,    ANEL,  4,     1,     ,      0
TBDATA,       1,     1.2720E+11,   8.0212E+10,   8.4670E+10
TBDATA,       7,     1.2720E+11,   8.4670E+10
TBDATA,       12,    1.1744E+11
TBDATA,       16,    2.3496E+10
TBDATA,       19,    2.2989E+10
TBDATA,       21,    2.2989E+10
/com   Piezo
```

```
TB,     PIEZ,   4
TBDATA,         3,      -.5093
TBDATA,         6,      -.5093
TBDATA,         9,      2.1445
TBDATA,         14,     1.523
TBDATA,         16,     1.523
/com    Permittivity
EMUNIT,         EPZRO,  8.85E-12
MP,     PERX,   4,      1000
MP,     PERY,   4,      1000
MP,     PERZ,   4,      950


tblist,all                      ! List input and converted material matrices

! selecting materials

vsel ,s,volu,,1,2
vatt ,1,,1
vsel ,s,volu,,3,6
vatt ,2,,2
vsel ,s,volu,,7,8
vatt ,5,,5
vsel ,s,volu,,9,12
vatt ,3,,3
vsel ,s,volu,,13,14
vatt ,4,,4

vsel, all

! meshing
esize,5e-4
vmesh,all

! merge coincidences
!nummrg,all
!waves
```

```
! DEFINE MASTER DEGREES OF FREEDOM
!total ,100,1

! MERGE COINCIDENCES AND REDUCE WAVEFRONT

numm,all,1e-8
waves

! CLAMPING
nsel ,s,loc,y,-lc,0         ! selects all nodes on the y=0 axis
nsel ,r,loc,x,w1/2-2e-3,w1/2+2e-3        ! selects all nodes on the x axis
nsel ,a,loc,y,-2e-3,0
d ,all,UX,0                 ! clamps selected nodes, sets degrees of freedom
d ,all,UY,0
d ,all,UZ,0
nsel ,all                   ! reselects all the nodes in the model

! FORCE

!asel,,,,64
!nsla,,1
!f,all,fz,force/16

!asel ,all
!nsel ,all

! VIEW THE MODEL

/view ,1,1,1,1
/pbc ,all,1
eplot

finish

! STATIC ANALYSIS

/solu
antype,static
```

```
pstres,on
solve
fini

! MODAL ANALYSIS

/solu
antype ,modal
modopt ,LANB,2
pstres ,on
mxpand ,2
solve
*get,fr,mode,1,freq

/com, Resonant frequency fr = %fr% Hz
fini

! Display deformed shape

/post1
set, first
pldisp ,2
```

Reference

[1] M. Weiser, “The computer for the twenty-first century,” *Scientific American*, pp. 94–104, 1991.

[2] P. E. Ross, “Managing care through the air,” *IEEE Spectrum*, vol. 41, no. 12, pp. 14–19, 2004.

[3] Website, “Strain Energy Harvesting for Wireless Sensor Networks,”.

[4] Website, “I think, therefore I interact, new electronics on campus,”.

[5] L. Doherty, B. A. Warneke, B. E. Boser and K. S. J. Pister, “Energy and performance considerations for smart dust”, *International Journal of Parallel Distributed Systems and Networks*, vol. 4, no. 3, pp. 121–133, 2001.

[6] Website, “ORESTEIA project homepage”.

[7] F. Nack, “An overview on wireless sensor networks” *IPCSIT* vol.35. 2012

[8] Y. Liao and H. A. Sodano “Model of a single mode energy harvester and properties for optimal power generation” *Smart Material Structure,* vol.17,no. 6, pp.1–14,2008.

[9] W. Shockley “The theory of p-n junctions in semiconductors and p-n junction transistors,” *Bell System Technology Journal*, vol. 28, pp. 435–489, 1949.

[10] S. E. Thompson, M. Armstrong, C. Auth, M. Alavi, M. Buehler, R. Chau, S. Cea, T. Ghani, G. Glass, T. Hoffman, C. Jan, C. Kenyon, J. Klaus, K. Kuhn, Z. Ma, B. Mcintyre, K. Mistry, A. Murthy, B. Obradovic, R. Nagisetty, P. Nguyen, S. Sivakumar, R. Shaheed, L. Shifren, B. Tufts, S. T yagi, M. Bohr and Y. El-Mansy, “A 90nm logic technology featuring strained-silicon,” *IEEE Transactions on Electron Devices*, vol. 51, no. 11, pp. 1790–1797, 2004.

[11] C. Kompis, S. Aliwell, “Energy harvesting technologies to enable remote and wireless sensing” 2008

[12] ASHTON, K. “That ‘Internet of Things’ Thing. In the real world, things matter more than ideas”. RFID,2009

[13] James, E.P., Tudor, M.J., Beeby, S.P., Harris, N.R., Glynne-Jones, P., Ross, J.N. and White, N.M. “An investigation of self-powered systems for condition monitoring applications” *Sensors and Actuators A: Physical*, 110, (1-3), 171-176. 2004

[14] L. Mateu and F. Moll, “Review of energy harvesting techniques and applications for microelectronics,” *Proceedings of the SPIE Microtechnologies for the New Millennium*, pp. 359–373, 2005.

[15] A. Harb “Energy harvesting: state-of-the-art,” *Renewable Energy*, vol. 36, pp. 2641–2654, 2011.

[16] L. Perez-Lombard, J. Ortiz and C. Pout "A review on buildings energy consumption information," *Energy Build*, vol. 40, no. 3, pp. 394–398, 2008.

[17] Website "Flow velocity air ducts".

[18] G. Poulin "Comparative study of an electromagnetic and a piezoelectric system," *Sensors and Actuators A. Physical*, vol. 116, pp. 461–471, 2004.

[19] F. Blatt, P. Schroeder, C. Foiles and D. Greig "Thermoelectric power of materials," *New York: Plenum Press*, 1976.

[20] R. Myers, "The basics of physics," *Greenwood Press*, 2006.

[21] O. Mah, "Fundamentals of photovoltaic materials," *National Solar Power Research Institute, Inc.*, 1998.

[22] R. Elliot "Electromagnetics: history, theory, and applications," *Piscataway: IEEE Press*, 1993.

[23] K. Werner "Introduction to Microsystem Design," *Springer*, 2011.

[24] L. Kok, N. White and N. Harris "Fabrication and characterisation of free-standing thick-film piezoelectric cantilevers for energy harvesting." *Measurement Science & Technology*, vol. 20, no. 12, 2009.

[25] Website "Piezoelectric constants,".

[26] J. Oliver, "Modeling interdigitated piezoelectric thin-film micro-actuators," *ProQuest*, 2008.

[27] K. Lee "Polymers for photonics applications II," *Springer-Verlag Berlin Heidelberge*, 2003

[28] M. S. Vijaya "Piezoelectric Materials and Devices," *CRC Press*, 2013

[29] R. Torah, S. P. Beeby and N. M. White "An improved thick-film piezoelectric material by powder blending and enhanced processing parameters," *IEEE transactions on ultrasonics, ferroelectrics, and frequency control*, vol. 52, no. 1, pp. 10–16, 2005.

[30] L. Kok, L. Swee, N. White and N. Harris "Design, fabrication and characterisation of free-standing thick-film piezoelectric cantilevers for energy harvesting," *Measurement Science & Technology*, vol. 20, no. 12, 2009.

[31] S., Gevorgian "Ferroelectrics in microwave devices, circuits and systems," *Springer–Verlag London Limited*, 2009.

[32] S. P. Beeby "MEMS Mechanical Sensors," *Artech House Publishers*, 2004.

[33] A. Nechibvute, A. Chawanda and P. Luhanga "Piezoelectric energy harvesting devices: An alternative energy source for wireless sensors," *Smart Materials Research,* 2012.

[34] H. A. Sodano, D. J. Inman and G. Park "Comparison of piezoelectric energy harvesting devices for recharging batteries," *Journal of Intelligent Material Systems and Structures*, vol. 16, no. 10, pp, 799–807, 2005

[35] C. S. Lee, J. Joo, S. Han, J. H. Lee and S. K. Koh "Poly (vinylidene fluoride) transducers with highly conducting poly (3, 4-ethylenedioxythiophene) electrodes," *Synthetic Metals*, vol. 152, pp 49–52, 2005.

[36] J. Rastegar, C. Pereira and H. L. Nguyen "Piezoelectric-based power sources for harvesting energy from platforms with low frequency vibration," *Proceeding SPIE 6171*, pp. 617101, 2006.

[37] S. R. Platt, S. Farritor and H. Haider "The use of piezoelectric ceramics for electric power generation within orthopaedic implants," *IEEE/ASME Transactions on Mechatronics*, vol. 104, pp. 55–61, 2006.

[38] W. J. Choi, Y. Jeon, J. H. Jeong, R. Sood and S. G. Kim "Energy harvesting MEMS device based on thin film piezoelectric cantilevers," *Journal of Electroceramics*, vol. 17, no. 2–4, pp. 543–548, 2006.

[39] D. Zhu, G. Peter, N. White, N. Harris, R. Torah, A. Almusallam, and S. Beeby, "Screen printed piezoelectric films for energy harvesting." *Advances in Applied Ceramics*, 112, (2), 79-84. 2013

[40] S. P. Beeby and T. J. Kazmierski "Energy Harvesting Systems," *Springer*, 2011.

[41] N. N. H. Ching, G. M. H. Chan, W. J. Li, H. Y. Wong and P. H. W. Leong "PCB integrated micro generator for wireless systems," *International Symposium on Smart Structures and Microsystems*, 2000.

[42] R. Amirtharajah and A. Chandrakasan "Self-powered signal processing using vibration-based power generation," *IEEE Solid-State Circuits*, vol 33, no 5, pp. 687–695, 1998.

[43] C. Williams, C. Shearwood, M. Harradine, P. Mellor, T. Birch and R. Yates "Development of an electro-magnetic micro-generator," *IEEE Proceeding G-Circuits, Devices and Systems*, vol. 148, pp. 337–342, 2001.

[44] W. Li, T. Ho, G. Chan, P. Leong and H. Y. Wong "Infrared signal transmission by a laser-micromachined, vibration-induced power generator," *IEEE Midwest Symposium on Circuits and Systems*, vol. 1, pp. 236–239, 2000.

[45] D. Zhu , S. Beeby, J. Tudor and N. Harris "Vibration energy harvesting using the Halbach array" *Smart Mater. Struct.* 21 075020 (11pp), 2012.

[46] D. Zhu , S. Beeby, J. Tudor and N. Harris "Increasing output power of electromagnetic vibration energy harvesters using improved Halbach arrays" *Sensors and Actuators A Physical*,203,pp11-19.2013.

[47] R. G. Herb, D. B. Parkinson and D. W. Kerst "The development and performance of an electrostatic generator operating under high air pressure," Physical Review, vol. 51, pp. 75–83, 1937

[48] P. D. Mitcheson, P. Miao, B. H. Stark, E. M. Yeatman, A. S. Holmes and T. C. Green "MEMS electrostatic micro-power generator for low frequency operation," *Sensors Actuators A*, vol. 115, pp. 523–529, 2004.

[49] J. F. Walker, N. Jenkins "Wind energy technology," *John Wiley & Sons*, 1997.

[50] T. Ackermann and L. Soder "An overview of wind energy-status." *Renewable and Sustainable Energy Reviews*, vol. 6, pp. 67–128, 2002.

[51] G. M. Herbert, S. Iniyan, E. Sreevalsan and S. Rajapamdian "A review of wind energy technologies," *Renewable and Sustainable Energy Reviews*, vol. 11, pp.1117–1145, 2007.

[52] H. Wu, X. Wang and Y. Hu "Development of small wind generator based on hybrid magnetic bearing," *Proceedings Asia-Pacific Power and Energy Engineering Conference*, pp. 27–31, 2009.

[53] S. Liu, Z. Bian, D. Li and W. Zhao "A magnetic suspended self-pitch vertical axis wind generator," *Proceedings Asia-Pacific Power and Energy Engineering Conference*, pp. 28–31, 2010.

[54] A. Flammini, D. Marioli and M. Serpelloni "An autonomous sensor with energy harvesting capability for airflow speed measurements," *IEEE Transactions on Instrumentation and Measurement*, vol. 60, no. 5, pp. 892–897, 2011.

[55] G. Shrestha, H. Polinder and J. A. Ferreira "Scaling laws for direct drive generators in wind turbines," *IEEE International Electric Machines and Drives Conference Proceedings*, pp 797–803, 2009.

[56] H. Hirahara, M. Z. Hossain, M. Kawahashi and Y. Nonomura "Testing basic performance of a very small wind turbine designed for multi-purposes," *Renewable Energy*, vol. 30, pp. 1279–1297, 2005.

[57] A. Vardar and I. Alibas "Research on wind turbine rotor models using NACA profiles," *Renewable Energy*, vol.33, pp. 1721–1732, 2008.

[58] D. Rancourt, A. Tabesh and L. G. Fréchette "Evaluation of centimeter-scale micro wind mills: Aerodynamics and electromagnetic power generation" *Proceedings Power MEMS*, pp. 93–96, 2007.

[59] A. S. Holmes, G. Hong, K. R. Pullen and K. R. Buffard "Axial-flow microturbine with electromagnetic generator: design, CFD simulation and prototype demonstration," *Proceedings Power MEMS*, pp. 568–571, 2004.

[60] A. Bansal, D. A. Howey and A. S. Holmes "cm-Scale air turbine and generator for energy harvesting from low-speed flows", *IEEE Transducers*, pp. 529–532, 2009.

[61] A. Bansal, D. A. Howey and A.S. Holmes "Design and performance of a centimetre-scale shrouded wind turbine for energy harvesting," *Smart Materials and Structures*, vol. 20, pp.1–12, 2011.

[62] D. Carli, D. Brunelli, D. Bertozzi and L. Benini "A high-efficiency wind-flow energy harvester using micro turbine," *International Symposium on Power Electronics, Electrical Drives, Automation and Motion*, 2010.

[63] F. J. Xu, F. G. Yuan, J. Z. Hu and Y. P. Qiu "Design of a miniature wind turbine for powering wireless sensors," *Proceedings of SPIE*, vol. 7647, pp. 764741–764741, 2010.

[64] P. H. Chen and S. C. Lin "Wind-powered piezo generators," *IEEE Industrial Electronics Society*, pp. 2163–2168, 2007.

[65] S. Priya, C. T. Chen, D. Fye and J Zahnd "Piezoelectric windmill: a novel solution to remote sensing," *Japanese Journal of Applied Physics*, vol. 44, no. 3, pp. 104–107, 2005.

[66] S. Priya "Modeling of electric energy harvesting using piezoelectric windmill," *Applied Physics Letters*, vol.87, pp. 184101–3, 2005.

[67] R. Myers, M. Vickers, H. Kim and S. Priy "Small scale windmill,", *Applied Physics Letters*, vol. 90, pp. 054106, 2007.

[68] S. Bressers, D. Avirovik, M. Lallart, D. Inman, and S. Priya, "Contact-less wind turbine utilizing piezoelectric bimorphs with magnetic actuation," *Structural Dynamics*, vol. 3, pp. 233–243, 2011.

[69] H. Jung, and S. Lee, "The experimental validation of a new energy harvesting system based on the wake galloping phenomenon," *Smart Material Structure*, vol. 20, pp. 055022, 2011.

[70] M. Sanchez-Sanz, B. Fernandez and A. Velazquez "Energy-harvesting microresonator based on the forces generated by the Karman street around a rectangular prism," *Journal of Microelectromechanical Systems*, vol. 18, no. 2, pp. 449–457, 2009.

[71] V. Sivadas and A. M. Wickenheiser "A study of several vortex-induced vibration techniques for piezoelectric wind energy harvesting," *Proceedings SPIE*, vol. 7977, pp. 79770F, 2011.

[72] M. M. Bernitsas, K. Raghavan, Y. Ben-Simon and E. M. H. Garcia "VIVACE : A new concept in generation of clean and renewable energy from fluid flow," *Journal of Offshore Mechanics and Arctic Engineering*, vol. 130, no. 4, pp. 041101, 2008.

[73] A. Barrero-Gil, S. Pindado and S. Avila "Extracting energy from vortex-induced vibrations: a parametric study," *Applied mathematical modelling*, vol. 36, no. 7, pp. 3153-3160, 2012.

[74] J. J. Allen and A. J. Smits "Energy harvesting eel," *Journal of Fluids and Structures*, vol. 15, pp. 629-640, 2001

[75] G. W. Taylor, J. R. Burns, S. M. Kammann, W. B. Powers and T. R. Welsh "The energy harvesting eel: a small subsurface ocean/river power generator," *IEEE Journal of Oceanic Engineering*, vol. 26, no. 4, pp. 539-547, 2001.

[76] S. R. Anton and H. A. Sodano "A review of power harvesting using piezoelectric materials," *Smart Materials and Structures*, vol. 16, no. 3, pp. R1, 2007.

[77] S. Jiang, X. Li, S. Guo, Y. Hu, J. Yang and Q. Jiang "Performance of a piezoelectric bimorph for scavenging vibration energy," *Smart Materials and Structures*, vol. 14, no. 4, pp. 769, 2007.

[78] D. A. Wang and N. Z. Liu "A shear mode piezoelectric energy harvester based on a pressurized water flow," *Sensors and Actuators A: Physics*, vol. 167, no. 2, pp. 449-458, 2011.

[79] S. Li and H. Lipson "Vertical-stalk flapping-leaf generator for wind energy harvesting," Proceedings of the ASME 2009 Conference on Smart Materials, Adaptive Structures and Intelligent Systems, 2009.

[80] S. Li, J. Yuan and H. Lipson "Ambient wind energy harvesting using cross-flow fluttering," Journal of Applied Physics, vol.109, pp. 026104, 2011.

[81] S. D. Kwon "A t-shaped piezoelectric cantilever for fluid energy harvesting," Applied Physics Letters, vol. 97, no. 16, pp. 164102, 2010.

[82] J. A. Dunnmon, S. C. Stanton, B. P. Mann and E. H. Dowell "Power extraction from aeroelastic limit cycle oscillations," *Journal of Fluids and Structures*, vol. 27, no. 8, pp. 1182-1198, 2011.

[83] Q. Wen, R. Schulze, D. Billep, T. Otto and T. Gessner "Modeling and optimization of a vortex induced vibration fluid kinetic energy harvester," *Procedia Engineering*, vol. 87, pp. 779-782, 2014.

[84] M. Demori, M. Ferrari, V. Ferrari, S. Farise and P. Poesio "Energy harvesting from von karman vortices in airflow for autonomous sensors," *Procedia Engineering*, vol. 87, pp. 775-778, 2014.

[85] L. A. Weinstein, M. R. Cacan, P. M. So and P. K. Wright "Vortex shedding induced energy harvesting from piezoelectric materials in heating, ventilation and air conditioning flows," Smart Materrial Structures, vol. 21, pp. 045003, 2012

[86] P. W. Bearman and A. J. Wadcock "The interaction between a pair of circular cylinders normal to a stream," *Journal of Fluid Mechanics*, vol. 61, pp. 499-511, 1973.

[87] H. J. Jung, S. W. Lee and D. Jang "Feasibility study on a new energy harvesting electromagnetic device using aerodynamic instability," *IEEE Transactions on Magnetics*, vol. 45, no. 10, pp. 4376–4379, 2009.

[88] H. Jung and S. Lee "The experimental validation of a new energy harvesting system based on the wake galloping phenomenon," *Smart Materials and Structures*, vol. 20, pp. 055022, 2011.

[89] J. W. Duncan "The fundamentals of flutter," *Aircraft Engineering and Aerospace Technology*, vol. 17, no, 1, pp.16-20, 1945.

[90] W. Mckinney and J. DeLaurier "The wing mill: an oscillating-wing windmill," *Journal of Energy*, vol. 5, no. 2, pp.109–115, 1981.

[91] K. D. Jones and M. F. Platzer "Numerical computation of flapping-wing propulsion and power extraction," *35th Aerospace Sciences Meeting and Exhibit, Aerospace Sciences Meetings*, pp. 97-0826, 1997.

[92] K. Isogai, M. Yamazaki, M. Matsubara and T. Asaoka "Design study of elastically supported flapping wing power generator," *Proceedings of International Forum on Aeroelasticity and Structural Dynamics,* 2003.

[93] A. Erturk, W. G. R. Vieira, C. De Marqui, Jr. and D. J. Inman "On the energy harvesting potential of piezoaeroelastic systems," *Applied Physics Letters*, vol. 96, pp. 184103, 2010.

[94] Q. Zhu, M. Haase and C. H. Wu, "Modelling the capacity of a novel flow-energy harvester," *Applied Mathematical Modelling*, vol. 33, pp. 2207–2217, 2009.

[95] S. D. Kwon, "A t-shaped piezoelectric cantilever for fluid energy harvesting," *Applied Physics Letters*, vol. 97, no. 16, pp. 164102, 2010.

[96] M. Bryant and E. Garcia "Development of an aeroelastic vibration power harvester," *Proceedings of SPIE,* vol. 7288, pp. 728812, 2009.

[97] M. Bryant and E. Garcia "Energy harvesting: A key to wireless sensor nodes," *Proceedings of SPIE,* vol. 7493, pp. 749311, 2009.

[98] M. Bryant, E. Garcia and A. Fang "Self-powered smart blade: Helicopter blade energy harvesting," *Proceedings of SPIE,* vol. 7643, pp. 764317, 2010.

[99] M. Bryant and E. Garcia "Modeling and testing of a novel aeroelastic flutter energy harvester," *Journal of Vibration and Acoustics*, vol. 133, no. 1, pp. 011010, 2011.

[100] M. Bryant, E. Wolff and E. Garcia "Parametric design study of an aeroelastic flutter energy harvester," *Proceedings of SPIE,* vol. 7977, pp. 79770S, 2011.

[101] J. Park, K. Kim, S. Kwon and K. H. Law "An aero-elastic flutter based electromagnetic energy harvester with wind speed augmenting funnel," *The International Conference on Advances in Wind and Structures,* 2012.

[102] Website, "MicroBelt tech sheet".

[103] D. Pimentel, P. Musilek and A. Knight "Energy harvesting simulation for automatic arctic monitoring stations," *IEEE Electrical Power & Energy Conference*, 2010.

[104] F. Fei, J. D. Mai, and W. J. Li, "A wind-flutter energy converter for powering wireless sensors," *Sensors and Actuators A,* vol. 173, no. 1, pp.163–171,2 012.

[105] K. H. Kim, D. Choi, and Y. H. Seo "Piezoelectric energy harverster using flow-induced vibration," *Proceedings of Power MEMS,* pp.197-200, 2008.

[106] C. Sun and J. Shi "PVDF microbelts for harvesting energy from respiration," *Energy and Environmental Science*, vol. 4, pp. 4508-4512, 2011.

[107] D. St. Clair, A. Bibo, V. R. Sennakesavababu, M. F. Daqaq and G. Li "A scalable concept for micropower generation using flow-induced self-excited oscillations," *Journal of Applied Physics*, vol. 96, no. 144103, 2010.

[108] B. H. Kim, D. Choi and Y.H.Seo "Piezoelectric energy harverster using flow-induced vibration," *Proceedings of Power MEMS,* pp.197-200. 2008.

[109] Y. H. Seo, B. Kim and D. Choi "Piezoelectric energy harverster using flow-induced vibration for infrastructure health monitoring applications" *Microsystem Technologies*, vol. 21, pp. 169–172, 2015.

[110] Y. Yang, G. Zhu, H. Zhang, J. Chen, X. Zhong, Z. Lin, Y. Su, P. Bai, X. Wen and Z. Wang "Triboelectric nanogenrator for harvesting wind energy and as self-powered wind vector sensor system," *ACS Nano*, vol. 7, no.10, pp. 9461-9468, 2013.

[111] S. Wang, X. Mu, Y. Yang, C. Sun, A.Y. Gu and Z. Wang "Flow-driven triboelectric generator for direct powering a wireless sensor node," *Advanced Materials.*,vol. 27, pp. 240-248, 2015.

[112] X. Wang, S. Wang, Y. Yang and Z.Wang "Hybridized electromagnetic–triboelectric nanogenerator for scavenging air-flow energy to sustainably power temperature sensors," *ACS Nano*, vol. 9, no.4, pp. 4553-4562, 2015.

[113] D. Zhu, S. Beeby, J. Tudor, N. White and N. Harris "A novel miniature wind generator for wireless sensing applications," *Proceedings of IEEE Sensor*, 2010.

[114] S. B. Horowitz, "Development of a MEMS-based acoustic energy harvester," *Proceedings of Power MEMS*, 2005.

[115] F. Liu, A. Phipps, S. Horowitz, K. Ngo, L. Cattafesta, T. Nishida and M. Sheplak, "Acoustic energy harvesting using an electromechanical Helmholtz resonator," *Journal of Acoustical Society of America*, vol. 123, no. 4, pp. 1983-1990, 2008.

[116] S. P. Matova, R. Elfrink, R. J. M. Vullers and R. van Schaijk "Harvesting energy from airflow with micromachined piezoelectric harvester inside a Helmholtz resonator," *Proceedings of Power MEMS*, 2010.

[117] C. B. Williams, and R. B. Yates "Analysis of a micro-electric generator for Microsystems," *Sensors and Actuators A: Physical*, vol. 52, no. 1–3, pp 8–11, 1996.

[118] S. Beeby, M. Tudor and N. White "Energy harvesting vibration sources for microsystems applications" *Measurement Science and Technology*, vol. 17, no. 12, pp. R175–R195, 2006.

[119] S. J. Roundy "Energy scavenging for wireless sensor nodes with a focus on vibration to electricity conversion," Ph.D. Dissertation, University of California, 2003.

[120] S. J. Roundy, P. K. Wright and J. M. Rabaey "Energy scavenging for wireless sensor nodes with a focus on vibrations" chapter 5, *Boston Kluwer Academic Press*, 2004.

[121] A Cammarano, S.G. Burrow, D.A.W. Barton, A. Carrella, and L. R. Clare "Tuning a resonant energy harvester using a generalized electrical load" *J Smart Mater Struct,* 19 055003, 2010

[122] N. Stephen "On energy harvesting from ambient vibration" *J. Sound Vib.* 293 409–25, 2006

[123] G. K. Batchelor "An introduction to fluid dynamics," chapter II, *Cambridge University Press*, 2000.

[124] H. Glauert “The elements of aerofoil and airscrew theory,” *Cambridge University Press*, 1947.

[125] H. Abbott and A. E. Doenhoff “Theory of wing sections including a summary of airfoil data,” *Courier Corporation*, 1959.

[126] Website, “http://www.electroscience.com/html”.

[127] Website, “http://www.memsnet.org/material/leadzirconatetitanatepzt”.

[128] H. S. Yoon, G. Washington and A. Danak “Modeling, optimization, and design of efficient initially curved piezoceramic unimorphs for energy harvesting applications,” *Journal of Intelligent Material Systems and Structures*, vol. 16, no. 10, pp. 877–888, 2005.

[129] P. Glynne-Jones, S. P. Beeby, P. Dargie, T. Papakostas and N. M. White “An investigation into the effect of modified firing profiles on the piezoelectric properties of thick-film PZT layers on silicon,” *Measurement Science and Technology*, vol. 11, no. 5, pp. 526–531, 2000.

[130] P. Dargie, R. Sion, J. Atkinson and N. White “An investigatin of the effect of poling conditions on the characteristics of screen-printed piezoceramics,” *Microelectronics International*, vol. 15, no. 2, pp. 6–10, 1998.